Spring 2022

Time-Resolved PIV Measurements of Ship Airwakes with Quartering Winds

Kaijus H. Palm
Embry-Riddle Aeronautical University – Daytona Beach, palmk@my.erau.edu

TIME-RESOLVED PIV MEASUREMENTS OF SHIP AIRWAKES WITH QUARTERING WINDS

By

Kaijus H. Palm

A Thesis Submitted to the Faculty of Embry-Riddle Aeronautical University

In Partial Fulfillment of the Requirements for the Degree of

Master of Science in Aerospace Engineering

April 2022

Embry-Riddle Aeronautical University

Daytona Beach, Florida

TIME-RESOLVED PIV MEASUREMENTS OF SHIP AIRWAKES

WITH QUARTERING WINDS

By

Kaijus H. Palm

This Thesis was prepared under the direction of the candidate's Thesis Committee Chair, Dr. J. Gordon Leishman, Department of Aerospace Engineering, and has been approved by the members of the Thesis Committee. It was submitted to the Office of the Senior Vice President for Academic Affairs and Provost, and was accepted in the partial fulfillment of the requirements for the Degree of Master of Science in Aerospace Engineering.

THESIS COMMITTEE

J. Gordon Leishman Digitally signed by J. Gordon Leishman Date: 2022.04.18 13:31:21 -04'00'

Chair, Dr. J. Gordon Leishman

Ebenezer P Gnanamanickam Digitally signed by Ebenezer P Gnanamanickam Date: 2022.04.18 15:53:29 -04'00'

Member, Dr. Ebenezer P. Gnanamanickam

John Ekaterinaris Digitally signed by John Ekaterinaris Date: 2022.04.18 18:22:37 -04'00'

Member, Dr. John A. Ekaterinaris

Daewon Kim Digitally signed by Daewon Kim Date: 2022.04.19 09:03:23 -04'00'

Graduate Program Coordinator,
Dr. Daewon Kim

4/19/2022

Date

Dean of the College of Engineering,
Dr. James W. Gregory

Date

Associate Provost of Academic Support,
Dr. Christopher Grant

Date

ACKNOWLEDGMENTS

I would like to express my greatest gratitude towards my advisor and my mentor, Professor J. Gordon Leishman, who provided me the opportunity to pursue a graduate degree under his guidance. Throughout the years, I have learned many valuable lessons from Dr. Leishman, and with every interaction, I keep learning something new. I am amazed and inspired by the discipline and passion he has, and I can only strive to follow his footsteps. With great excitement, I look forward to continuing my studies under his wings.

I want to thank Dr. Zheng Zhang for teaching me the procedures of conducting particle image velocimetry measurements, as well as helping me run the experiments themselves. I have learned a lot and his advice and guidance helped shape my work. I would also like to thank Professor Ebenezer Gnanamanickam, who was always willing to help and provide suggestions for improvements, and I hope to learn more from him. I am also very thankful to Professor John A. Ekaterinaris for his advice on ways to interpret my results.

A special thank you to my friend and labmate, Nicholas Zhu, who was willing to help me set up and run every experiment. I appreciate the conversations we have, they always bring great pleasure and a different perspective. I would also like to thank Dr. Dhuree Seth, whose doctoral work laid the foundation for the ship airwake study and was valuable to this thesis. From the wind tunnel facility, I want to thank Mr. Joel Mills, who was always willing to help install the Cowdrey Rods, and would lend a hand when needed. I also want to express my appreciation to the undergraduate students who have helped at the wind tunnel, especially Matthew O'Brien, Emma Nicotra, and David A. Paolicelli.

The group of friends that I've made throughout my time here has been a great source of joy. I want to thank Gregory Enriquez, Aldous George, Arjun Vedam, Miriam Theobald-Deschine, Patricio Garzon, Samuel Afari, Guillermo Mazzilli, Michael Wannemacher, and Riccardo Roiati, who have birghtened my days and have left memorable moments outside of academics.

Of course, I would not be here without the love and support from my family, especially my parents. I am forever grateful for everything they have done for me. They give me the

strength to get through tough times and are always there when I need them. I want to make them happy and proud, as they deserve the best.

Lastly, I would like to thank the U.S. Army/Navy/NASA Vertical Lift Research Center of Excellence at Penn State University and Georgia Tech for the support received under Agreement No. W911W6-17-2-0003 and Agreement No. W911W6-21-2-0001, under the direction of Mahendra Bhagwat of the US Army Futures Comment. Opinions, interpretations, conclusions, and recommendations are those of the author and are not necessarily endorsed by the United States Government. I want to also thank ONR DURIP for support in acquiring instrumentation through award N00014-17-1-2853. My graduate studies would not be possible without the funding I have received. I am truly grateful for the opportunity, and I hope the outcomes of my work will provide value for future research related to the ship airwake problem.

ABSTRACT

The unsteady, three-dimensional, turbulent airwake over the Simple Frigate Ship No. 2 (SFS2) with quartering wind flow directions was studied in a low-speed wind tunnel facility. Surface oil flow visualization and time-resolved stereoscopic and planar particle image velocimetry (PIV) measurements were made for three crosswise planes and a single centerline streamwise plane. Measurements included various configurations with the bow of the ship model at two different quartering wind conditions of 10 and 20 degrees, as well as cases with and without the effects of a simulated atmospheric boundary layer (ABL). A comparative analysis of the time-averaged flow structures between the quartering wind cases and the pure headwind measurements showed significant differences in the development of the airwake. For both quartering wind cases, the funnel wake had a trailing vortex on the windward side and large cross-sectional velocity magnitudes. The flight deck recirculation region decreased in size and became asymmetric for both quartering wind cases. Different flight deck vortical structures were found, indicating a difference within the flow field based on the yaw angle. A spectral analysis showed the streamwise fluctuations contained more energy for the quartering wind cases in the funnel wake region, which was also seen in the turbulent fluctuations. Two-point velocity correlations revealed large-scale coherent motion in the streamwise direction. The coherent behavior was further related to the observed time-averaged flow field structures through proper orthogonal decomposition (POD). The POD analysis highlighted the nontrivial behavior that was inherent to the airwake. These findings further emphasize the complexity of the airwake and necessity of understanding the development of the airwake under a broad range of conditions.

TABLE OF CONTENTS

LIST OF FIGURES

Figure **Page**

LIST OF TABLES

Table **Page**

NOMENCLATURE

$\boldsymbol{C}$	Covariance matrix
$\boldsymbol{C_s}$	Correlation matrix
f	Frequency, Hz
f_s	Sampling frequency, Hz
I	Turbulence intensity
k	Turbulent kinetic energy, $\mathrm{m}^2\ \mathrm{s}^{-1}$
l	Length of the flight deck, m
M	Mach number
N_t	Number of time instances
r	Mode number in POD
$\boldsymbol{R}$	Time dynamics matrix for POD
R_{ij}	Correlation coefficient between two quantities i and j
Re	Reynolds number $= \rho U_\infty SL/\mu$
SH	Ship height
SL	Ship length
St	Strouhal number
$\boldsymbol{U}$	Data set matrix of size n-by-m
U_∞	Free-stream velocity, $\mathrm{m\ s}^{-1}$
U_{ref}	Reference velocity, $\mathrm{m\ s}^{-1}$

u, v, w	Streamwise, spanwise, and wall-normal velocities, m s^{-1}
$u_{\text{rms}}, v_{\text{rms}}, w_{\text{rms}}$	Root mean square values of velocity components, m s^{-1}
$\overline{u}, \overline{v}, \overline{w}$	Time-averaged velocity components, m s^{-1}
$\overline{u}_{\text{unc}}, \overline{v}_{\text{unc}}, \overline{w}_{\text{unc}}$	Time-averaged velocity uncertainty components, m s^{-1}
u', v', w'	Instantaneous velocity fluctuations, m s^{-1}
$\overline{u'}, \overline{v'}, \overline{w'}$	Time-averaged velocity fluctuations, m s^{-1}
$\boldsymbol{x}$	Spatial position within a flow field, m
Δt	Straddling time between frames, μs
$\boldsymbol{\Delta x}$	Spatial displacement within a flow field, m
μ	Dynamic viscosity of air, kg m^{-1} s^{-1}
ρ	Density of air, kg m^{-3}
$\boldsymbol{\Sigma}$	Singular value matrix for POD
σ	Singular value from POD calculation
$\boldsymbol{\Phi}$	Spatial basis matrix for POD
ψ	Yaw angle, deg.
ABL	Atmospheric Boundary Layer
CFD	Computational Fluid Dynamics
DI	Dynamic Interface
ERAU	Embry-Riddle Aeronautical University
FFT	Fast Fourier Transform

FOV	Field of View
HWA	Hot-Wire Anemometry
LDA	Laser Doppler Anemometry
LES	Large Eddy Simulation
LSWT	Low-Speed Wind Tunnel
PCA	Principal Component Analysis
PIV	Particle Image Velocimetry
POD	Proper Orthogonal Decomposition
PSD	Power Spectral Density
PTU	Programmable Timing Unit
ROI	Region of Interest
SFS	Simple Frigate Shape
SFS2	Simplified Frigate Shape No. 2
SHOL	Ship-Helicopter Operating Limits
SPOD	Spectral Proper Orthogonal Decomposition
SVD	Singular Value Decomposition
TiO_2	Titanium Dioxide
TKE	Turbulent Kinetic Energy
TR-PIV	Time-Resolved Particle Image Velocimetry
WOD	Wind Over Deck

1 Introduction

The present work contributes to the further understanding of ship airwakes. The airwake affects helicopter operations from the deck of a ship, which contributes to the so-called ship-helicopter dynamic interface (DI) problem. The airwake poses difficulties for aircraft flight operations, particularly during the takeoff and landing phases. In the presence of rough seas, this process can be additionally hazardous because of the movement of the flight deck relative to the aircraft. The main objective of the research work reported in this thesis is to study the unsteady, turbulent airwake of the ship with different quartering wind conditions, i.e., with the wind coming at an angle or "quartering" with respect to the bow of the ship. A general overview of the airwake problem and the challenges in its measurement will be covered in this chapter, and the relevant literature published on ship airwakes with quartering winds will be reviewed. This chapter will conclude with a more detailed description of the technical objectives and an outline of the thesis as a whole.

1.1 Ship Airwake as a Contributor to the Dynamic Interface Problem

The airwake produced by most naval ships potentially creates a challenging environment for an operating helicopter. The airwake is just one contributor to the so-called dynamic interface (DI), which more broadly refers to the environment between the ship and an operating aircraft. Fundamentally, one root of the DI problem lies in the coupled aerodynamics between the airwake and the flow field produced by the helicopter. Naval ships are mostly bluff bodies, which produce complex three-dimensional, unsteady, separated flows. The geometric features of a ship also generate a variety of coherent vortex flows with local regions of shed vorticity [13]. A helicopter landing on the flight deck can encounter this complex unsteady vortical flow. Such conditions can pose many challenges for an operating helicopter as it encounters the upwash and downwash flow in the airwake, which adds significantly to the pilot's workload. The ship's motion dynamics add an additional layer of complexity for the pilot. A ship has motion in six degrees of freedom: roll, pitch, yaw, heave, surge, and sway. Compensating for the swaying and heaving of the ship requires additional control inputs, increasing further the

Figure 1.1 A helicopter landing on the flight deck of a frigate. Accessed November 2021, source: https://www.navyrecognition.com/index.php/naval-news/naval-exhibitions/2016-archives/dsa-2016/.

pilot's workload over and above that caused by the airwake. This motion can be significant (Fig. 1.1), complicating the station-keeping of the helicopter near the deck of the ship.

Despite the difficulties of operating in such an environment, ship-helicopter operating limits (SHOL) can be established, which map out the safe conditions for launch and recovery operations [14]. The boundaries of the SHOL are established through at-sea flight trials with specific makes and models of helicopter. These trials lead to conservative estimates of operating envelopes that are only further limited by weather constraints rather than by aircraft or pilot capabilities [1].

A typical SHOL diagram is illustrated in Fig. 1.2, where the bold lines around the ship depict the safe operating conditions for a particular helicopter. The SHOL diagram shows the allowed relative speeds for a certain wind over deck (WOD) angle. However, these speeds are not the same for every angle, which suggests that the changes in the airwake caused by different quartering wind conditions affect the safe operating limits, i.e., when the wind approaches at an angle to the bow of the ship.

It is clear that aerodynamics play a major role in determining the operational envelope. In fact, quartering winds affect the operational limits for all wind directions either directly or indirectly [8]. An alternative option is desired because the SHOL boundaries are primarily established through at-sea trials, which are time-consuming and carry significant risk. One such method would be a flow model that simulates the airwake. A better model of the airwake as a contributing factor to the DI would significantly improve pilot training using flight simulators, which are a safer and cheaper alternative than pilot training at sea.

From an aerodynamic perspective, computational simulations of the airwake could also help to understand the intricate flow physics involved [1], which are difficult to measure, particularly on an actual ship. Furthermore, an airwake model may also give some beneficial detailed augmentation to the SHOL definition process (Advani and Wilkinson [15]), or even to the ship geometry itself such as to widen the useful operating envelope [7, 16]. With that being said, no valid DI simulation can exist without an accurate representation of the quartering wind airwake (Zan [8]). To this end, there is a need for very detailed, time-resolved measurements of the ship airwake under very controlled testing conditions, which can be achieved in a wind tunnel.

The ship airwake problem is not new and has been studied for many decades in wind tunnels. Some of the earliest measurements of ship airwakes date back to the 1950s. Methods used to study the airwake were by using hot-wire anemometry (HWA), multi-probe pressure measurements, and flow visualization [17]. These measurement techniques are staples of wind tunnel testing and are in everyday use today. Hot-wire anemometry, in particular,

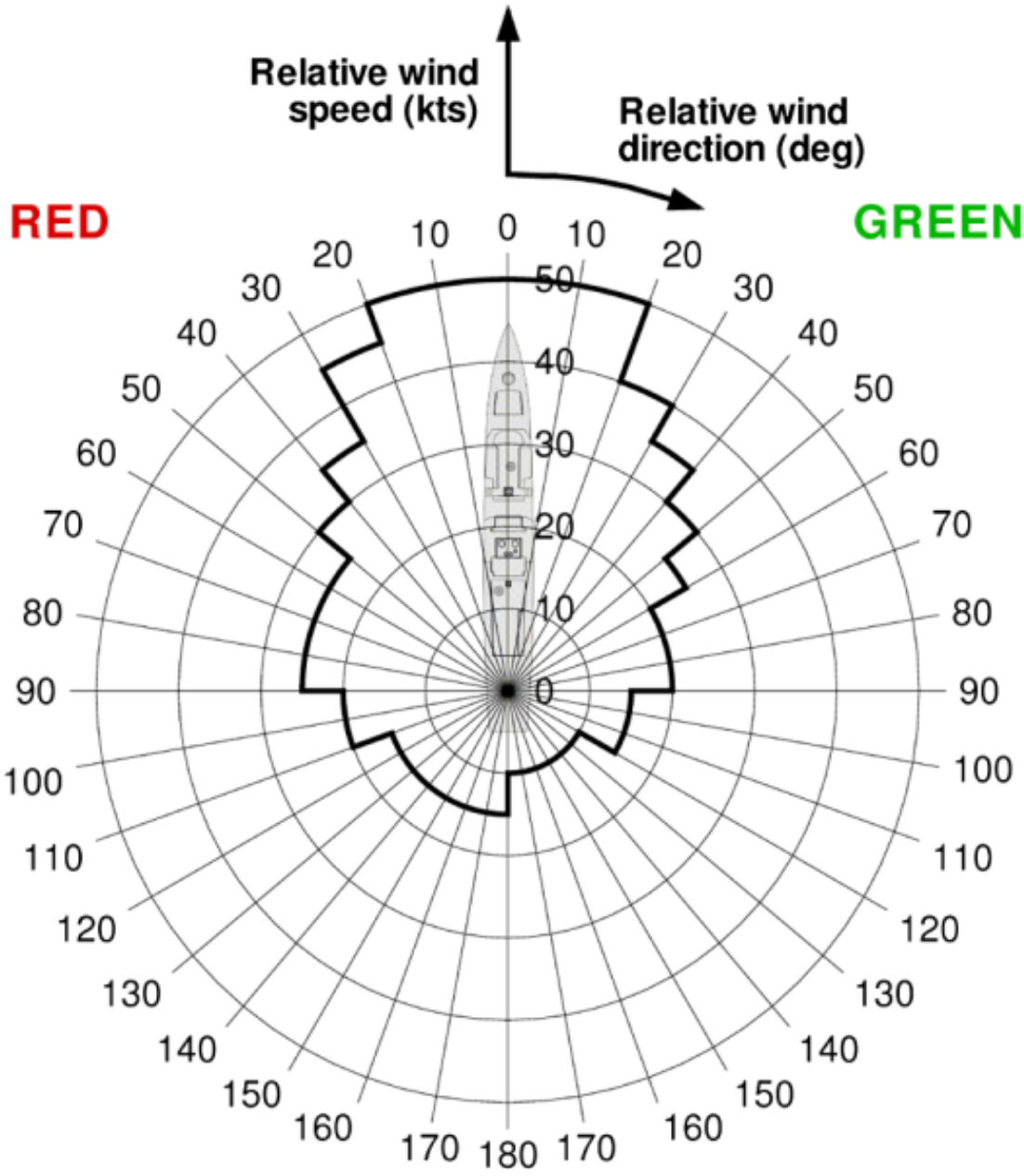

Figure 1.2 A typical ship-helicopter operating limits (SHOL) diagram [1].

has been used for point-wise measurements of the various stochastic quantities associated with turbulent flows [18]. While HWA has provided some insight, it is a point measurement method and cannot cover an entire spatial domain easily. Of course, this latter issue can be addressed by using multiple hot-wire probes; however, the approach soon becomes impractical because of the number of probes needed to obtain temporal correlations.

More advanced optical flow measurement techniques have been applied in more recent decades to study the airwake problem. Non-intrusive methods such as laser Doppler anemometry (LDA) and particle image velocimetry (PIV) are widely used to measure complex flow fields. PIV enables spatially resolved measurements of the instantaneous velocity field and allows the detection of large and small scale spatial structures in the flow [19]. The extent to which these techniques have been applied to the airwake problem will be covered in more detail in the literature review. The objective is clear; through detailed flow measurements, then an understanding of the flow features of the airwake can be obtained.

Predicting the airwake has also been attempted using computational fluid dynamics (CFD). However, highly unsteady turbulent, separated flows pose many challenges for CFD. But the advantages of such models are clear if they can be adequately validated, which is a fully spatial and temporal representation of the airwake. However, neither wind tunnel measurements nor contemporary CFD can replace at-sea trials [17]. Establishing an adequate model for the decoupled ship airwake with different quartering wind conditions is clearly a significant challenge. Some recent CFD studies are addressing the coupled airwake as well [20].

Measurements in the wind tunnel can be used for computational model validations. For proper validations, the geometric models and flow conditions of the ship airwake must be in agreement between CFD and experimental setups. The Simplified Frigate Shape No. 2 (SFS2) model has been and continues to be widely used to study the aerodynamics of a ship [3, 4, 7–10, 21, 22]. The SFS2 has been studied extensively in the wind tunnel, and the flow characteristics have been documented in detail for the headwind case. The flight deck of the SFS2 resembles that of a double backward-facing step [5], as shown in Fig. 1.3. This relatively simple canonical geometry has been used to understand the fundamental physics involved in the development of a ship's airwake. The SFS2 is also used as a basis for comparative studies and validations between experimental and computational results [17].

The present work uses the SFS2 ship model to study the airwake with different quartering

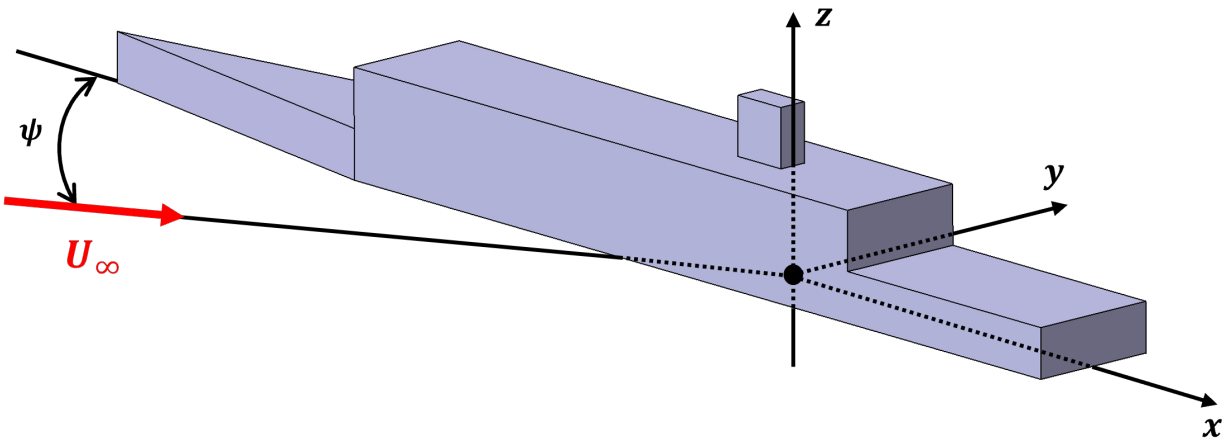

Figure 1.3 A schematic of the Simple Frigate Shape No.2 (SFS2) model configuration.

wind conditions. Although the flow physics of SFS2 have been widely studied, studies of different quartering wind conditions are relatively sparse, i.e., with the bow of the ship at different yaw angles. Experimental measurements for different quartering wind cases tend to focus on higher angles, such as $\psi = 30°$, $\psi = 45°$, or $\psi = 60°$. While these larger angles are important, there is a lack of understanding of how the flow structures change with each increased angle.

Computationally, there have been large-eddy simulations (LES) for smaller angles [4], which are capable of exposing the full three-dimensional airwake. A similar experimental approach would examine sections over the flight deck and measure the airwake using PIV. It is important to select key spatial locations, such that a comparison with the $\psi = 0°$ case can be made. Through these comparisons, a better grasp of the changes that the flow structures in the airwake undergo can be attained. Establishing this base understanding will help further investigate the turbulent behavior of the airwake and the changes in large- and small-scale structures. Ultimately, the outcomes from current research work show that there are significant differences in these flow structures across the flight deck as the yaw angle is increased.

1.2 Literature Review

A more detailed examination of the literature pertaining to the studies of different quartering wind conditions will be presented in this section. It is important to consider other types of measurements performed in prior research and the approaches taken to investigate the airwake behavior. The general experimental research will be covered first, after which the computational studies will also be addressed. Finally, the most relevant PIV measurements of the ship airwakes will be discussed. This section does not cover the full extent of the airwake problem described in the research literature. Instead, this review aims to highlight the most notable research performed on ship airwakes with the ship at different yawed configurations relative to the oncoming wind. In this regard, the results from these past studies include findings that apply to the work conducted in the present thesis.

1.2.1 Experimental Work on Airwakes

As mentioned previously, the ship airwake problem has been studied for many decades. Various measurement techniques have been used to study the flow. Because the airwake is highly unsteady and turbulent, HWA has been used to measure these effects. In the late 1970s, Garnett [23] performed HWA measurements and flow visualization on a navy destroyer model and found large areas of flow separation and turbulence behind the ship. For low yaw angles ($\psi < 30°$), Garnett found that the hull behaves almost exactly like a heavily loaded low aspect ratio wing, which sheds powerful vortices. In addition to smoke visualization, Garnett also used helium-soap bubble tracks to visualize the flow around the various elements of the superstructure. This visualization revealed a strong bound vortex in the lee of the hangar over the flight deck. This bound vortex was noted to recede quickly into a disorganized pattern when the ship yaw angles exceeded 10° and 15° in either direction. The helium-soap bubble observation also revealed that the mast structure acted as a large flow screen, which broke the flow structures into smaller ones and contributed to the incoherent flow behind the ship when it was yawed. Garnett added that the overall flow field behind the ship had a repeatable steady component at most yaw angles and locations throughout the airwake.

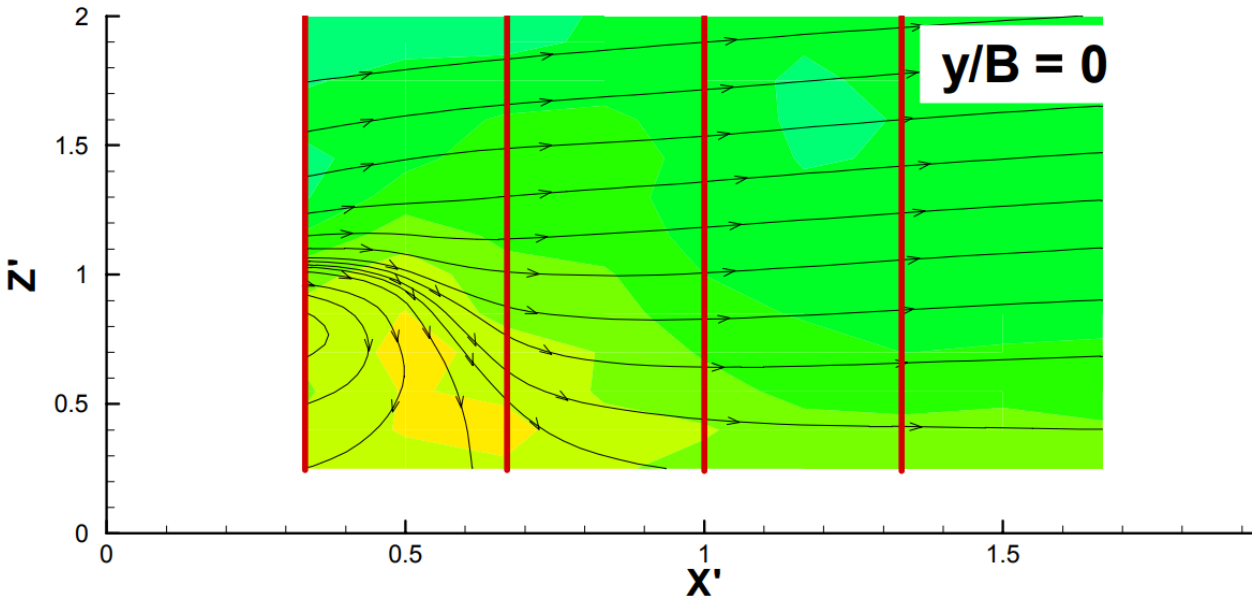

(a) Mean streamwise velocity contour over the flight deck.

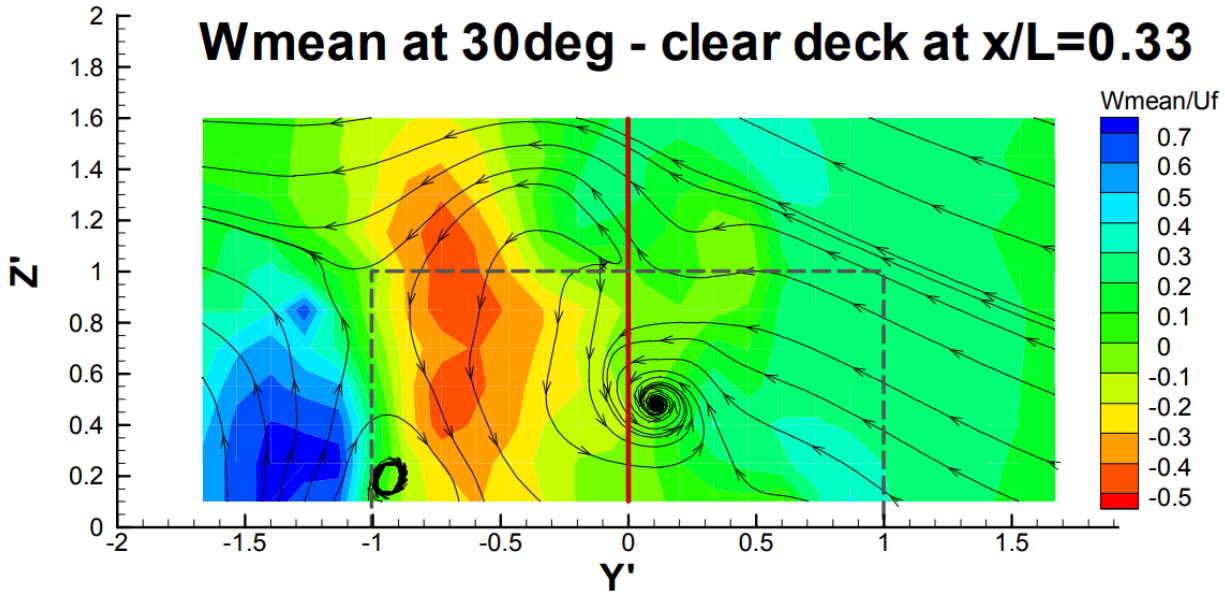

(b) Mean wall-normal velocity contour within a crosswise plane over the flight deck.

Figure 1.4 Laser Doppler anemometry (LDA) results showing the mean velocity contours over a generic frigate flight deck for $\psi = 30°$ [2]

A different HWA study was done by Healey [24], who performed three-dimensional measurements on a 1/141 scale ship. Unlike Garnett, Healey's focus was closer to the flight deck of the ship. It was noted that for the $\psi = 0°$ case, the flow over the hangar and flight deck region along the centerline of the ship showed characteristics similar to that of

a backward-facing step. This outcome included the familiar highly turbulent recirculation region. Healey noted, however, that near the edges of the ship the flow was far more complex and interacted with the recirculation region. An interesting result from Healey's study involved the spectral function of the turbulent velocity fluctuations. This spectra suggested that for the $\psi = 30°$ case at the touch-down point on the flight deck, the flow was much more disturbed than in the $\psi = 0°$ case. The key finding from the u-spectra showed that there was less low-frequency energy over the flight deck than further aft in the wake. Similar findings were observed for the v- and w-spectra. Lastly, Healey described the peculiar flow behavior of a yawed ship as a "rising and dropping" flow.

Laser Doppler anemometry was used by Greenwell and Barrett [2] to investigate novel flow control devices applied to a generic frigate flight deck. In their study, various crosswise and streamwise planes were investigated. Alongside the different shapes of the flight deck edge screens, these authors performed measurements for the $\psi = 30°$ case. It was highlighted that in the yawed case the flow was much more complex and unsteady, and a number of vortical structures were apparent in the crosswise planes. The crossflow topology changed rapidly as the the field of view (FOV) moved downstream.

This latter complex behavior is shown in Fig. 1.4, where the mean wall-normal velocity, of the plane intersecting the recirculation region, was captured. Figure 1.4 shows regions of large velocity gradients that were evident on the leeward side. The authors tried to identify the sources of these flow features with oil and smoke visualization, but because of the very low local velocities and high unsteadiness, the results were inconclusive. Nevertheless, five separate vortex structures were distinguished: 1. A large anti-clockwise vortex downwind of the flight deck, driven by the upwash from the hull side; 2. A small vortex sitting above the hangar roof on the centerline, which dissipates rapidly; 3. A small anti-clockwise vortex shed from the upwind edge of the flight deck; 4. & 5. A counter-rotating pair of vortices shed from the flight deck surface. Lastly, the authors mentioned that the high levels of turbulence encountered were likely related to large-scale unsteadiness within the flow, such as filling and

bursting of the recirculation region in the hangar lee, rather than the vortex structures that were observed.

Common observations can be noted between these three studies, even though the measurement methods were different. It is clear that prior findings indicated the airwake of the ship, yawed with respect to the wind, was different from the headwind case. The early measurements done by Garnett [23] were largely qualitative for the quartering wind cases. Although the model studied by Garnett was different, it still contained the common flow descriptions observed throughout literature for yawed ships—highly unsteady and complex. Conversely, Healey [24] quantitatively examined the turbulence content of the ship and highlighted that there was less low-frequency energy on the flight deck. From Healey's measurements, he was also able to describe the behavior shown in Fig. 1.4, where the wall-normal velocity had large regional gradients.

The study done by Greenwell and Barrett [2] provided great value to the work in this thesis. Despite the $\psi = 30°$ case, very similar flow features were observed in the present work,

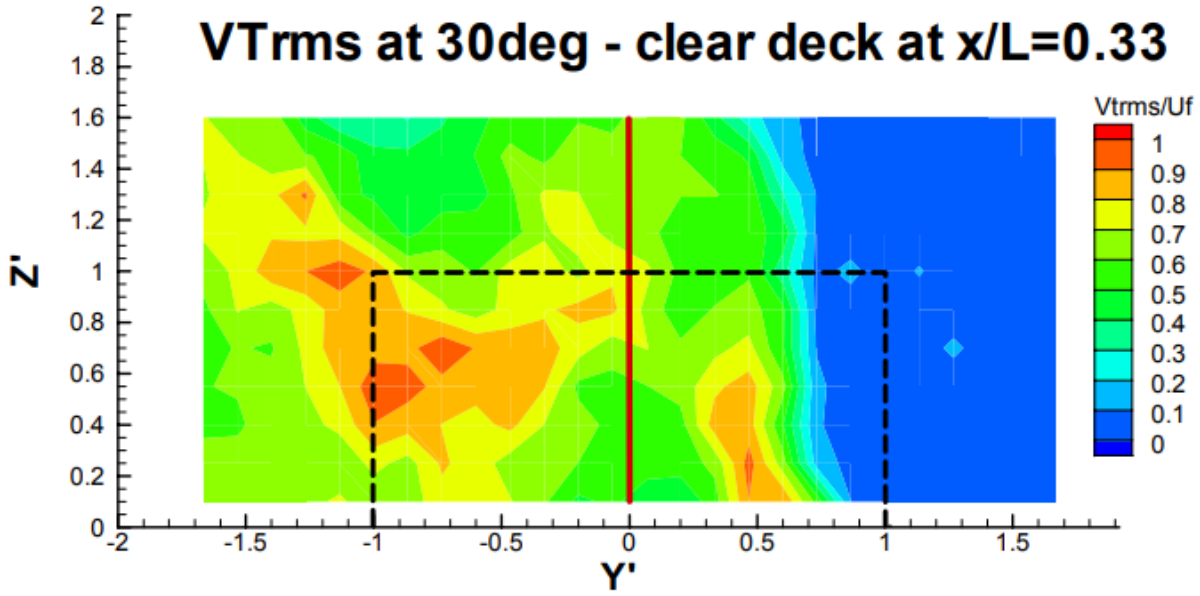

Figure 1.5 Turbulence intensity from laser Doppler anemometry (LDA) results for $\psi = 30°$ [2].

which will be further discussed and related in the Results & Discussion section, specifically the findings in Fig. 1.4 & 1.5. With that being said, the research covered thus far should provide a basis of what to expect from the flow behavior of ship airwakes with quartering wind conditions.

1.2.2 Computational Work on Airwakes

Computationally modeling the ship's airwake is no trivial task. Analogous to the different measurement techniques, various computational solvers have been used, each with advantages and disadvantages. Polsky [13] used Cobalt, a Reynolds-Averaged Navier-Stokes solver, to predict the unsteady flow field produced by the superstructure of an assault class ship. Two different turbulence models were explored, and Polsky found that the steady-state CFD calculations were unable to predict even the time-averaged flow field. One of the models Polsky used was a monotone integrated large eddy simulation, which is a form of turbulence modeling for LES. This method had more success and showed that major flow features changed drastically in the $\psi = 30°$ case. Polsky noted that the flow separation off the bow was nonexistent for $\psi = 30°$, and because the flow separation was a source for the periodic shedding of "burbles," this feature was not present in the yawed case. Additionally, significant flow separation was observed on the starboard deck edge, and considerably more of the leeward island flow was separated.

CFD simulations for the SFS2 ship model have also been studied. Yuan et al. [21] used OpenFOAM to study the flow over the SFS2 model and compared it to hot-wire measurements. Yuan's group employed delayed detached eddy simulations in OpenFOAM and captured the unsteady airwake relatively well. The authors mentioned that for the $\psi = 45°$ case, the flow over the flight deck was dominated by separated flows from the windward vertical edge of the hangar and the windward flight deck edge. The formation of a vortical structure at the corner of the windward edge of the hangar roof was also observed. These latter results also showed that the off-body flow region was larger and more complex than the unyawed case. However, it was acknowledged in the absence of validation with measurements that the CFD

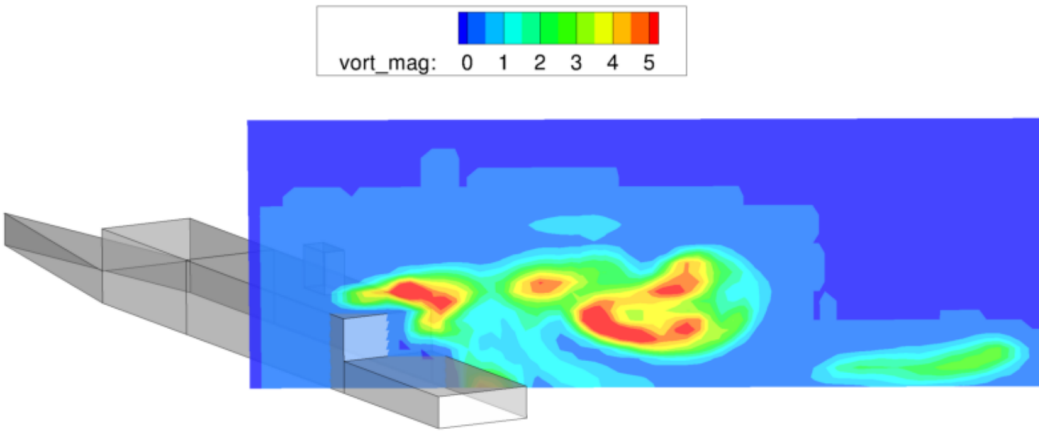

Figure 1.6 Instantaneous vorticty magnitude contour on a plane intersecting the hangar and aligned with the free-stream flow [3].

calculations only qualitatively captured the flow features of the airwake.

Quon et al. [3] used an unsteady Reynolds-Averaged Navier-Stokes solver to study the SFS2 model and compared the results to five-hole probe measurements of the airwake made in a wind tunnel. Quon's group investigated a rather large angle of $\psi = 60°$, and observed complex interactions in the hangar wake region, as shown in Fig. 1.6. The majority of the deviations from the experiment occurred at locations below hangar height, which was similar to their headwind case. It was also noted that the greatest amount of variability, caused by bluff-body flow physics, was observed in the wake of the hangar, which was measured by the probes as well. However, the authors mentioned that the CFD over-predicted these latter effects. Lastly, these authors emphasized that further effort was to be focused on understanding the complex vortical flow behavior in the hangar wake for both headwinds and yawed cases. Results showed the most significant discrepancies appeared near the surface of the flight deck.

The effect of yaw angle on the bi-stable airwake of the SFS2 model was investigated using LES by Zhang et al. [4]. This group studied smaller yaw angles of $\psi = 2.5°$, $\psi = 5°$, and $\psi = 10°$. Extensive analysis was done on understanding the reason behind the changes in the bi-stability of the recirculation region behind the hangar doors and on the deck. For smaller

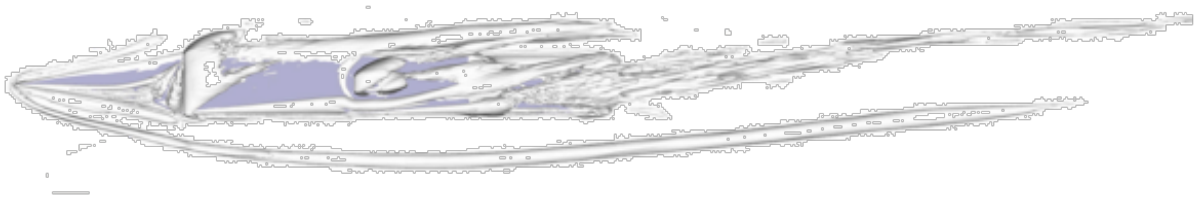

Figure 1.7 Time-averaged iso-surfaces of Q-criterion for $\psi = 10°$ [4].

angles, it was observed that the bi-stable recirculation region remained asymmetric behind the hangar doors and at the ship's stern.

Interestingly, this latter behavior was no longer present at higher yaw angles of $\psi = 5°$ and $\psi = 10°$. Instead, the recirculation region at the stern became more symmetric. A vorticity analysis revealed that smooth incoming flow became more turbulent as a result of the sharp bow of the generic ship. Massive flow separations that originated from the edges developed towards the end of the ship, and resulted in a highly turbulent wake. The authors also noted that with the increase of yaw angle, the vortex region at the bow of the ship became larger, while simultaneously the region on top of the superstructure became smaller. This latter effect can be seen in Fig. 1.7, where the top of the superstructure had a region with no iso-surfaces of Q-criterion. The Q-criterion represents areas with vorticity magnitude being greater than the magnitude of the rate of strain, and it is used as a vortex identification method.

Overall, the computational simulations of the airwake performed thus far and reported in the literature showed broadly similar results as shown by the numerous measurements. The most extensive study of the yaw effects was done by Zhang et al. [4], whereas the other studies did not elaborate on the changes to the flow structures. It appears that LES provided reasonable agreement with experimental results, and it seems appropriate for predicting the airwake. As discovered by Polsky [13], however, steady-state models failed to capture the time-averaged flow. There is clearly a significant advantage in computational simulations because, for example, the whole spatial domain can be resolved, as shown in Fig. 1.7. However, validation with measurements remains essential if confidence in prediction is to be obtained.

The iso-surfaces in Fig. 1.7 revealed flow structures that were also observed in the oil flow and PIV measurements of this thesis work.

1.2.3 Particle Image Velocimetry

In recent years, PIV has been applied to study the ship airwake problem. Some of the benefits offered by PIV were mentioned in section 1.1. Considering that the ship airwake is highly unsteady, PIV is a suitable tool to study such a flow field. The airwake of the SFS2 model has flow structures akin to those seen on a double backward-facing step. Thus, it is important to recognize these fundamental flow behaviors. Tinney and Ukeiley [5] used PIV and oil flow visualization to study the flow over a three-dimensional backward-facing step. The study categorized some of the major flow structures seen on such geometries (Fig. 1.8). A unique identification from this study involved the counter-rotating vortex pair that formed after the saddle point, which was caused by transverse entrainment of fluid and its collision at the center of the model. The authors also identified a peak in the power spectral density around $St = 0.17$. However, there was no evidence that suggested the peak was caused solely by a lateral oscillation in the flow.

Sydney et al. [22] investigated how the airwake of the SFS2 model was affected by ship orientation and oscillation frequency. The study used PIV in a subsonic closed-return wind

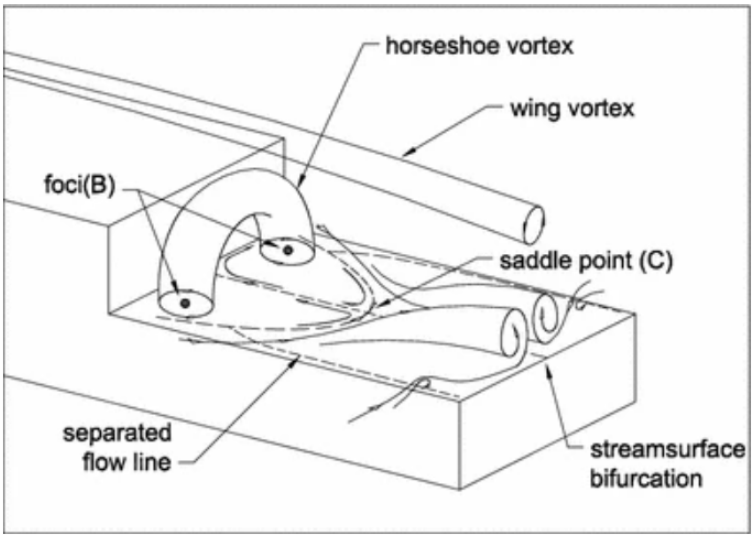

Figure 1.8 Flow structures seen on a three-dimensional double backward-facing step [5].

tunnel. The changes in orientation were only related to pitch, which was accomplished using a motion platform, and a sealing mechanism within the test section. One of the major effects caused by the pitch orientation was the translation of the airwake higher above the flight deck. The key outcome of this effect suggested that the shear layer was primarily dominated by the free-stream velocity. The changes in turbulence were also examined by Sydney et al. [22]. Three main sources were identified, which included the hangar, the funnel, and the front of the funnel, referred to as the forward step. The turbulence from the forward step interacted with the funnel wake further down at the flight deck midpoint, but at the height of the funnel. As the pitch angle was increased, the interaction occurred lower, and at a pitch angle of 2.5° it was at the height of the hangar. It was also highlighted that the turbulence intensity increased at higher pitch angles, and the authors noted that the result was expected, since previous studies have shown that the forward step can produce the strongest vorticity in the SFS2 airwake.

Seth et al. [10] performed an extensive analysis of the SFS2 airwake and included the effects of a simulated atmospheric boundary layer (ABL) into the experimental configuration. The turbulent ABL was simulated using two sets of Cowdrey rods, which were placed at adequate distances to allow mixing before the flow reached the test section inlet. The airwake was measured with and without the simulated ABL, but the results showed that the effects of the simulated ABL were important in determining the details of the flow over the flight deck. It was observed that the flow with and without the ABL qualitatively looked very similar, which suggested that the geometry of the ship produced most of the turbulence and the effects of the upstream turbulent ABL were secondary. The study also used spectral proper orthogonal decomposition (SPOD), which takes the frequency domain of the flow and performs a proper orthogonal decomposition (POD), to investigate the coherent flow scale evolution in space and time. The results showed that most of the larger energetic flow structures were at low frequencies and in the near-wall regions of the flight deck. It was also found that the shedding of vortices from the funnel wake and upstream superstructure had a

significant overall contribution to the turbulence in the airwake.

PIV measurements containing yawed cases are sparse. Nevertheless, Mora [6] used snapshot PIV on a simple frigate shape (SFS) model to study the flow across the flight

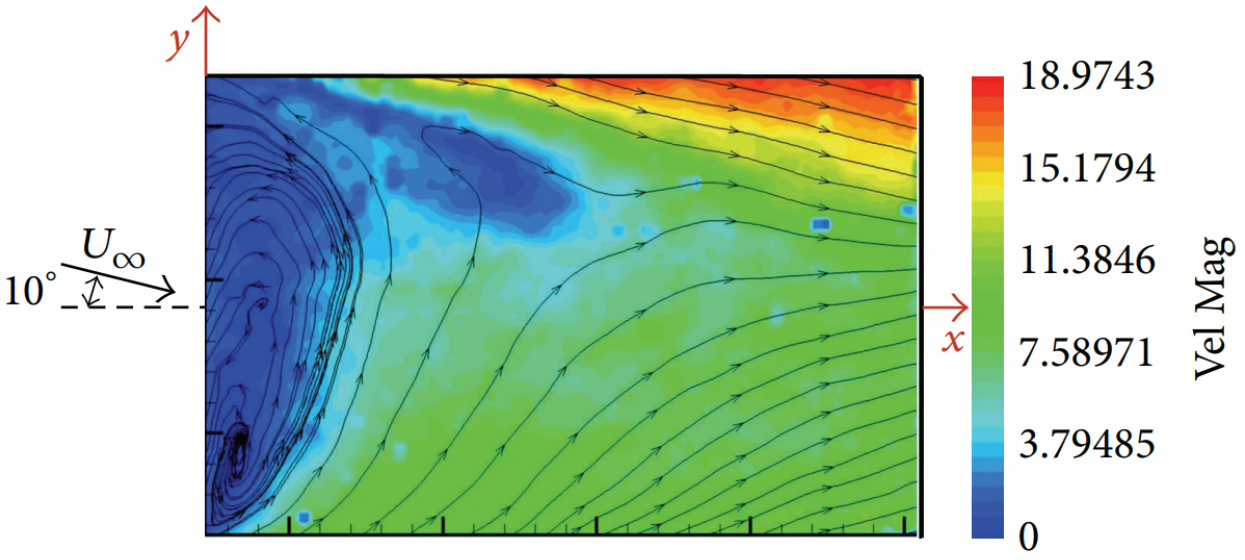

(a) $\psi = 10°$ case.

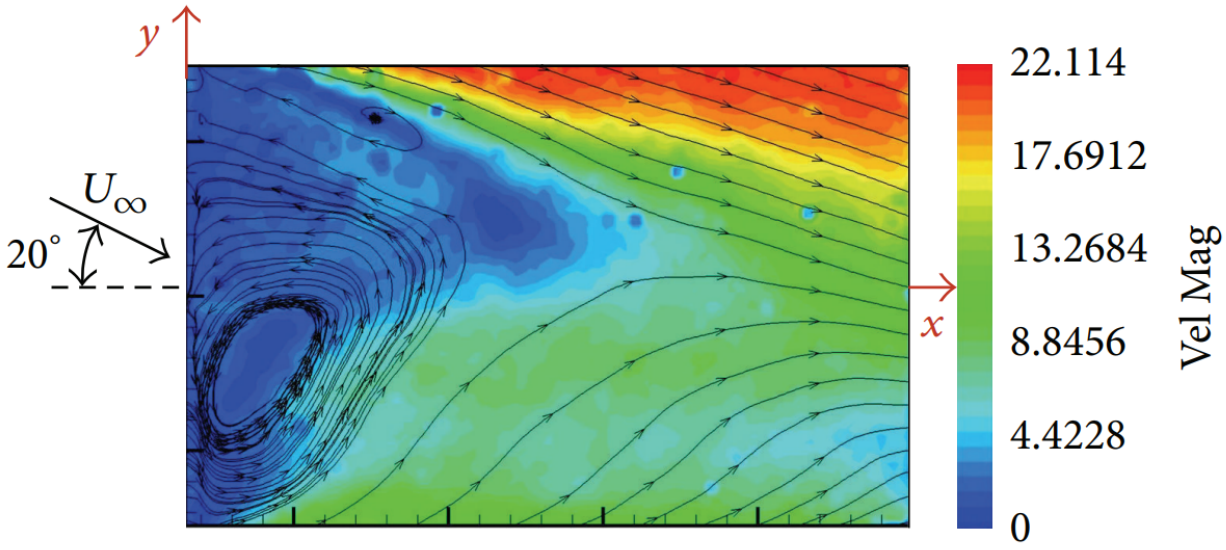

(b) $\psi = 20°$ case.

Figure 1.9 Snapshot particle image velocimetry (PIV) measurements of a horizontal plane located at the middle of the hangar on the Simple Frigate Shape (SFS) model flight deck. Figures show a top-down field of view (FOV) intersecting the recirculation region for $\psi = 10°$ and $\psi = 20°$ cases Mora [6].

deck. The results showed that for $\psi = 10°$ and $\psi = 20°$, the recirculation region became asymmetric, as seen in Fig. 1.9. The asymmetry appeared to be stronger for the $\psi = 20°$ case and more widespread on the starboard side. The author mentioned that the horseshoe structure from Fig. 1.8 was observed from these results, however, there was a lack of support whether the overall shape remained the same. It was evident that the measurement plane intersected some structures for the $\psi = 20°$ case in Fig. 1.9, but the horseshoe shape was not immediately apparent. The main finding from the study involved the comparison of the SFS model to a frigate model and full-scale ship data. It was shown that SFS was in agreement with frigate and full-scale ship results for a wide range of quartering wind conditions; however, there was a small range of higher yaw angles where the SFS model did not agree.

More recently, Mora et al. [7] studied the different hangar shape configurations for the SFS2 model using snapshot PIV. The study included measurements of $\psi = 15°$ and $\psi = 30°$, with a setup shown in Fig. 1.10. The choice of using the free-stream axis instead of the model's body axis is important. As seen in Fig. 1.6, the wake extended to the leeward side of the ship, and the choice of aligning the region of interest (ROI) with the free-stream axis captured the leeward wake. The downside of this choice manifests in the difficulty of characterizing the flow structures over the flight deck, where the ROI can miss important features. The objective of the study done by Mora et al. [7] was to examine the performance of different hangar shapes, rather than characterize the flow behavior. In this aspect, the study found that hangars with modifications had significantly better aerodynamic performance, especially the angled and elliptical shapes. This finding had relevance for the design of navy ships, as it was another way of addressing the DI problem.

When it comes to PIV, there is a clear lack of measurements made on the yawed airwakes. Despite Mora [6, 7] including such cases, the measurements were done using snapshot PIV, which is not resolved in time. The studies that have used time-resolved PIV (TR-PIV) [5, 9, 10, 22] did not include yawed cases. Thus, there is a need for an extensive study for different quartering wind conditions using TR-PIV; Greenwell and Barrett [2] suggested that

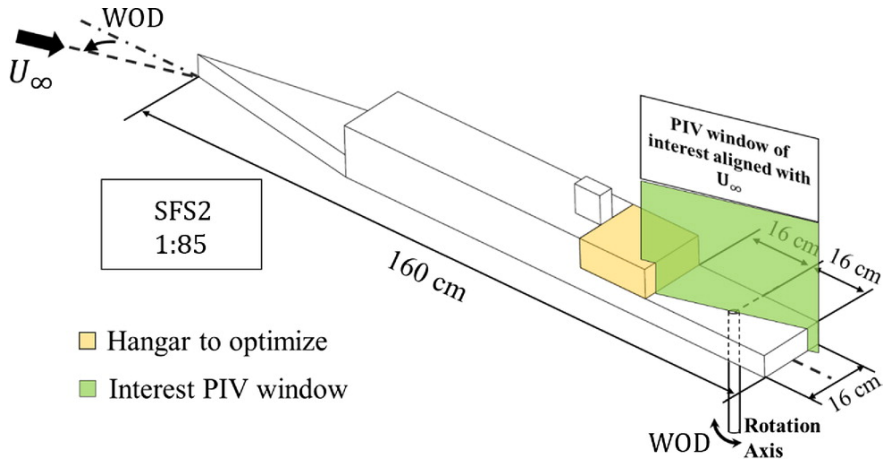

Figure 1.10 Particle image velocimetry region of interest aligned with the free-stream flow across the flight deck of the Simple Frigate Shape No. 2 model [7].

the LDA measurements should be repeated with PIV. Additionally, the descriptions that exist of the yawed airwake vary vastly between different angles, measurement planes, and overall ROI. To characterize the changes within the airwake and to understand the changes introduced by a yaw angle, a more rigorous study is needed. There are unanswered questions related to the flow structures seen on the flight deck and above it. Additionally, what effect does the ABL induce into the yawed airwake, and do the flow features [10] remain the same in such a case? These are some of the gaps that need to be filled for airwakes with different quartering wind conditions.

1.3 Thesis Objectives

A review of prior work on ship airwakes under yawed configurations has highlighted a significant gap in understanding such airwakes. This thesis aims to address several important aspects of this problem. After all, for a pilot landing on a ship, the wind does not always blow from straight-ahead from bow to stern, which may be exceptional. Therefore, high-fidelity dynamic interface (DI) models will require an accurate aerodynamic representation of the ship airwake with yaw. The current section will go into more detail about the overall objectives of this work. Below are the primary objectives that will be addressed in this thesis work:

1. *Quartering Wind Airwake Characterization.* The very basic flow characteristics of the

airwake under quartering wind conditions must be examined first. A common approach is to examine the mean flows, turbulence intensities, and power spectral density (PSD). These metrics can reveal important information about the fundamentals of the airwake. This part will be accomplished through TR-PIV measurements at selected planes. The measurements alone will not be sufficient to categorize the flow—surface oil flow visualization will aid these qualitative measurements. This characterization aims to establish a better understanding of the flow topology in the flight deck region. Once the flow topology is better understood, a deeper look into the turbulent behavior of the airwake can be pursued.

2. *Coherent Structures within the Airwake.* The unsteady, turbulent airwake of a ship consists of recirculating flows, eddies of various scales and energies, and numerous other coherent structures [9, 25]. Part of understanding the turbulent behavior is to first look at the turbulence intensities and the turbulent kinetic energy of the flow, which will be done for the yawed cases and then compared with the headwind case. Because the airwake has coherent structures, a two-point correlation method will be used to examine the changes to these structures under quartering winds. Lastly, proper orthogonal decomposition (POD) methods will be used to look at how the most energetic modes differ for the yawed cases. Alongside two-point correlation, the POD can provide a deeper understanding of how the coherent structures are behaving in the turbulent airwake.

3. *Effects of ABL at Different Quartering Wind Angles.* Simulation of the atmospheric boundary layer (ABL) is important to draw any meaningful comparisons between the experiment and the real flow over the ship. Therefore, the effects of the simulated ABL on the flow will also be investigated. As noted by Seth et al. [10], in the headwind case, the ABL had a small but not insignificant effect on the overall characteristics of the airwake, which suggests that the ship's geometry is a primary driving factor in

the development of the airwake. However, it is still necessary to examine whether this conclusion is valid for the quartering wind cases. Therefore, the effects of the simulated ABL on the turbulence of the quartering wind airwakes will also be investigated.

It is important to note that the present work aims to help establish a more quantitative descriptive understanding of the airwakes with different yaw angles, also known as quartering wind conditions. However, it is anticipated that many details will remain regarding the airwake and its unsteady, turbulent behavior.

1.4 Thesis Outline

Chapter 1 covers the introduction of the present research, as well as the general problem that the work is contributing towards. This is followed by a literature review that primarily focuses on prior research in experimental, computational, and PIV areas that have studied airwakes of ships with quartering winds. Some of the key issues that the thesis will address are mentioned at the end of this chapter.

Chapter 2 will go through the methodology applied for the work done in this thesis. This chapter will provide information on the testing facility, experimental setup, and other details regarding the equipment and testing conditions. The data acquisition and processing will also be covered in this chapter. Lastly, the primary methods used to interpret and analyze the data will be presented.

Chapter 3 documents the results of the research. Oil flow visualization will be covered first, followed by time-averaged velocity flow fields for different crosswise and streamwise planes, for which the turbulence intensities will be presented after. The characterization will conclude with a comparison between the cases with and without ABL. A spectral analysis of two points, one over the flight deck and one behind the funnel, will aim to highlight some of the differences in the energies of the yawed cases. The same points will be used for a two-point correlation to show how the changes in coherent structures. Finally, the analysis will conclude with the outcome of the modal decomposition.

Chapter 4 concludes the research work and summarizes the key findings. This chapter will also provide suggestions for future work related to airwakes of yawed ships. Some of the suggestions will cover experimental approaches, whereas other suggestions will be more focused on providing potential data analysis methods that can be used to better understand the airwake.

2 Methodology

The details of the experiment and data analysis techniques will be covered in this chapter. Measurements of the ship airwake for a 1:90 scale Simple Frigate Shape No. 2 (SFS2) model were carried out at the Embry-Riddle Aeronautical University (ERAU) Low-Speed Wind Tunnel (LSWT) facility. Qualitative surface oil flow visualization was performed first better to understand the flow around different parts of the ship. Subsequently, time-resolved particle image velocimetry (TR-PIV) was used to investigate different crosswise planes and a single streamwise plane. The measurement planes were selected based on notable flow structures observed in the headwind case [12].

Measurements obtained from particle image velocimetry (PIV) provide qualitative results for the in-plane velocity components. These velocity components contain information related to turbulence, which can be interpreted using different approaches. The latter part of this chapter (Section 2.6) is focused on presenting the tools used for data analysis. A more traditional evaluation of the airwake examines the turbulent kinetic energy (TKE), two-point correlation, and the energy spectra at selected points. This is also done for the present work, but a simple proper orthogonal decomposition (POD) analysis is also used to help with the interpretation of coherent structures.

2.1 Low-Speed Wind Tunnel Facility

The airwake measurements were carried out in the Embry-Riddle Aeronautical University (ERAU) Low-Speed Wind Tunnel (LSWT) facility (Fig. 2.1). This facility is a closed-return wind tunnel capable of reaching flow speeds up to $M = 0.38$ (130 m s^{-1} or 425 ft s^{-1}). The test section cross-sectional area is 1.2-by-1.8 m (4-by-6 ft) wide with tapered corner fillets, and it is 3.7 m (12 ft) long. The flow quality within the test section contains turbulence intensities of $< 0.1\%$ of the free-stream velocity for flow speeds below 45.7 m s^{-1} (150 ft s^{-1}), and $< 0.25\%$ for flow speeds below 107 m s^{-1} (350 ft s^{-1}). The flow angularity within the test section is $< \pm 0.2^{\circ}$. Tapered corner fillets counter the development of the boundary layer to ensure that no longitudinal pressure gradient is present over the length of the ship model.

Figure 2.1 Embry-Riddle Aeronautical University's closed-return wind tunnel facility located at the MicaPlex Research Park.

The test section, by area, consists of 65% non-reflective optical-grade glass, which provides excellent flexibility and accessibility for non-intrusive measurements such as PIV. Other features found within the wind tunnel include a heat exchanger, which helps control the flow temperature within certain bounds. The wind tunnel also has a seeding vent that injects smoke into the tunnel. The volumetric density of these seeding particles can be controlled by either adding more or ejecting the smoke outside the facility through the PIV venting system. The wind tunnel interchanges air through small breather slots located downstream of the test section, maintaining the test section at atmospheric pressure.

2.2 Simple Frigate Shape 2 (SFS2)

The Simple Frigate Shape (SFS) models were proposed under a collaborative program for helicopter-ship DI research. The older SFS model was developed in 1985, and the more realistic SFS2 model was developed in 1998 [17]. The SFS models consist of simple angular geometries (Fig. 2.2), making them relatively easy to model for computational applications as well as to manufacture for making measurements in the wind tunnel. Although the models don't represent an actual frigate, they consist of similar flow features observed on a full-scale

Table 2.1 Dimensions of the full-scale and 1:90 scale Simple Frigate Shape No. 2 (SFS2) model in feet.

Scale	Height (ft)	Length (ft)	Width (ft)
1:1	55	455	45
1:90	0.61	5.05	0.5

model, making them valuable for research purposes. As such, the work done in this thesis is for a 1:90 scale SFS2 model. Throughout this thesis, different locations of the SFS2 model are mentioned and referred to, and for orientation these locations are shown in Figure 2.3.

Previous research has been done with the same exact ship model used in this thesis [9, 10, 12]. The model was refurbished with the application of a new low-reflective matte black finish. The model is not smooth, and its surface roughness is equivalent to between 600 and 800 grit. The model was constructed from high-density PVC plastic and mounted to a

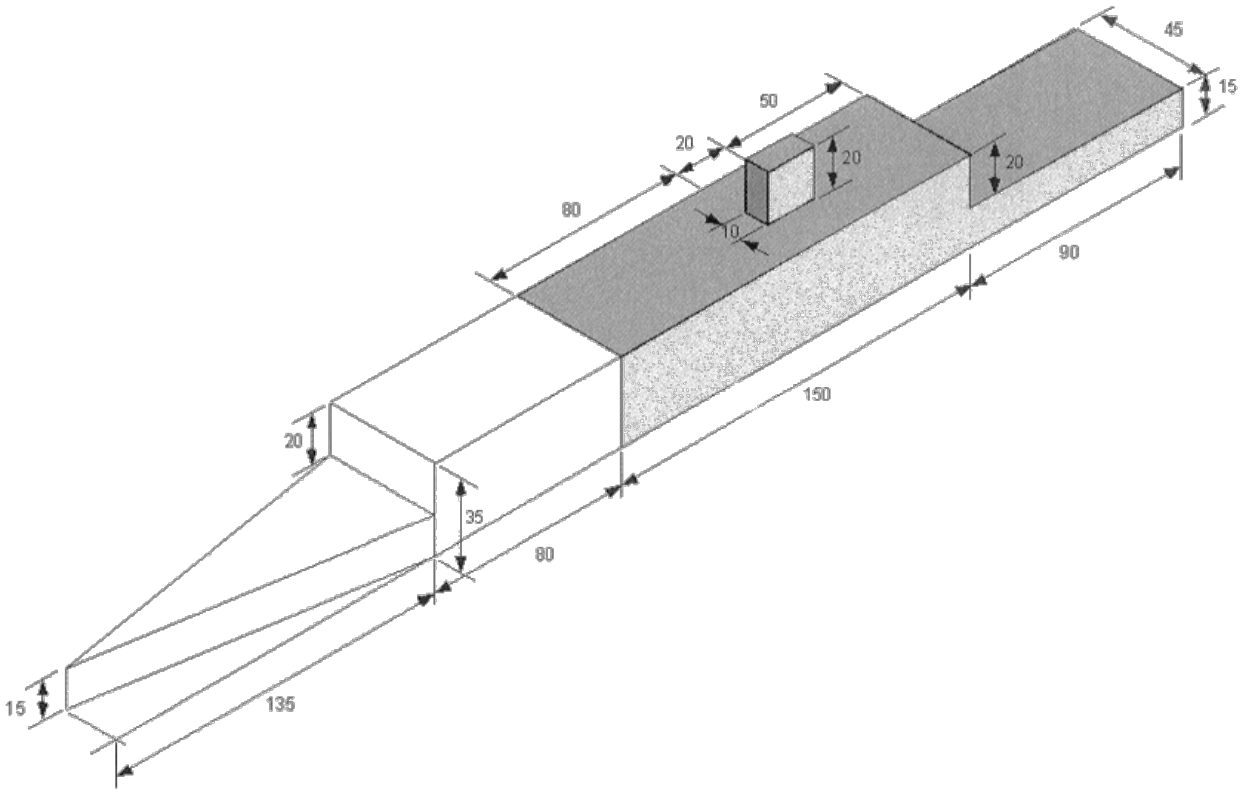

Figure 2.2 Simple Frigate Shape No. 2 (SFS2) model with dimension given in feet. The shaded area represents the preceding Simple Frigate Shape (SFS) model [8].

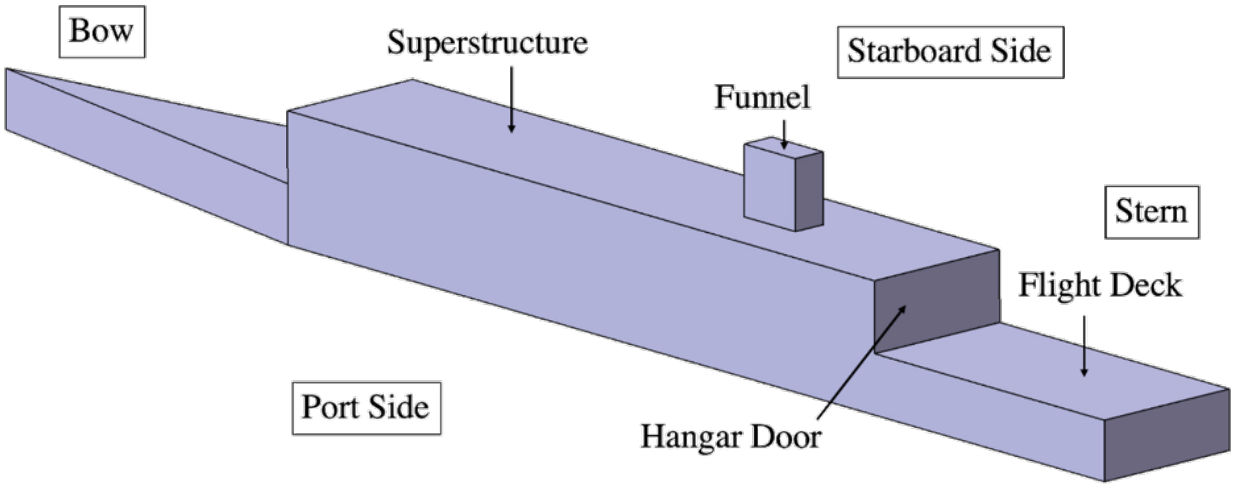

Figure 2.3 Terminology for different locations of the Simple Frigate Shape No. 2 (SFS2) model [9].

precision ground aluminum plate.

The dimensions shown in Fig. 2.2 are relevant, and the primary reference length used was the ship height (SH). The SH of the 1:90 scale model was 0.61 ft (0.186 m), and the other dimensions are given in Table 2.1. Although the primary reference dimension was the ship height, the Reynolds number (Re) was based on ship length. Nevertheless, this section covered the necessary information related to the spatial dimensions and the terminology of the SFS2 model.

2.3 Surface Oil Flow Visualization

Oil flow visualization was the first step of this thesis work. Surface oil flow visualization is primarily used to help identify different topological flow features from signatures left on a surface. This qualitative method can be quite revealing, and combined with other measurement techniques, the overall flow field can be better interpreted and represented topologically.

The visualization was performed by applying a mixture of oil and pigment on the entire ship model when the wind was off. After turning on the tunnel and reaching the desired flow speed, the surface features start to develop under the action of the surface shear stresses. This

development happens until most of the oil is no longer on the surface, and a time-averaged flow pattern forms. The patterns observed on the surface leave streaks of the pigment behind. Some portions of the surface will have more oil accumulated than others, which indicates regions of lower shear where separation, recirculation, or stagnation occurs. These results were then photographed from different angles and locations under normal lighting conditions but with various camera lens combinations. A high contrast surface, such as a matte-black finish, aids with the quality of the images.

Some challenges with oil flow present themselves in choosing the right mixture. The oil is required to have the appropriate viscosity and the right concentration of pigment particles. Hence, the method involves some trial and error in getting the right amounts of each ingredient [26]. The mixture used for this work consisted of a clear mineral oil with cosmetic grade Titanium Dioxide (TiO_2). Cosmetic grade TiO_2 has smaller particles than paint grade, which dissolve easier. To reduce the surface tension then a small amount of oleic acid (olive oil) was added to the mixture. The container with the oil mixture requires frequent mixing to avoid letting the TiO_2 particles settle out at the bottom. After starting the tunnel, the oil is blown away from the surface and mostly the TiO_2 particles are left. In practice, however, oil will pool in certain areas and continuing to keep the tunnel on will not change the end result. Therefore, the method requires a quick and an appropriate amount of mixture be applied onto the surface; too little will result in poor quality of the patterns and too much will result in the patterns being spoiled by the residual oil from pooling.

2.4 Simulated Atmospheric Boundary Layer

The atmospheric boundary layer (ABL) must be taken into account in any ship airwake study. Indeed, most investigators will argue that a representative scaling of an actual ABL is a prerequisite to study the effects on the airwake [10]. The simulated ABL in the present work was identical to the previous studies performed by Seth [11] and Zhu [12].

As shown in Fig. 2.4a, the velocity profile reaching the ship model in the wind tunnel closely followed a classic 1/7th power law, indicating a sufficient development of a fully-

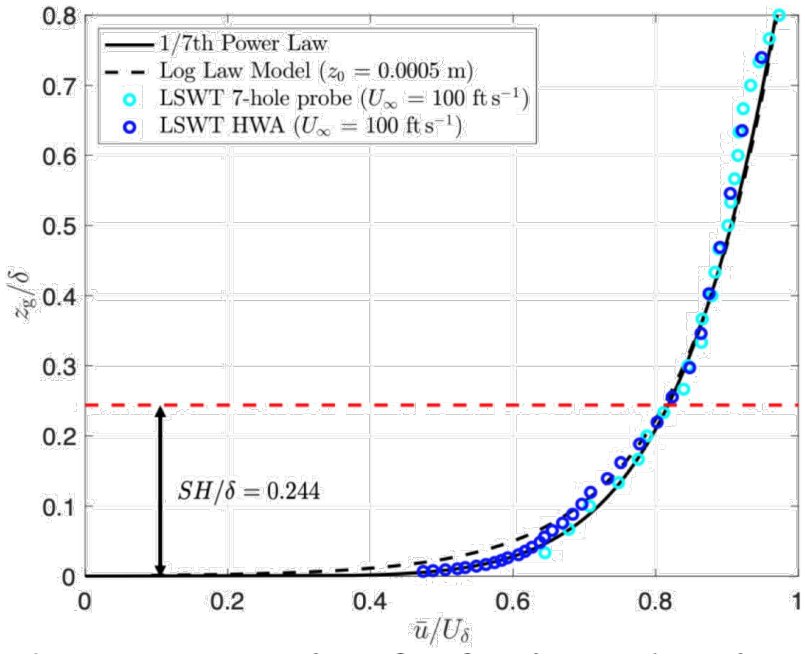

(a) Mean velocity profile compared with the 1/7th power law [10].

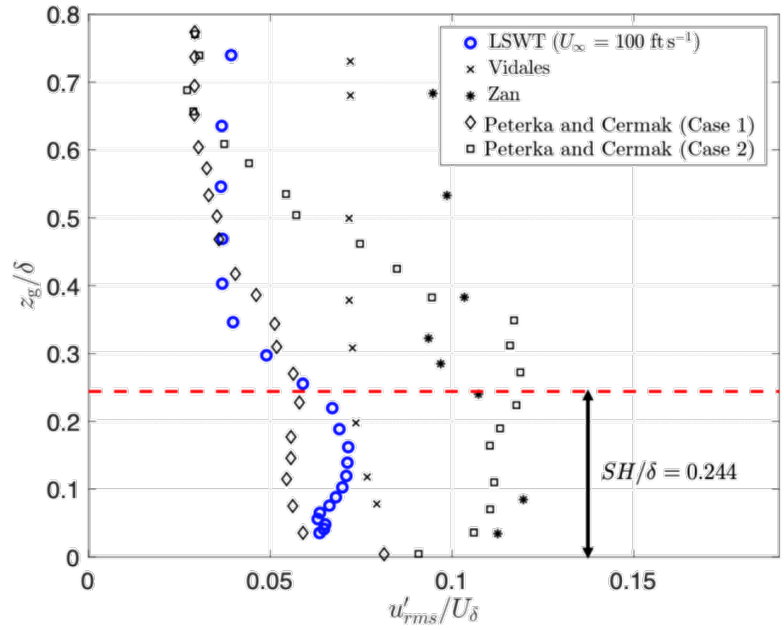

(b) Turbulence intensity of the simulated atmospheric boundary layer (ABL) compared with wind tunnel results from literature [10].

Figure 2.4 The mean velocity profile and turbulence intensity of the simulated atmospheric boundary layer (ABL) in the Embry-Riddle Aeronautical University (ERAU) Low-Speed Wind Tunnel (LSWT) facility used for present work. The ABL measurements were done by Seth et al. [10].

developed turbulent boundary layer. After reaching the test section, the boundary layer did not vary much in the streamwise and spanwise directions, thereby allowing the ship model to be yawed and moved upstream or downstream.

The turbulence intensity of the ABL is important for the ship airwake study. Strong turbulent boundary layers can affect the structures seen inside the airwake. Therefore, it is required to achieve a representative magnitude and distribution of turbulence in any simulated ABL. The turbulence intensity of this simulated ABL (Fig. 2.4b) was compared to previous studies found in the literature. Overall, the results are representative of the ABL and in general bounds of what can be achieved in wind tunnels. The effects of this simulated ABL on the ship airwake will be further discussed in Chapter 4 of the present thesis.

2.5 Time-Resolved Particle Image Velocimetry

The present section provides additional details of the overall experimental setup, specifically involving PIV. Some of the details include the physical setup of the experiment, test cases and conditions for the measurements, selection of regions of interest, data processing software and settings, and uncertainties related to the measurements.

Measurements of the airwake were performed by using two different PIV methods: stereoscopic and planar. The primary difference between these two methods is in the number of velocity components resolved. Stereoscopic PIV can resolve all three velocity components, whereas planar PIV can only resolve two. Although stereoscopic PIV provides three-component velocity, it does so only for a single plane. Thus, gradients normal to the measurement plane cannot be resolved unless several light-sheet planes are recorded simultaneously [19]. Nevertheless, in the case of the ship airwake, a stereoscopic PIV measurement for a single plane can provide valuable information. The airwake consists of highly unsteady and turbulent regions with recirculation; three-component velocity measurements can qualitatively capture the locations where these phenomena occur. Lastly, the time-resolved aspect of PIV only applies to the larger scale turbulence in the current work.

2.5.1 Experimental Setup

In total, eight different configurations were used. Table 2.2 shows the different configuration definitions for referencing purposes. The configurations are defined based on three different criteria: type, with or without ABL, and yaw angle. Stereoscopic PIV is type 1, and planar is type 2. The decimal point indicates the yaw angle, where '.1' is for $\psi = 10°$, and '.2' is for $\psi = 20°$. Lastly, the letters refer to whether the ABL was included in the measurements or not. The letter 'A' after the number refers to a case with ABL, and the letter 'B' refers to a case without ABL.

The equipment used for each setup was the same. However, for the cases with ABL, two sets of Cowdrey rods were used, as shown in Fig. 2.5. The larger first set was located right after the turbulence screens at the start of the settling chamber. The rods for the first set were hollow PVC pipes. The smaller second set was located at the end of the contraction chamber, immediately before the test section inlet. These two sets of Cowdrey rods create a velocity gradient and turbulence in the incoming flow. The exact positioning and height of these Cowdrey rods is based on the work done by Seth [11].

The settling chamber had seeding inlet through which the aerosol particles are injected into the wind tunnel. The oil-based seeding particles were generated using a smoke generator and had a nominal diameter of 0.2 μm measured by calibration. Compressed air was used to overcome the pressure inside the wind tunnel and assist with the injection of the seed particles. This seeding procedure was carried out at low wind speeds of around 3.5 m s^{-1} (or

Table 2.2 Different measurement setup configurations.

Configuration	**TR-PIV Type**	**ABL**	$\boldsymbol{\psi}$
1.1A	Stereoscopic	Yes	10°
1.1B	Stereoscopic	No	10°
1.2A	Stereoscopic	Yes	20°
1.2B	Stereoscopic	No	20°
2.1A	Planar	Yes	10°
2.1B	Planar	No	10°
2.2A	Planar	Yes	20°
2.2B	Planar	No	20°

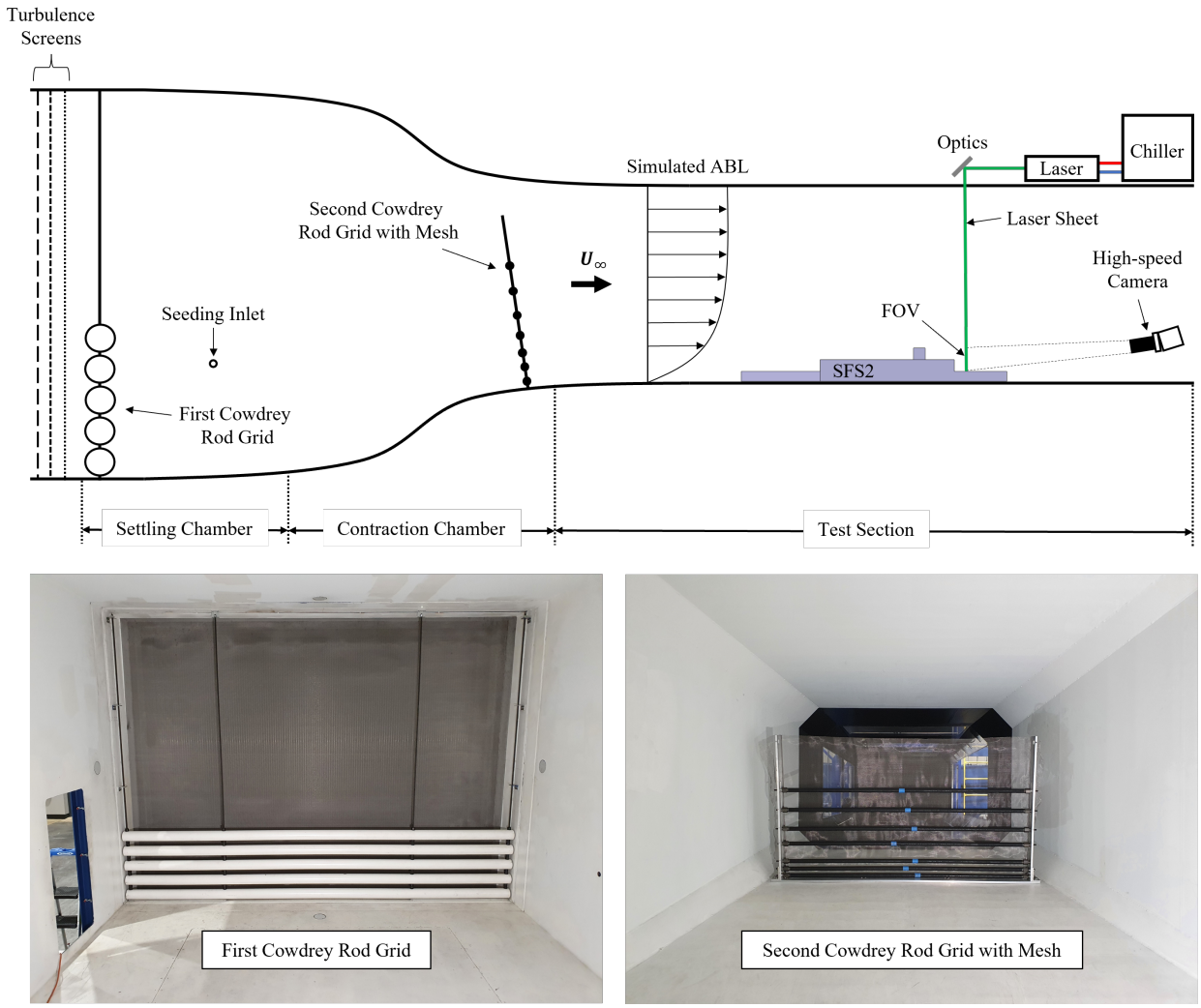

Figure 2.5 Overview of entire particle image velocimetry (PIV) setup with atmospheric boundary layer (ABL). The schematic shows a stereoscopic PIV configuration for both 1.1A and 1.2A (Table 2.2), and the diagram is based on the work done by Seth [11] and Zhu [12].

10 ft s^{-1}) to keep the air moving inside the tunnel and speed up the mixing process. Once the desired concentration is achieved, the valves connected to the seeding inlet were closed.

The entire seeding process takes around 5 minutes. As mentioned in Section 2.1, if the tunnel has too much smoke, the PIV venting system can purge it outside, which helps control the desired concentration required for PIV. Throughout the experiment, some of the smoke leaks outside into the tunnel hall and so causes its concentration to change. To account for this, quick sample PIV snapshots are taken before each test case to check the image quality. Based on these samples, if the concentration is inadequate then more smoke was added.

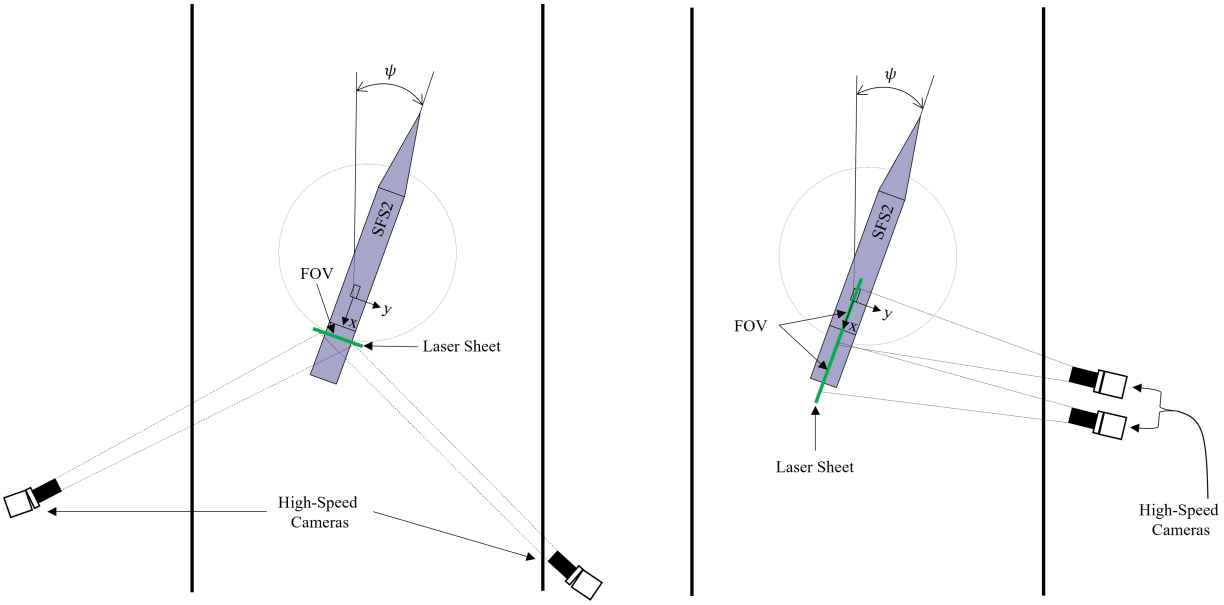

(a) Stereoscopic time-resolved PIV setup. *(b)* Planar time-resolved PIV setup.

Figure 2.6 Time-resolved particle image velocimetry (PIV) setup for crosswise (Fig. 2.6a) and streamwise (Fig. 2.6b) planes for the Simple Frigate Shape No. 2 (SFS2) model.

Figure 2.6 shows the two different measurement types used for the present work. It is necessary to address the stereoscopic PIV setup (Fig. 2.6a & 2.7) and its relatively large oblique angle with the starboard side camera. The cameras remained in a fixed position for each configuration; however, they were turned when the optics were moved to a different plane. This approach resulted in an angle between the cameras and the measurement plane that changed based on the test case.

For configurations 1.1A and 1.1B the starboard side camera angle varied between 55°–58°, and the port side camera varied from 38°–42°, depending on the measurement plane. Similarly, for configurations 1.2A and 1.2B, the starboard side camera varied between 58°–67°, and the port side camera varied from 25°–28°. These are unusually large angles for stereoscopic PIV measurements. Nevertheless, the software used for calibration and data acquisition was able to resolve velocity vectors even at such high oblique angles.

For all configurations, the PIV experiments were carried out using high-speed, 4-megapixel CMOS cameras. Apart from the different position, the main difference involving the cameras

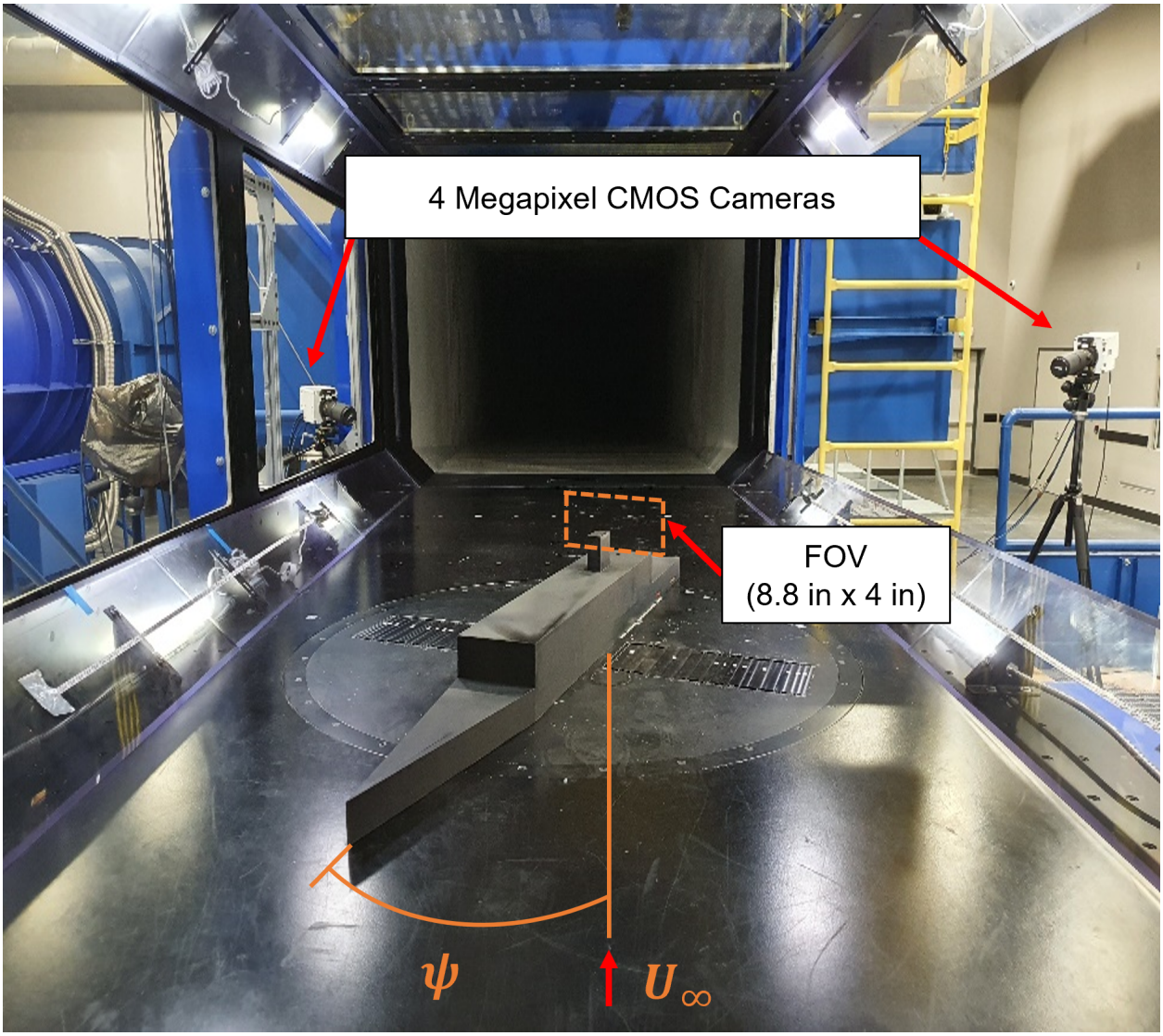

Figure 2.7 Stereoscopic time-resolved particle image velocimetry (TR-PIV) setup from inside the test section.

between the stereoscopic and planar PIV measurements was the focal length. Stereoscopic configurations (Fig. 2.6a) had a focal length of 200 mm for both cameras, whereas the planar configurations had a focal length of 105 mm. A focal length of 200 mm was not sufficient for the desired field of view in the planar cases. Instead, for planar PIV, two cameras were used with a small overlapping region that was stitched into a single image. The field of view was fairly large for the planar configurations; it covered a region from the start of the funnel towards the end of the flight deck (Fig. 2.6b).

Table 2.3 Experiment parameters for time-resolved particle image velocimetry (TR-PIV) measurements for 1.1A–1.2B configurations (Table 2.2).

Speed	***Re***	**Δt w/o ABL**	**Δt w/ ABL**	**Number of images**	**Image rate**	**Sample period $10°/20°$**
(m s^{-1} / ft s^{-1})	**(10^6)**	**(μs)**	**(μs)**	**($10°/20°$)**	**(Hz)**	**(s)**
30.5 / 100	3.2	10	14	8,000 / 9,000	500	16 / 18
45.7 / 150	4.8	8	12	8,000 / 9,000	500	16 / 18
61.0 / 200	6.4	5	10	8,000 / 9,000	500	16 / 18

Table 2.4 Experiment parameters for time-resolved particle image velocimetry (TR-PIV) measurements for 2.1A–2.2B configurations (Table 2.2).

Speed	***Re***	**Δt w/o ABL**	**Δt w/ ABL**	**Number of images**	**Image rate**	**Sample period**
(m s^{-1} / ft s^{-1})	**(10^6)**	**(μs)**	**(μs)**		**(Hz)**	**(s)**
30.5 / 100	3.2	30	20	7,500	500	15
45.7 / 150	4.8	20	15	7,500	500	15
61.0 / 200	6.4	10	10	7,500	500	15

For the stereoscopic configuration, the FOV varied by very little as a result of different measurement plane positions on the flight deck. The FOV for the stereoscopic configurations was around 8.8-by-4 inches (or 22-by-10 centimeters). Additionally, to help correct the distorted focus caused by large oblique angles, for the stereoscopic configuration the lenses were mounted on Scheimpflug mounts. The camera resolution varied for the different configurations. Configurations 1.1A & 1.1B had a resolution of 2048-by-1452, and configurations 1.2A & 1.2B had resolutions of 1920-by-1600. The planar configurations had the full resolution of the CMOS cameras, which was 2560-by-1600. This resulted in a spatial resolution of around 0.11 mm/pixel, with an average pixel displacement between 1–5 pixels. Lastly, all cameras operated at an aperture of f/4 to maximize the brightness of the images.

The source used to illuminate the particles was a dual-head, 30 mJ/pulse, 527 nm Nd:YLF laser. The equipment surrounding the laser setup is shown in Fig. 2.9a, which is located on top of the test section. A different perspective is shown in Fig. 2.9b, which is similar to the overview schematic (Fig. 2.5). The setup consists of the laser head, laser controller, and the chiller. During operation, the laser is liquid cooled by the chilling system, and can be

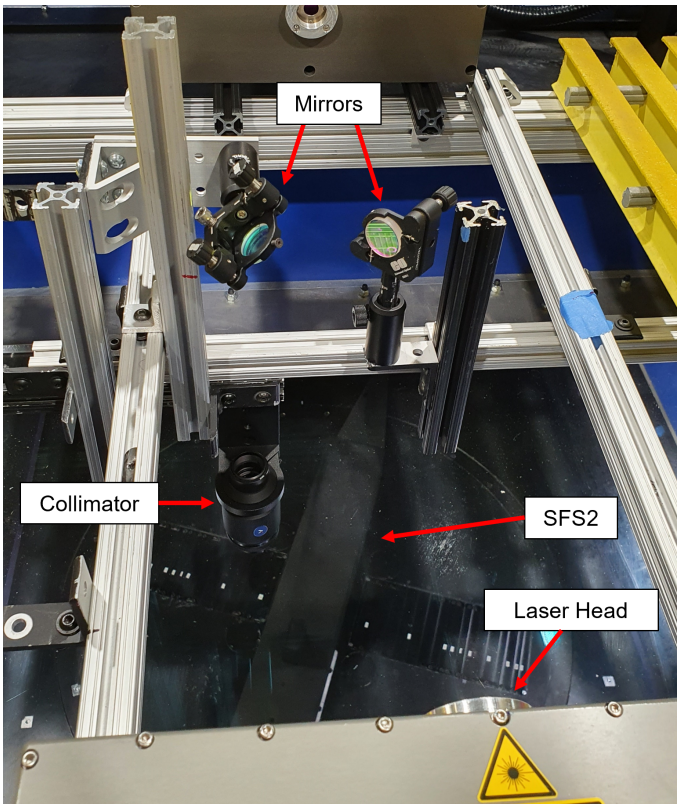

Figure 2.8 Optical setup that directs the laser beam towards the desired measurement plane.

controlled either manually through the laser controller or through a software on the data acquisition computer.

Once turned on, the laser beams encounter an optical setup comprised of small mirrors organized in such a way that the laser sheet reflects down onto the plane of interest, shown in Fig. 2.8. This optical setup can be adjusted according to the desired measurement plane, allowing the laser, cameras, and the field of view to stay in a fixed position. The laser sheet thickness and focus can be altered through a collimator, which is positioned to be the final optical device before the sheet illuminates the measurement plane. During the experiment, the laser and camera synchronization was controlled by a programmable timing unit (PTU).

The different experimental parameters are given for each configuration in Table 2.3 and Table 2.4. The number of images was different for $\psi = 10°$ and $\psi = 20°$ in Table 2.3 because the camera resolutions were different. Configurations 1.1A and 1.1B used a higher camera resolution causing more camera memory to be needed. In turn, this resulted in fewer images.

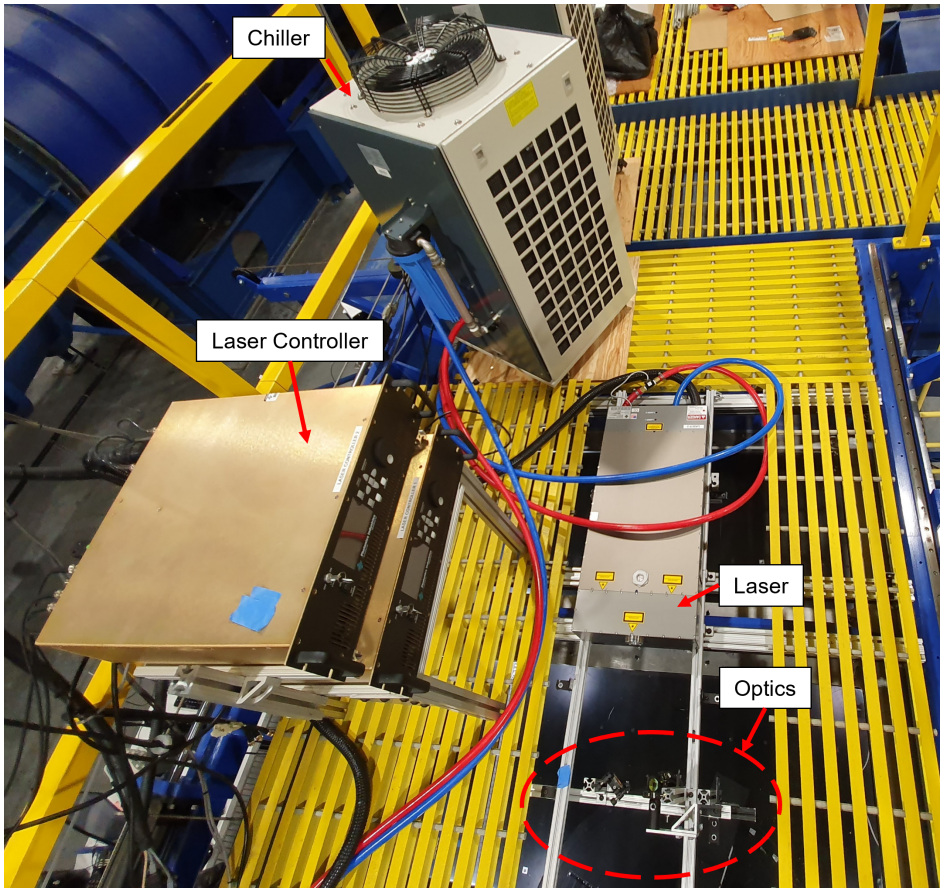

(a) Laser equipment setup on top of the test section.

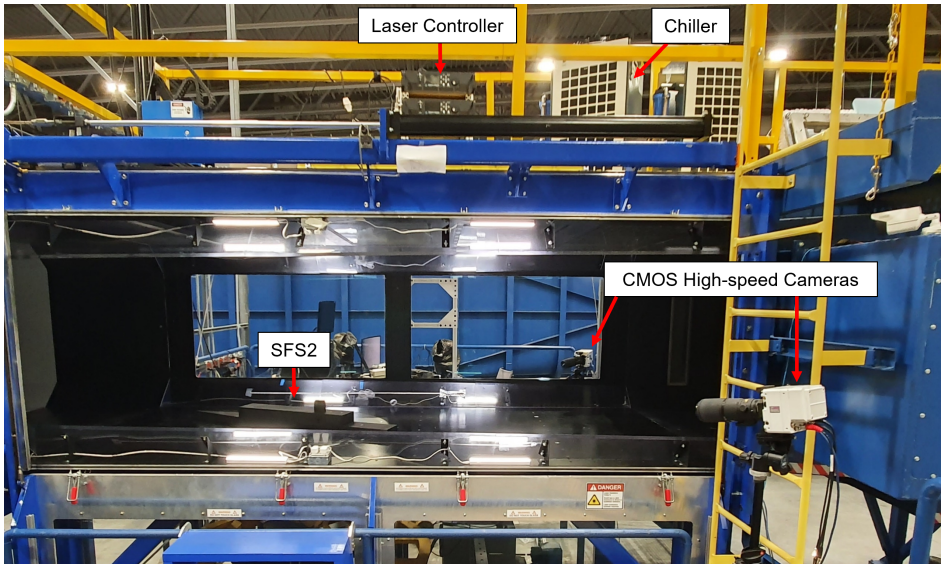

(b) Side view of the experimental setup. Cameras are arranged as shown in Figure 2.6a.

Figure 2.9 Layout and equipment of the particle image velocimetry (PIV) setup.

However, the reason for the larger Δt in the cases without ABL in Table 2.4 was related to pixel displacement. The change was made in hopes to capture a better pixel displacement, and slight improvements were seen. A higher Δt could be explored for future test runs with ABL. The large numbers of images are related to the time dynamics. From previous studies [4, 9, 10], certain time-dependent behaviors have been observed in the SFS2 airwake. Thus, a larger sample time provides a better opportunity to capture these time dynamics within the flow. However, this comes at a lower sampling frequency, which will result in aliasing some of the higher frequency content. The choice was made deliberately, since the flight deck region has significant turbulent energy in the low frequency range of 0.2–2 Hz [24].

2.5.2 Regions of Interest

The PIV measurements were carried out for three different crosswise planes and a single streamwise plane, as shown in Fig. 2.10. These regions of interest (ROI) were chosen based on previous findings by Zhu [12] and Seth [11]. The crosswise planes were located in areas that involve important flight deck flow structures.

The first ROI was a crosswise plane that was located on top of the superstructure and captured the funnel wake region. In the headwind case, horseshoe vortices were observed in this region. The second ROI was a crosswise plane that was located in the area of the recirculation region. This recirculation region showed a bistable flow behavior when the yaw angle was very small or close to zero [4, 9]. Lastly, the third ROI was a crosswise plane that was located towards the end of the flight deck. At that location, the recirculation region was no longer present, but its effects still prevailed. In the headwind measurements, flight deck vortices were captured in this last crosswise plane. As for the streamwise plane, it intersects all three crosswise planes and covers the centerline region of the funnel wake and the flight deck.

It is necessary to point out that all regions of interest are on the longitudinal body axis of the SFS2 as opposed to being parallel to the free-stream frame as was done by Mora et al. [7]. The objective of these measurements was to help understand the ship airwake

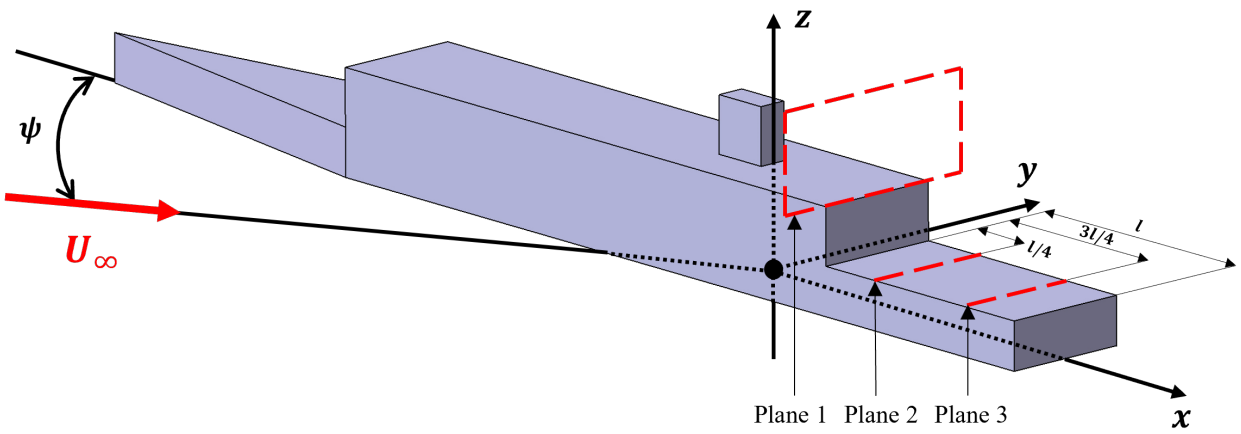

(a) Stereoscopic TR-PIV crosswise plane locations.

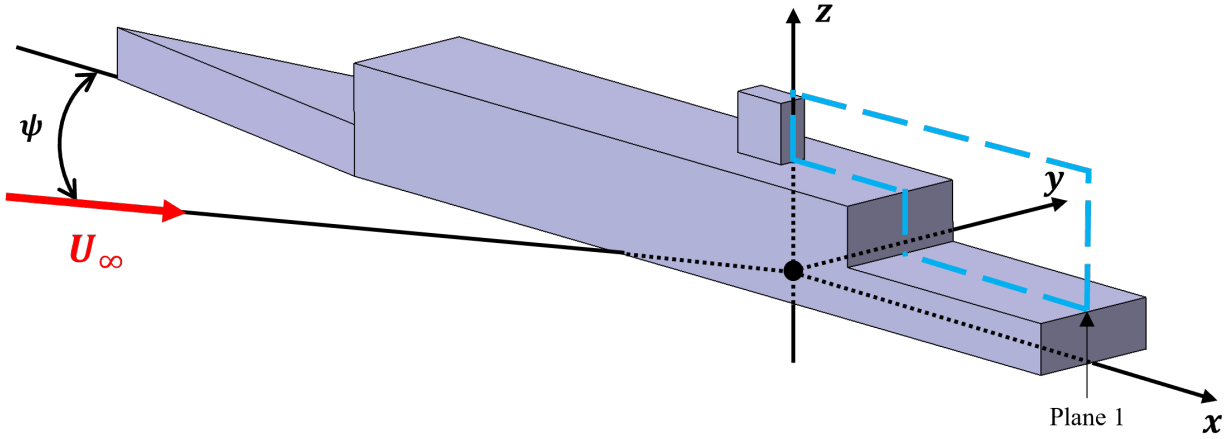

(b) Planar PIV streamwise plane locations.

Figure 2.10 Regions of interest for time-resolved particle image velocimetry (TR-PIV) measurements of the Simple Frigate Shape No. 2 (SFS2) airwake.

encountered by an operating aircraft. In a yawed setting, the overall ship airwake will be on the leeward side (Fig. 1.7), but specific flow structures will also be present over the flight deck. Therefore, it is essential to understand and capture these differences and changes within the flow. Additionally, a direct comparison to the headwind case is made in the present work. The headwind measurements had a similar ROI, resulting in a more convenient qualitative comparison.

2.5.3 Data Processing

Data acquisition and processing were conducted using the commercially available LaVision software, DaVis. The software was used during all stages of the measurement process, starting from making calibration images to acquiring the data and finally processing the raw images.

For the stereoscopic PIV measurements, a 309-15 calibration plate provided by LaVision was used to calibrate the ROI. This plate consisted of equally spaced dots that helped the software track the particle movement. The dots were 3 mm (0.12 in) in diameter and 15 mm (0.59 in) apart. The plate had two levels that differed in depth, and this difference was 3 mm (0.12 in). A pinhole mapping function was used during the calibration process. A custom calibration plate was used with a single level for the planar PIV measurements. The dots in this plate were 5 mm (0.197 in) in diameter and spaced 10 mm (0.39 in) apart. A polynomial mapping function was used to calibrate the images for the planar PIV case.

The raw images included regions where the laser did not illuminate the particles. During the processing, these regions were removed by an applied geometric mask that defined the FOV. A filter was applied to all the images to subtract the average background noise from the cameras and laser reflections. The vector calculation was defined by an interrogation window, which specified the spatial resolution. For all results, this interrogation window was set to 128-by-128 with 50% overlap for the initial pass and 48-by-48 with 75% overlap for the two final passes. A universal outlier detection was used to remove vectors that had a peak ratio of less than 1.5 in a filter region of 3-by-3 with a minimum of 5 vectors. The filter removed outliers with residuals greater than two and reinserted them if the residual was less than 3 in the following passes. The maximum expected displacement of the particles was set to 8 pixels. Lastly, empty spaces where vectors could not be resolved were filled in with interpolation. The software calculated an average of all the non-zero vectors surrounding the empty space and filled in the empty area with an interpolated vector [27].

2.5.4 Uncertainties in the Measurements

Measurements are not exact and contain inherent uncertainties. These uncertainties originate from various sources, such as: camera and laser sheet alignment, particle density or size, calibration, image brightness, etc. The quartering wind measurements over the SFS2 flight deck had significant oblique angles. Thus, it is necessary to acknowledge the uncertainties of these measurements to understand how representative the obtained results are of the actual airwake.

The uncertainties were calculated by DaVis 10.2. The method consists of a statistical analysis of how each pixel contributes to the cross-correlation peak shape, from which the uncertainty of the displacement vector is derived [27, 28]. The obtained uncertainties were scalar values in different units of velocity. Overall, the software was able to resolve the velocities with relatively small uncertainties, as shown in Fig. 2.11. Nevertheless, all velocity components did not have the same uncertainty. The spanwise and wall-normal velocity components had significantly larger uncertainties when compared to the streamwise velocity. For all crosswise planes, majority of the FOV points had uncertainties below 1%, with some regions having higher uncertainties as seen in Fig. 2.11a & I.3. This was observed for all configurations, and additional uncertainties for $\psi = 10^{\circ}$ are shown in Appendix I.

A notable observation related to uncertainties involves the measurements at near-wall regions. In Appendix I, the spanwise and wall-normal velocities have high uncertainty values in regions close to the surface. For PIV configurations used in the present work, this is an expected outcome. The fidelity of the results at near-wall regions is not very high, which presents higher uncertainty values in these locations, as seen in Fig. I.1 through I.5.

2.6 Data Analysis Methods

This section covers different techniques used for data analysis. The focus of these techniques is placed on the turbulent behavior of the flow. Thus, the most common tools used to investigate turbulent behavior in the ship airwake study are present in the current work. The section will briefly introduce the background of turbulent kinetic energy (TKE),

two-point correlation, power spectral density (PSD), and proper orthogonal decomposition (POD) methods.

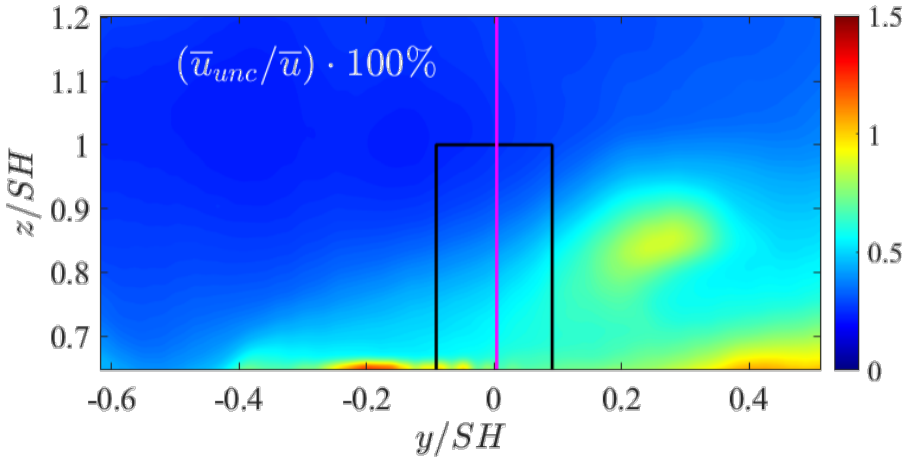

(a) Crosswise Plane 1 uncertainty contour of $\overline{u}_{unc}$ normalized to $\overline{u}$, where the magenta line is the location of uncertainties shown in Fig. 2.11b.

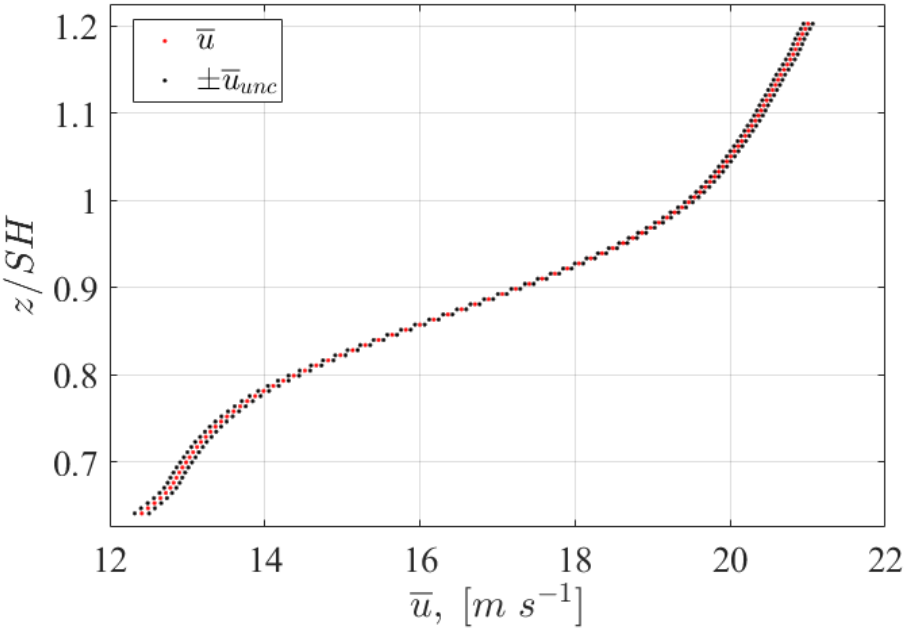

(b) The uncertainty of $\overline{u}$ for crosswise Plane 1 located at the magenta line in Fig. 2.11a.

Figure 2.11 Crosswise Plane 1 streamwise velocity uncertainties calculated by DaVis 10.2 for configuration 1.1A (Table 2.2).

2.6.1 Turbulent Kinetic Energy (TKE)

Turbulent kinetic energy is widely used to obtain an insight of the turbulent behavior. The technique helps identify regions of energetic fluctuations within the flow, or quantify the turbulence intensity of specific velocity components. Generally, the TKE is normalized to the free-stream velocity to obtain a nondimensional value, which allows a better comparison between different cases. In the present work, the ABL lowers the free-stream velocity captured within the FOV, which requires an appropriate choice for the free-stream value. For all cases, the reference free-stream value was the velocity set inside the test section. Thus, even if the cases with ABL had a lower overall velocity throughout the FOV, the normalization choice was the test section free-stream velocity. Additionally, the contours related to TKE will show the time-averaged results. The TKE is defined as

$$k = \frac{1}{2}\left(\overline{u'u'} + \overline{v'v'} + \overline{w'w'}\right) \tag{2.1}$$

For certain cases, all three velocity components were not available. Therefore, only two components were used to calculate the TKE. Individual velocity fluctuation components were also used to find the turbulence intensity contours for different regions of interest. Turbulence intensity describes the standard deviation of random velocity fluctuations, and it is defined as I, given by

$$I_{u_i'} = \frac{\sqrt{\overline{u_i'^2}}}{U_{ref}} = \frac{u_{i,rms}}{U_{ref}} \tag{2.2}$$

where u_i' denotes a velocity fluctuation component u', v', or w', which can be found by subtracting the mean from the instantaneous velocity

$$u_i' = u_i - \overline{u}_i \tag{2.3}$$

As mentioned before, the reference velocity U_{ref} was used for nondimensionalization, and it was always set as the free-stream value U_∞.

2.6.2 Two-Point Correlation

Two-point correlation measures the change of two variables with respect to one another. If the variation between the two variables is small that would suggest a high correlation. Likewise, if the variation is high, then the two variables would not be correlated. In turbulence, two-point statistics are useful in characterizing the behavior of coherent motion [29]. Effectively, two-point correlation can be used to study whether a coherent structure is passing through the two selected spatial locations. The two-point correlation is defined as

$$R_{ij}(\boldsymbol{x}, \boldsymbol{\Delta x}) = \frac{\langle u_i'(\boldsymbol{x}) u_j'(\boldsymbol{x} + \boldsymbol{\Delta x}) \rangle}{\sqrt{\langle u_i'^2(\boldsymbol{x}) \rangle} \sqrt{\langle u_j'^2(\boldsymbol{x} + \boldsymbol{\Delta x}) \rangle}} \tag{2.4}$$

where u_i' and u_j' denote the different velocity fluctuations ($i, j = 1, 2, 3$), in which the indices refer to the streamwise (x-direction), spanwise (y-direction), and wall-normal (z-direction) components. The reference spatial location is given by $\boldsymbol{x} = (x_1, x_2, x_3)$, and the constant variation with respect to $\boldsymbol{x}$ is given by $\boldsymbol{x} + \boldsymbol{\Delta x} = (x_1 + \Delta x_1, x_2 + \Delta x_2, x_3 + \Delta x_3)$. Lastly, the angled brackets $\langle \cdot \rangle$ denote an ensemble average. In the current work, two-point correlation is used to investigate the Reynolds stresses in the streamwise plane, which spans from the funnel towards the end of the flight deck (Fig. 2.10).

2.6.3 Power Spectral Density (PSD)

The highly unsteady and turbulent ship airwake involves flow structures of different scales. One way to investigate these different scales is to study their frequency content. As mentioned in Section 1.2.3, the airwake is primarily dominated by low-frequency flow structures. Thus, a tool capable of decomposing the data into its frequency content is desired. In the study of turbulence, the power spectral density allows the assessment of such content, especially when random effects, such as fluctuations, are present [30].

Spectral analysis was performed for two points in streamwise Plane 1 (Fig. 2.10). The first point was located within the funnel wake region, and the second point was above the flight deck. These points were treated as midpoints, and the immediate eight surrounding

points were used for further smoothing of the results. The smoothing was achieved by taking an average of the nine total points. The power spectral density was calculated using a Filtering–Squaring–Averaging method [31], which involves a Fast Fourier Transform (FFT) of the time signal. Further smoothing was done by including a bandpass filter of 256 Hz bandwidth with a 50% overlapping window. Lastly, in the present work, the power spectra was normalized to U_∞^2.

Frequency of the turbulent content is highly relevant for the ship airwake problem, and it is necessary to address the resolvable frequency from the PIV measurements. A Strouhal scaling can be performed to relate the model-scale frequency content to the full-scale frequency content. The Strouhal number is defined as

$$St = \frac{fSH}{U_\infty} \tag{2.5}$$

where f is the frequency, SH is the ship height, and U_∞ is the free-stream velocity. The free-stream conditions for the full-scale ship can be assumed to be 35 knots (18 m s^{-1}) [24], and knowing that the model is at a scale of 1:90, the frequency of the full-scale ship can be calculated. The Strouhal scaling is

$$\frac{St_{fs}}{St_{ms}} = \left(\frac{f_{fs}}{f_{ms}}\right)\left(\frac{SH_{fs}}{SH_{ms}}\right)\left(\frac{U_{\infty,ms}}{U_{\infty,fs}}\right) = 1 \tag{2.6}$$

where the subscripts "fs" and "ms" denote the full-scale and model-scale values. Using a tunnel speed of $U_{\infty,ms} = 30.48$ m s^{-1}, and knowing that the sampling rate was $f_s = 500$ Hz, the resolvable Nyquist frequency is $f_{ms} = 250$ Hz. Thus, assuming normal operating conditions, an approximation of the full-scale frequency can be calculated

$$f_{fs} = f_{ms}\left(\frac{SH_{ms}}{SH_{fs}}\right)\left(\frac{U_{\infty,fs}}{U_{\infty,ms}}\right) \tag{2.7}$$

The maximum resolvable Strouhal number for this case is $St = 1.53$. According to Shukla

et al. [17], the dominant vortex shedding frequency for a full-scale ship lies in the range of $St \in [0.16, 0.25]$. Therefore, the PIV measurements are capable of resolving the dominant frequencies within the airwake, and PSD will be used to interpret the results.

2.6.4 Proper Orthogonal Decomposition (POD)

Turbulent flow fields contain disorder and randomness that can be challenging to interpret. Proper orthogonal decomposition was introduced by Lumley [32] to decompose the random turbulent flow field into a set of deterministic functions that represent a portion of the total fluctuating kinetic energy in the flow [33]. Through these deterministic functions, some information about the coherent structures within a turbulent flow field can be observed. The POD is a statistical approach, and in the field of statistics, it is called the principal component analysis (PCA). Although there are different names, the method is based on the singular value decomposition (SVD) of a non-square matrix.

Considering a data set matrix $\boldsymbol{U}$ with n-rows of flow field values and m-columns of different time instances ($n >> m$), the singular value decomposition factorizes the real n-by-m data set matrix into

$$\boldsymbol{U} = \boldsymbol{\Phi}\boldsymbol{\Sigma}\boldsymbol{R}^T \tag{2.8}$$

where $\boldsymbol{\Phi}$ is an n-by-m spatial basis matrix containing the different modes ranked in order from the most energetic to the least energetic. The singular value matrix $\boldsymbol{\Sigma}$ is of size m-by-m, and contains the singular values ranked in an order from highest to lowest. Lastly, the matrix $\boldsymbol{R}$ is of size m-by-m and includes information related to the time dynamics of the flow. From the singular value decomposition, the data set matrix $\boldsymbol{U}$ can be reconstructed in a truncated manner using a desired number of spatial modes.

The relation between POD and SVD is further seen by examining the covariance matrix $\boldsymbol{C}$ and correlation matrix $\boldsymbol{C_s}$. Computing matrices $\boldsymbol{C}$ and $\boldsymbol{C_s}$ using the relation from Eq. 2.8

results in

$$\begin{aligned} \boldsymbol{C} &= \boldsymbol{U}^T\boldsymbol{U} \\ &= \boldsymbol{R}(\boldsymbol{\Sigma}^T\boldsymbol{\Sigma})\boldsymbol{R}^T \\ &= \boldsymbol{R}(\boldsymbol{\Sigma}^2)\boldsymbol{R}^T \end{aligned}$$

and similarly,

$$\begin{aligned} \boldsymbol{C_s} &= \boldsymbol{U}\boldsymbol{U}^T \\ &= \boldsymbol{\Phi}(\boldsymbol{\Sigma}\boldsymbol{\Sigma}^T)\boldsymbol{\Phi}^T \\ &= \boldsymbol{\Phi}(\boldsymbol{\Sigma}^2)\boldsymbol{\Phi}^T \end{aligned}$$

it can be seen that the non-zero diagonal elements of the matrices $\boldsymbol{\Sigma}\boldsymbol{\Sigma}^T$ and $\boldsymbol{\Sigma}^T\boldsymbol{\Sigma}$ are exactly the same, and they are the squares of the singular values of $\boldsymbol{U}$ [33]. Algorithmically, SVD is a faster way of calculating POD.

3 Results & Discussion

Results from the time-resolved particle image velocimetry (TR-PIV) measurements will be covered in the current chapter. The flow field of quartering wind cases will be established through oil flow visualization, time-averaged velocity contours, and the study of coherent motion within the airwake. The chapter will proceed by covering the surface oil flow visualization results first, revealing the differences between the headwind and quartering wind cases. Following the qualitative oil flow results, Reynolds number independence will be shown for the quartering wind cases. The chapter will continue with the time-averaged airwake results without the effects of the simulated atmospheric boundary layer (ABL), which includes the velocity and turbulent fluctuation contours that form a basis for further comparisons. Afterwards, effects of the simulated ABL will be briefly explored. Finally, the chapter will end with a more detailed analysis of the streamwise measurement plane, which is under the influence of the simulated ABL.

3.1 Surface Oil Flow Visualization

The surface oil flow visualization results will be discussed in the current section. First, it is necessary to establish a primary understanding of different surface flow features present as a consequence of the Simple Frigate Shape No. 2 (SFS2) airwake. As mentioned in Section 2.3, the TiO_2 particles leave white traces on the matte black surface of the ship model. The following figures highlight some important topological flow features for the different quartering wind conditions. However, not all of the flow features found are shown in these figures. The airwake is complex and has many intricacies, and the oil flow visualization is only a qualitative interpretation of the off-surface flow topology.

The funnel wake region for the headwind case is shown in Fig. 3.1. The overall shape appeared symmetric, and three different points highlight some of the flow characteristics. First, the funnel itself is a bluff body with its own small recirculation region, as shown by Point A. Sharp edges of the funnel caused flow separation on the sides, which were observed as regions devoid of oil at the front and the back of the funnel. This funnel wake region,

shown by Point B, was unsteady and turbulent. Third, the funnel wake interacted with the larger recirculation bubble at the hangar doors, which caused the wake to curl around at the edge of the superstructure. Lastly, the areas on top of the superstructure highlighted by Point C were related to the horseshoe vortices, which wrapped around the front of the funnel. These horseshoe vortices created a clear boundary in the oil flow contours, distinguishing them from the funnel wake.

A difference was observed between the headwind and quartering wind cases. Figure 3.2 shows the same funnel wake region for the two yaw angles. Notice that the flows were distinctly different from the headwind case. The two quartering wind cases shared similar features yet were also different from one another. Although Point E resembled the horseshoe vortex shape, this region was the so-called "wing vortex" that formed at the front edge of

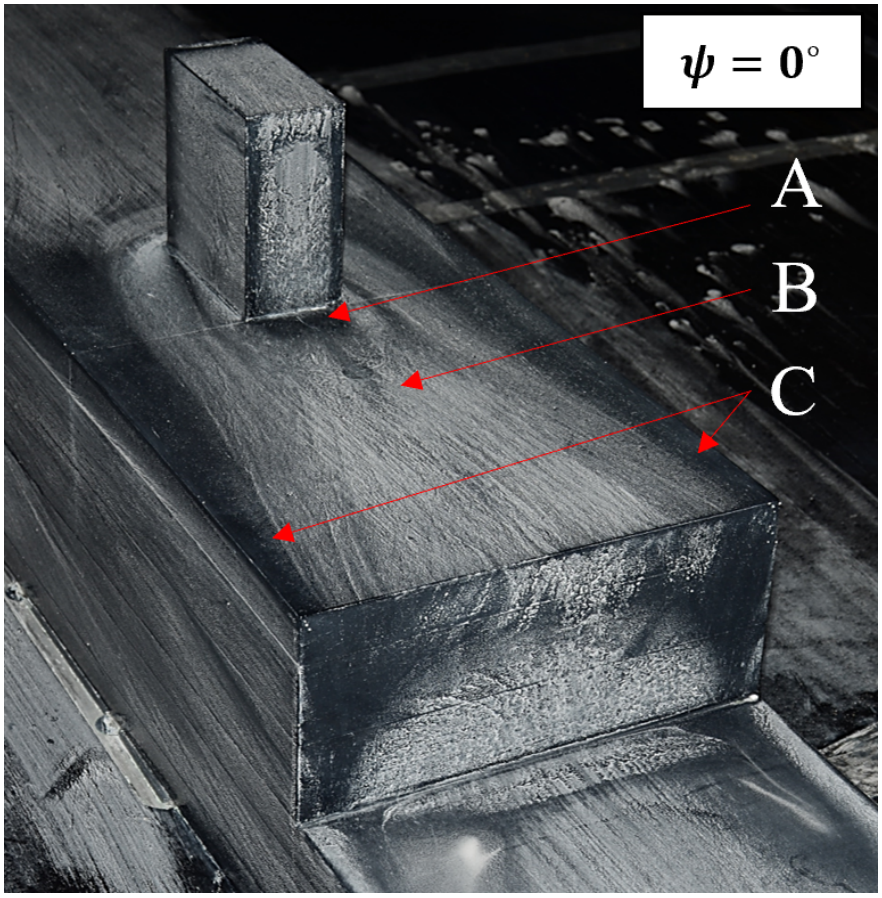

Figure 3.1 Surface oil flow visualization of the funnel wake region for $\psi = 0°$.

the superstructure and convected in the streamwise direction. Both yawed cases exhibited this latter phenomenon, the distinction was more apparent in Fig. 3.2b. Tinney and Ukeiley [5] observed such wing vortices on a model without a funnel, and Fig. 1.7 also captured a similar vortex structure on the port side.

Point F shows the wake of the funnel, which was once again turbulent and unsteady. In the $\psi = 20°$ case (Fig. 3.2b), the funnel wake shown by Point F was more narrow when compared to the $\psi = 10°$ case. As the yaw angle increased, the funnel wake further shifted towards the leeward side. It can be interpreted that a region of lower pressure formed in the area shown by Point D. When the ship model was yawed, the funnel had a region with higher pressure on the windward side, and a region with lower pressure on the leeward side. Additionally, in Fig. 3.2b, Point G shows the upwash from the leeward side, which is better visible in Fig. 3.4b noted by Point P. The flow in both yawed cases had an upwash on the

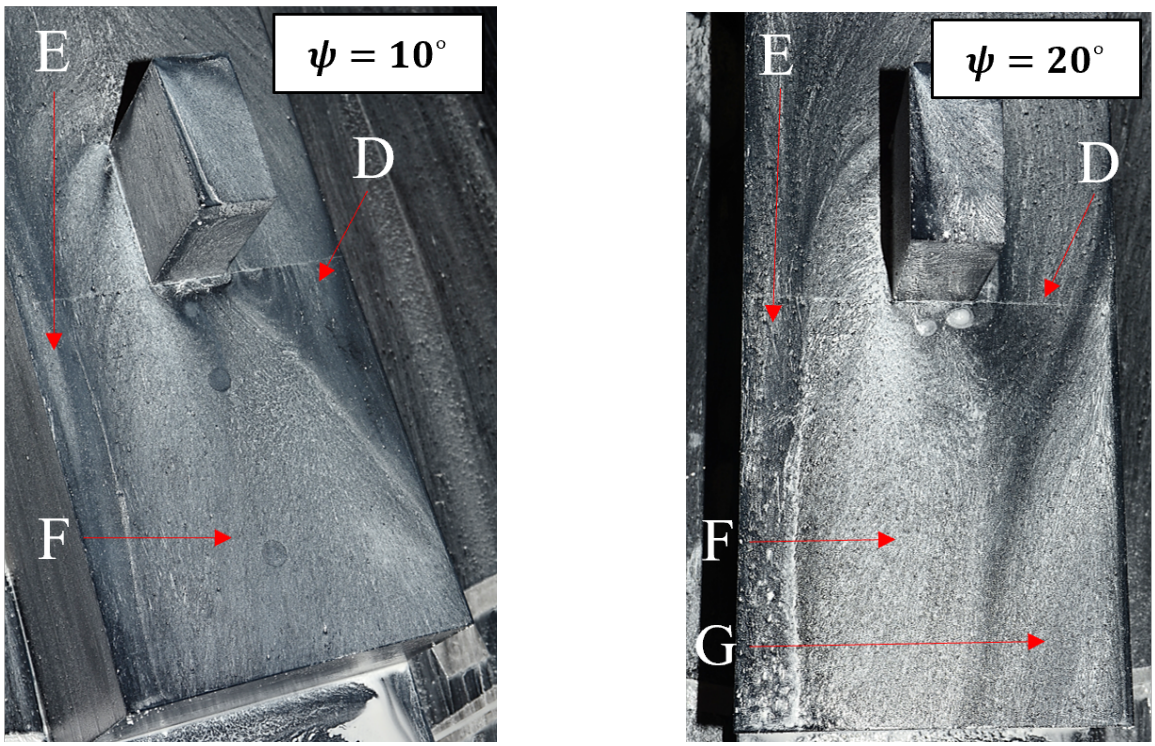

(a) Funnel wake region for $\psi = 10°$. *(b)* Funnel wake region for $\psi = 20°$.

Figure 3.2 Oil flow visualization showing differences within the funnel wake region for two different quartering wind conditions.

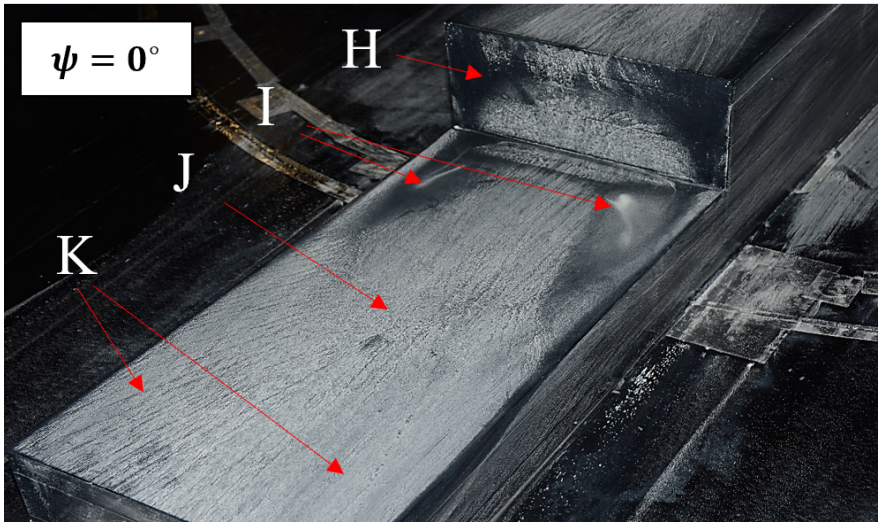

Figure 3.3 Surface oil flow visualization of the flight deck region for $\psi = 0°$.

leeward side. However, it was more prominent in the $\psi = 20°$ case.

The flight deck region for the headwind case is shown in Fig. 3.3. The most evident observation was the symmetry of the recirculation region. This recirculation region contained a horseshoe vortex with two foci in the locations shown by Point I. It can be seen that oil pooling occurred at these foci locations. Point H shows the separation line on the hangar doors. The flow coming from above the superstructure curled down onto the hangar doors and interacted with the recirculation region. The horseshoe vortex of the recirculation region caused a flow separation line to form in the shape of a "U." Some of the flow coming from above the superstructure was diverted downwards, and reattached at Point J, as shown in Fig. 3.3. The recirculation region was defined by the reattachment line, where the flow inside it moved upstream and the flow outside this region moved downstream. Point K highlights a spanwise movement of the flow observed after the reattachment line. This spanwise movement was likely a bi-product of the recirculation region, which affected a significant portion of the flight deck region.

Surface oil flow visualization of the flight deck region for the yawed cases is shown in Fig. 3.4. The differences between the quartering wind and headwind cases might initially appear as minor, but the airwake is actually significantly different. The main difference was

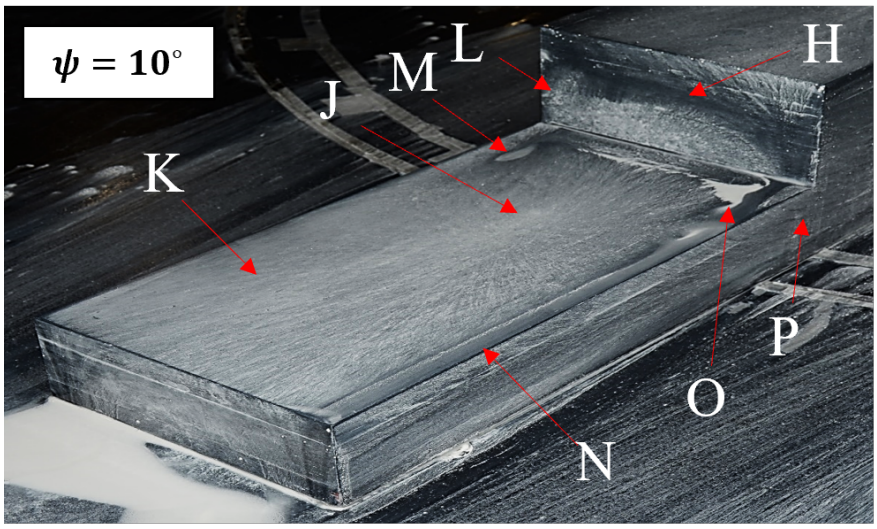

(a) Flight deck region for $\psi = 10°$.

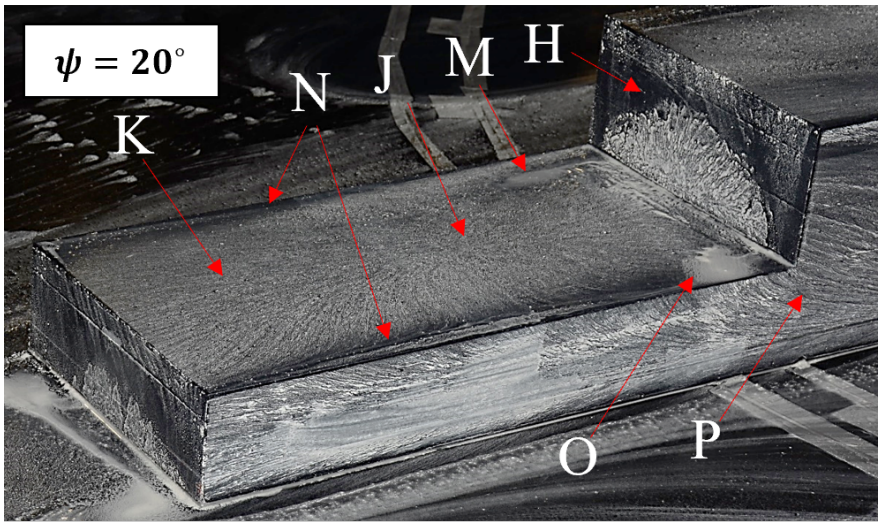

(b) Flight deck region for $\psi = 20°$.

Figure 3.4 Oil flow visualization showing the flight deck surface flow contours for different quartering wind conditions.

the asymmetry of the recirculation region and its size. The asymmetry was evident by the shape of the reattachment line, as well as the location of the reattachment point shown by Point J. Additionally, there was only one focus shown by Point M, which was located on the port side. On the starboard side, however, the significant pooling shown by Point O was caused by the interaction of the leeward side upwash (Point P) with the recirculation region.

There was a difference in the separation line (Point H) on the hangar doors between the

two quartering wind cases. The $\psi = 10°$ case did not show the same separation line. Instead, there was a strong upstream flow on the port side that resulted from the recirculation region interaction with the strong spanwise component of the windward side that curled onto the flight deck. This interaction caused the oil flow traces to remain on the port side edge of the hangar doors, which is shown by Point L in Fig. 3.4a. This effect was not present in the $\psi = 20°$ case, which was likely a result of the stronger flow separation on the port side edge. Similarly to the headwind case, the recirculation region affected the flow across the flight deck, which imposed spanwise movement of the near-wall flow downstream of the reattachment line, shown by Point K. Interestingly, on both edges of the flight deck, two angled separation lines were visible, indicated by Point N. The port side line was caused by the windward flow interaction with the flight deck edge, which led to flow separation. Conversely, the starboard side line was caused by the upwash from the leeward side, which attempted to curl onto the flight deck.

The surface flow visualization indicated a significant difference between the headwind and quartering wind cases. The oil flow results alone are not enough to classify certain flow features within the quartering wind airwake. Nevertheless, the results were insightful in providing near-wall flow features. Combined with the PIV results, which will be discussed next, a better overall understanding of the airwake that developed behind the yawed ship can be achieved.

3.2 Effects of Reynolds Number

The SFS2 airwake was not affected significantly by changes in the studied Reynolds number range of $Re \in [3.2, 6.4] \times 10^6$ based on the ship length. Prior work [11, 12] has shown that the headwind case did not have significant changes in the flow field for different Re variations. The ship model can be considered a bluff body, and such shapes are generally not sensitive to changes at high Re values. The dependence on Re was studied for the quartering wind cases. In this section, only crosswise Plane 1 and streamwise Plane 1 for $\psi = 10°$ will be covered.

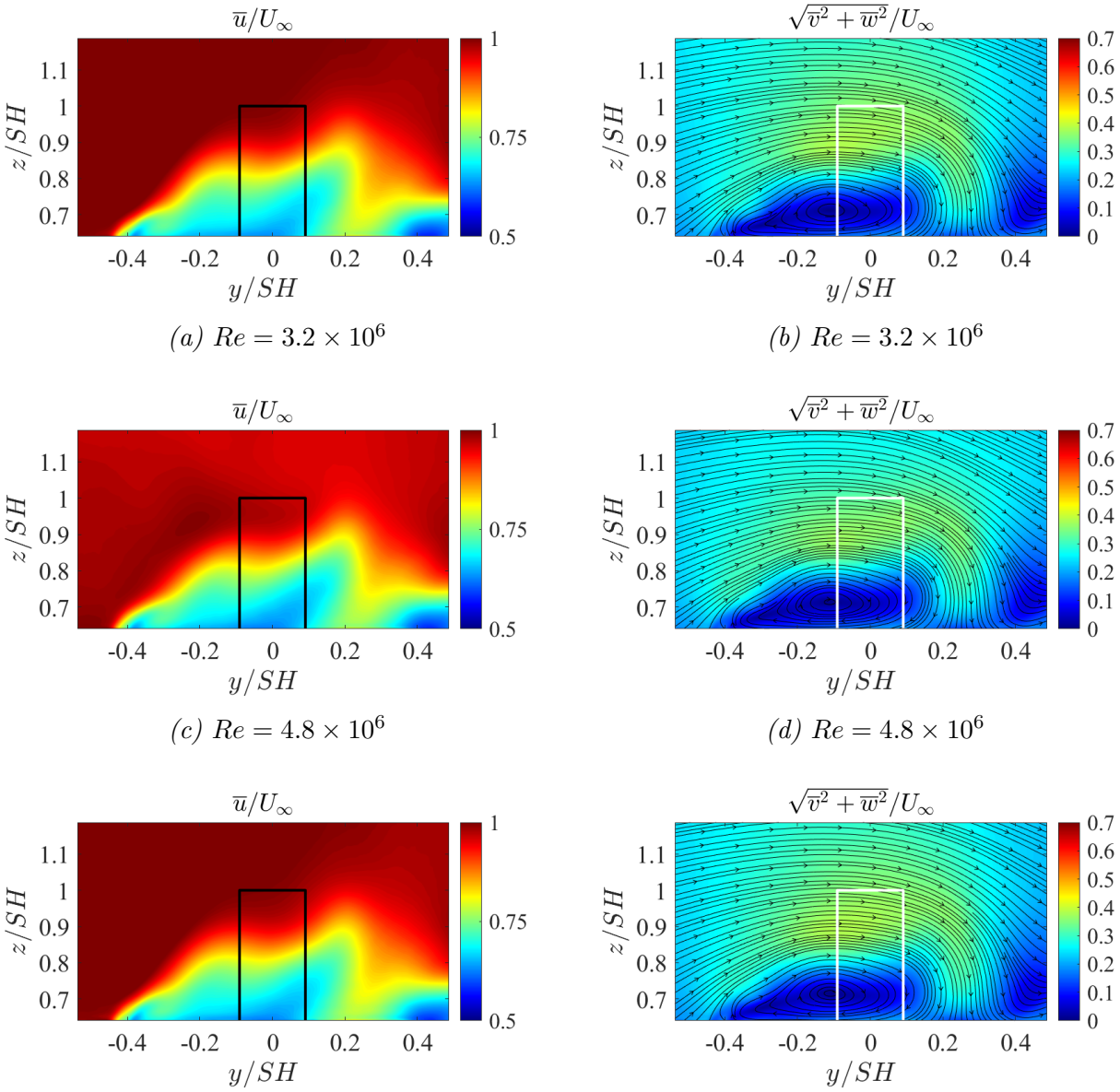

(a) $Re = 3.2 \times 10^6$ *(b)* $Re = 3.2 \times 10^6$

(c) $Re = 4.8 \times 10^6$ *(d)* $Re = 4.8 \times 10^6$

(e) $Re = 6.4 \times 10^6$ *(f)* $Re = 6.4 \times 10^6$

Figure 3.5 Reynolds number insensitivity shown through time-averaged velocity contours for crosswise Plane 1 (Figure 2.10a) for $\psi = 10°$. The contours do not include the simulated atmospheric boundary layer (ABL).

The flow field without the simulated ABL is shown in Fig. 3.5. The qualitative results showed minimal differences between the Re variations. Interestingly, the streamwise velocity $\overline{u}/U_\infty$ contour showed a lower free-stream region above the funnel for $Re = 4.8 \times 10^6$ (Fig. 3.5c). This difference was more evident in Fig. 3.6a, where a localized velocity profile at $z/SH = 0$

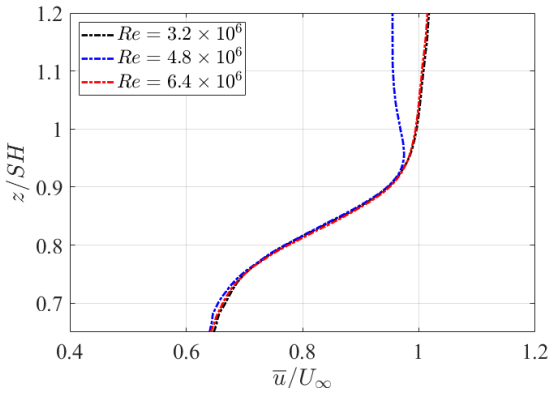

(a) Without the atmospheric boundary layer.

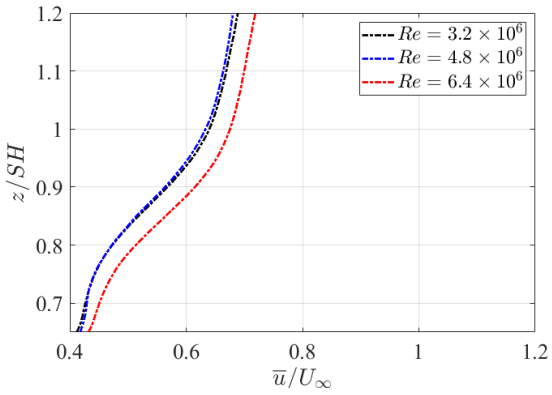

(b) With the atmospheric boundary layer.

Figure 3.6 Comparison of different Re effects on the time-averaged velocity for crosswise Plane 1 at $y/SH = 0$ and $\psi = 10°$. The location is the same as shown in Figure 2.11a.

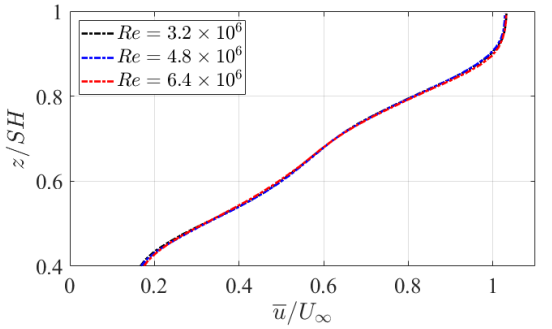

(a) Without the atmospheric boundary layer.

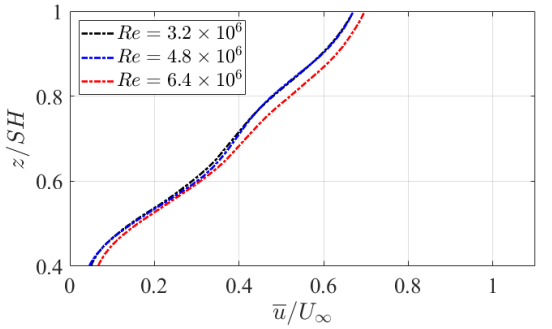

(b) With the atmospheric boundary layer.

Figure 3.7 Comparison of different Re effects on the time-averaged velocity for the streamwise Plane 1 at $x/SH = 1.5$ and $\psi = 10°$. The location is the same as shown in Figure I.3.

was plotted for three different Re cases. The velocity profile for the $Re = 4.8 \times 10^6$ case diverged from the other two variations before reaching $z/SH = 1$. Conversely, when the simulated ABL was included, the $Re = 4.8 \times 10^6$ case did not diverge, and it matched the general trend of the velocity profile seen in Fig. 3.6b. However, the simulated ABL caused the magnitude of $Re = 6.4 \times 10^6$ case to be higher, shifting the velocity profile. Likewise, the overall shape of the flow field (Fig. 3.8) was unaffected by the inclusion of the simulated ABL.

Although some deviations were observed in the time-averaged velocity profiles and contours, the velocity fluctuations were in good agreement, as shown in Fig. 3.9. This outcome suggests

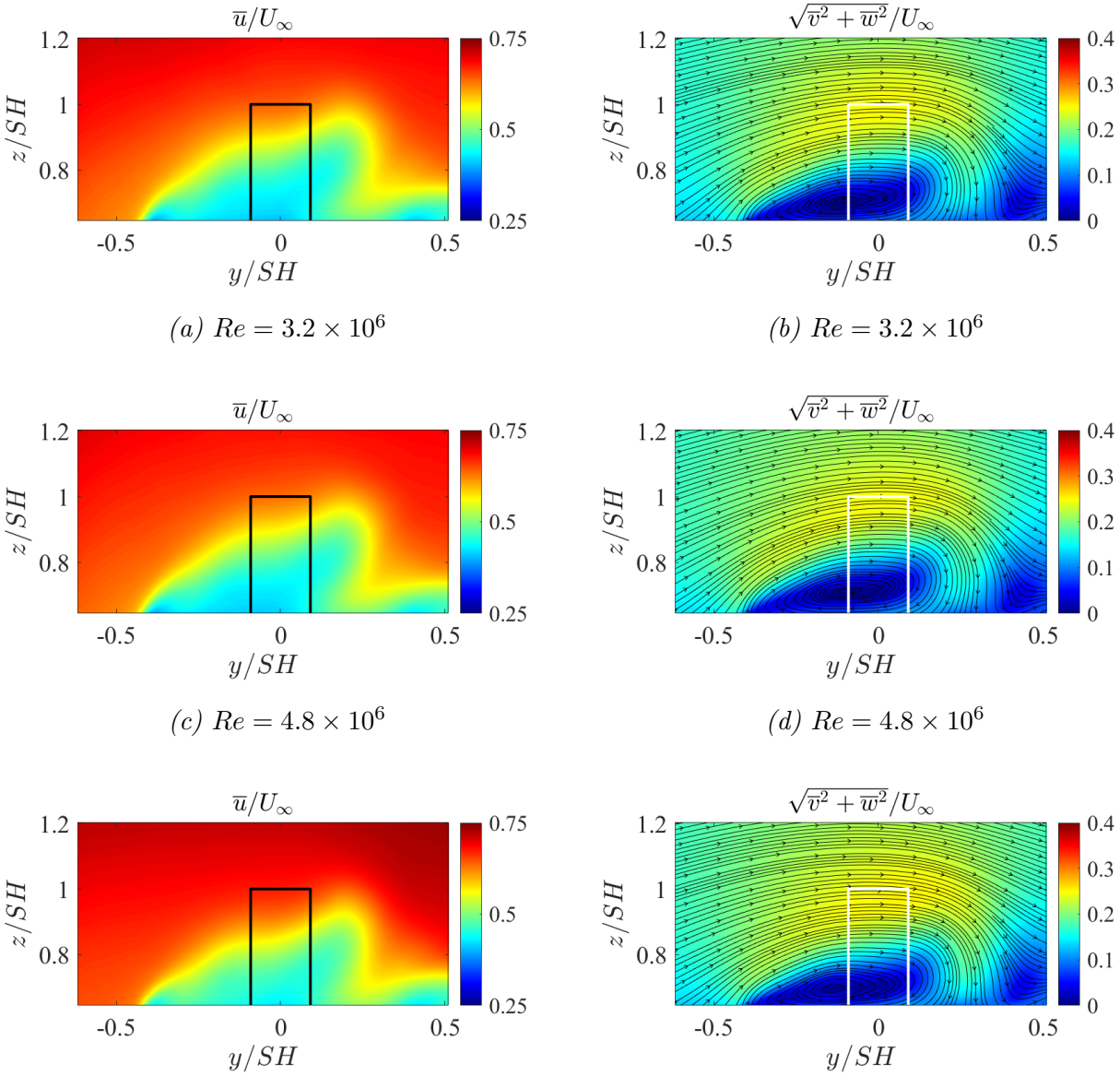

(a) $Re = 3.2 \times 10^6$ *(b)* $Re = 3.2 \times 10^6$

(c) $Re = 4.8 \times 10^6$ *(d)* $Re = 4.8 \times 10^6$

(e) $Re = 6.4 \times 10^6$ *(f)* $Re = 6.4 \times 10^6$

Figure 3.8 Reynolds number insensitivity shown through time-averaged velocity contours for crosswise Plane 1 (Figure 2.10a) for $\psi = 10°$. The contours include the simulated atmospheric boundary layer (ABL).

that the flow fields for quartering wind cases are indeed invariant of Re. If the deviations affected the flow field, it would have been evident within the fluctuations, which would suggest a change in the turbulent behavior. Considering the ABL did not cause the $Re = 4.8 \times 10^6$ case to diverge prematurely, the deviation in Fig. 3.6a was likely an anomaly. These findings

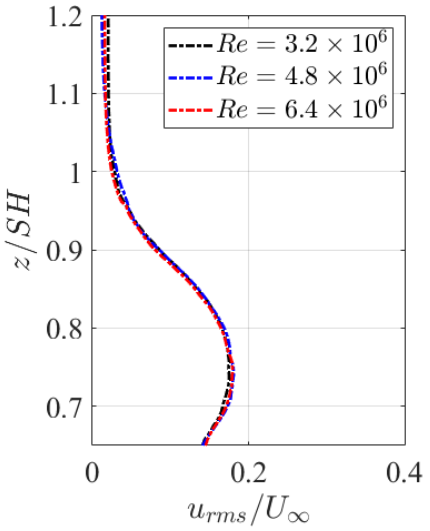

(a) Without the atmospheric boundary layer.

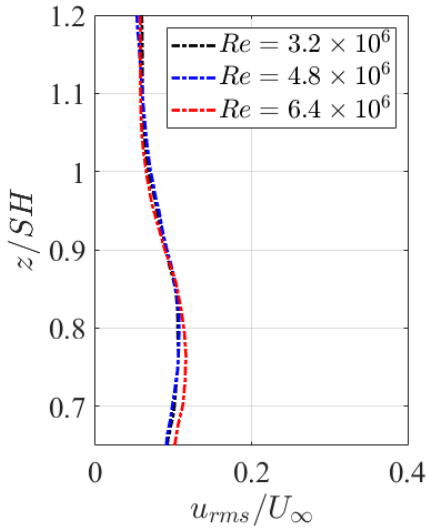

(b) With the atmospheric boundary layer.

Figure 3.9 Comparison of Re effects on the time-averaged velocity fluctuations for crosswise Plane 1 at $y/SH = 0$ and $\psi = 10°$. The location is the same as shown in Figure 2.11a.

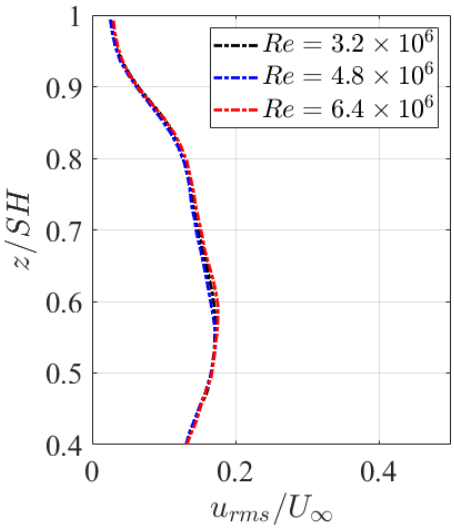

(a) Without the atmospheric boundary layer.

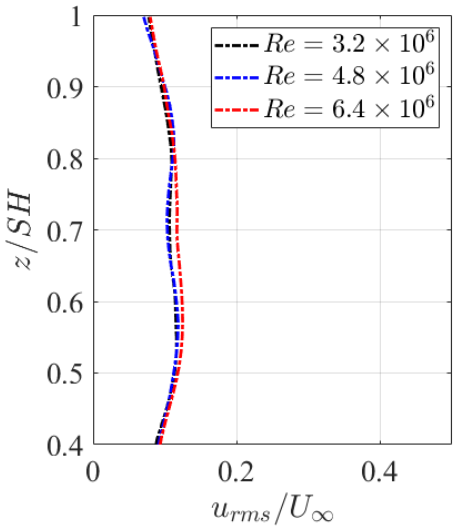

(b) With the atmospheric boundary layer.

Figure 3.10 Comparison of Re effects on the time-averaged velocity fluctuations for the streamwise Plane 1 at $x/SH = 1.5$ and $\psi = 10°$. The location is the same as shown in Figure I.3.

were consistent with the performed stereoscopic TR-PIV measurements. Thus, a single case is sufficient to highlight the Re independence.

Planar TR-PIV results did not contain deviations within the localized velocity profiles

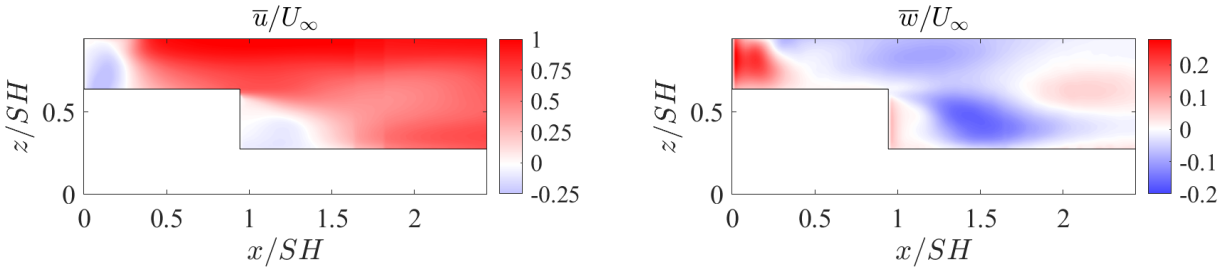

(a) $Re = 3.2 \times 10^6$ *(b)* $Re = 3.2 \times 10^6$

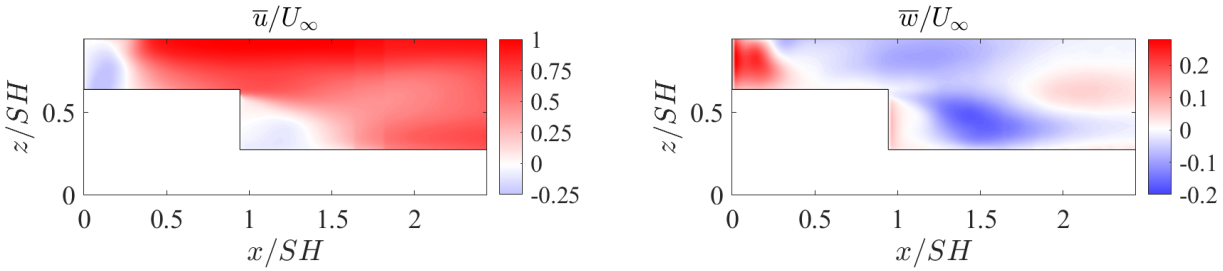

(c) $Re = 4.8 \times 10^6$ *(d)* $Re = 4.8 \times 10^6$

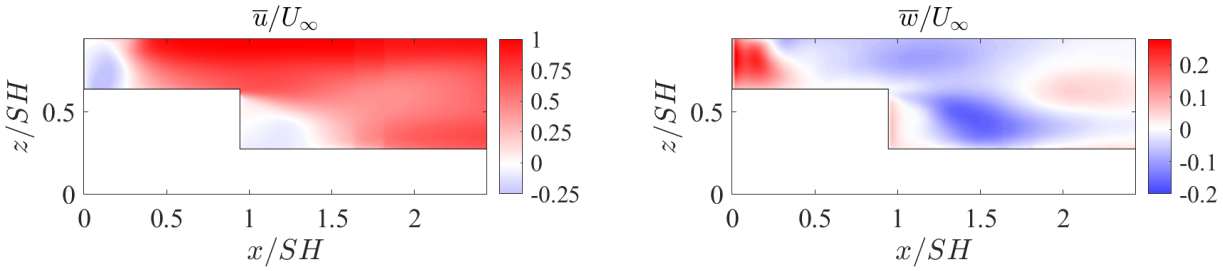

(e) $Re = 6.4 \times 10^6$ *(f)* $Re = 6.4 \times 10^6$

Figure 3.11 Reynolds number independence shown through time-averaged velocity component contours for the streamwise Plane 1 (Figure 2.10b) for $\psi = 10°$. The contours do not include the simulated atmospheric boundary layer (ABL).

for the streamwise Plane 1. The flow field remained unchanged with different Re variations, as seen in Fig. 3.11. The localized velocity profiles at $x/SH = 1.5$ in Fig. 3.7 also showed exceptional agreement. Once again, a slight shift was observed for the $Re = 6.4 \times 10^6$ case in Fig. 3.7b. This shift for the $Re = 6.4 \times 10^6$ cases might have been caused by a stronger velocity profile of the simulated ABL. Nevertheless, the difference was minor and the overall

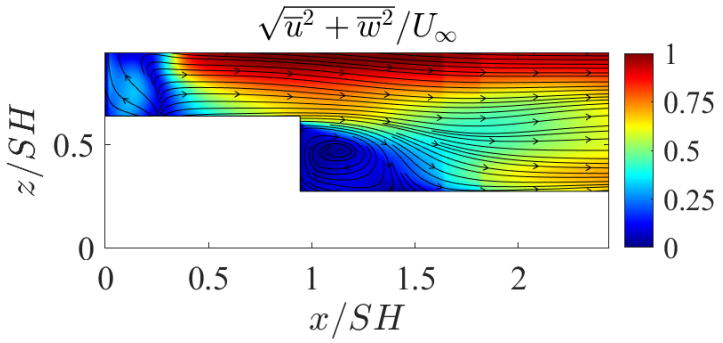

(a) $Re = 3.2 \times 10^6$

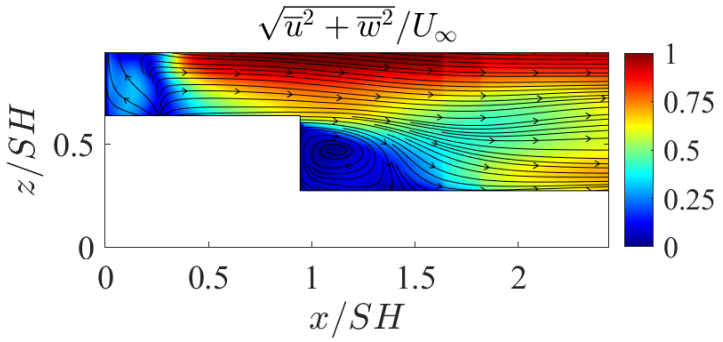

(b) $Re = 4.8 \times 10^6$

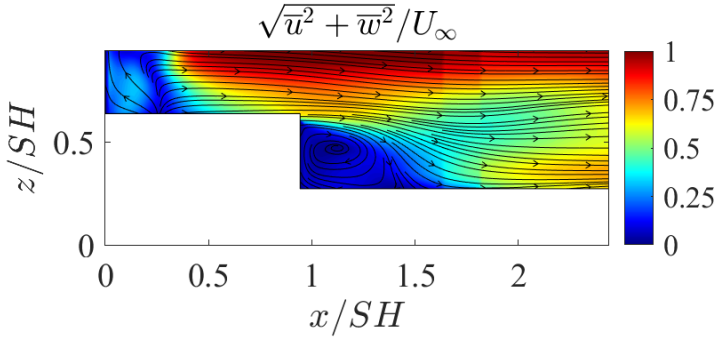

(c) $Re = 6.4 \times 10^6$

Figure 3.12 Reynolds number independence of the time-averaged velocity magnitude and direction for the streamwise Plane 1 (Figure 2.10b) for $\psi = 10°$. The contours do not include the simulated atmospheric boundary layer (ABL).

profile of the flow field remained consistent. The fluctuations for the streamwise case in Fig. 3.10 were consistent as well.

For the SFS2 geometry, an invariant flow field is expected at high Re values. It is important to confirm the invariance for different quartering wind conditions. Although only two planes of interest were presented in this section, the invariance was present for all measured planes (Fig. 2.10). Thus, it is valid to consider the flow field to be consistent. Increasing Reynolds number values do not significantly affect the flow field, even with different quartering wind conditions. Typically, the threshold value of Reynolds number independence for naval ships is around 10^4, and Lumsden showed the consistency of flow characteristics for ships with Re varying from 10^4–10^7 [17]. Therefore, the changes in Reynolds number are not as relevant to the ship airwake as the changes in quartering wind conditions and the effects of the ABL. Further sections will consider only the results obtained from the case of $Re = 3.2 \times 10^6$ based on the ship length.

3.3 Time-Averaged Ship Airwakes

A comprehensive summary of the time-averaged velocity, velocity fluctuations, and turbulent kinetic energy (TKE) contours obtained from TR-PIV measurements will be covered in the current section. The cases without the effects of ABL (Table 2.2) were considered and compared with the headwind case where possible. The results included only the 100 ft s^{-1} (30.48 m s^{-1}) case. As mentioned in the previous section, the flow field remained independent of the Reynolds number. Hence, a detailed analysis for more than one flow velocity is redundant. Instead, comparisons between the different quartering wind cases for all regions of interest (Fig. 2.10) were made. Qualitative velocity contours will be presented first for the crosswise planes, followed by the streamwise plane. Afterward, the time-averaged velocity fluctuations and TKE contours will be covered in a similar manner.

3.3.1 Airwake Flow Velocity Contours

The funnel wake was partially captured by the field of view of crosswise Plane 1, shown in Fig. 3.13. Differences between each quartering wind case were clearly evident. Symmetry was observed in the streamwise velocity $\overline{u}$ for $\psi = 0°$. The funnel wake was significant enough to reduce the magnitude of the incoming streamwise flow. Although in the headwind case,

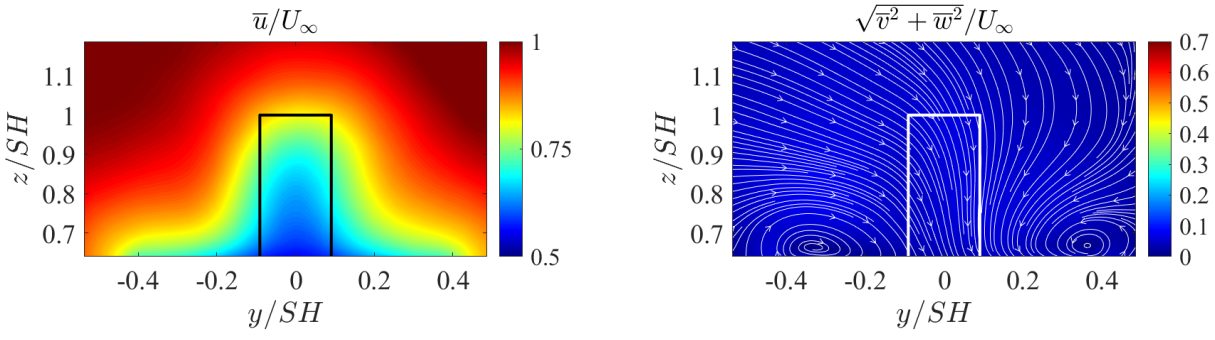

(a) $\psi = 0°$.

(b) $\psi = 0°$.

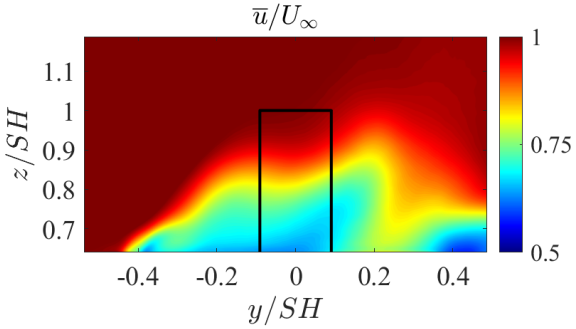

(c) $\psi = 10°$.

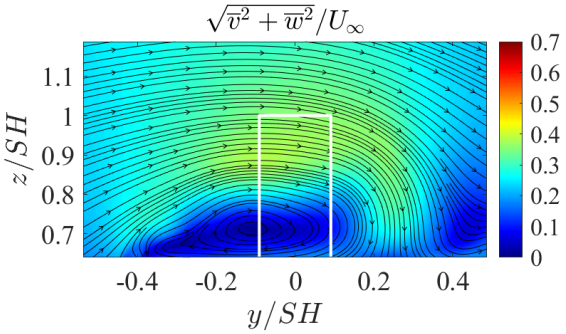

(d) $\psi = 10°$.

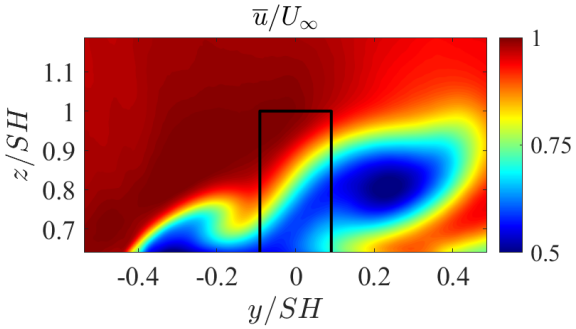

(e) $\psi = 20°$.

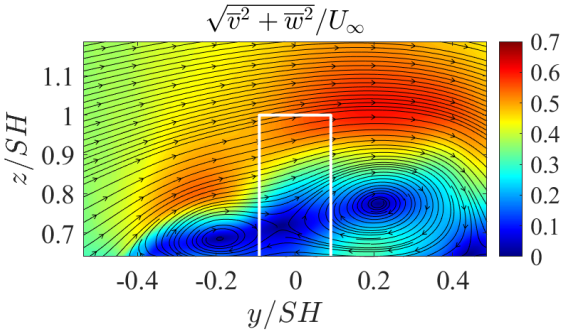

(f) $\psi = 20°$.

Figure 3.13 Time-averaged velocity contours for crosswise Plane 1 (Figure 2.10a) for $U_\infty = 30.48$ m s^{-1}.

the body-axis reference frame matched the free-stream reference, for the sake of clarity, the terms "streamwise," "spanwise," and "wall-normal" will also be used in conjunction with the body-axis reference frame for quartering wind cases (Fig. 2.10).

Figure 3.13 shows the spanwise and wall-normal components combined into a contour of $\sqrt{\overline{v}^2 + \overline{w}^2}/U_\infty$, with the lines indicating the dominant direction of the cross-sectional flow

field. It is worth noting that these lines do not represent the streamlines of the flow field per se, and they are only a general indicator of the flow direction, as used in prior works [2, 4–7, 9].

With that being said, the symmetric wake of the headwind case had its lowest values at $0.5U_\infty$ in the streamwise direction. At this location, no upstream flow was present, suggesting that the recirculation region of the funnel was further upstream. However, the effect of the funnel recirculation region remained relevant, causing a reduction of the streamwise flow velocity. The cross-sectional flow field showed significantly weaker magnitudes, with the highest regions reaching around $0.1U_\infty$. These results suggested the existence of the counter-rotating horseshoe vortices that had previously indicated their presence in the oil flow results (Fig. 3.1).

The time-averaged flow field of the quartering wind cases differed significantly. An asymmetric funnel wake was observed, as shown in Fig. 3.13c & 3.13e. The asymmetry appeared to become more significant as the yaw angle was increased. In the $\psi = 10°$ case, the streamwise velocity was higher throughout the funnel wake. However, a region of reduced velocity remained present. This reduced velocity region appeared to contain a vortical structure in the vicinity of the wall, shown by the cross-sectional flow field contours. This vortical structure was likely related to the propagating trailed vortex (Point E in Fig. 3.2), which interacted with the immediate funnel airwake. This interaction, combined with the windward flow separating at the edge of the superstructure, caused the trailed vortex to shift towards $y/SH = -0.1$ instead of remaining near the edge of the superstructure at $y/SH = -0.41$. Additionally, this vortical structure had a distinctly lower magnitude than the surrounding flow field, which reached speeds of $0.4U_\infty$.

As for the other quartering wind case of $\psi = 20°$, the flow appeared to develop differently from the $\psi = 10°$ case. There was a strong reduced streamwise flow region towards the starboard side, as shown in Fig. 3.13e. The funnel wake shifted further to the leeward side, causing a secondary vortical structure to form around $y/SH = 0.2$. The center of this

secondary structure appeared to follow the reduced pressure region, shown by Point D in Fig. 3.2b. The reduced pressure region indicated that the flow moved faster near the surface of the superstructure, which was observed by the higher near-wall streamwise velocity in Fig. 3.13e at $y/SH = 0.2$. The shift of the funnel wake towards the leeward side also caused the port-side trailed vortex to move closer towards the superstructure edge. This vortex movement was from $y/SH = -0.1$ to $y/SH = -0.2$. Although the shift was significant, the trailed vortex appeared to remain under the influence of the funnel wake. Lastly, the overall cross-sectional flow field appeared to have even greater magnitudes, reaching upwards of $0.6U_\infty$. It is also worth noting that both quartering wind cases had sharp velocity gradients in streamwise and cross-sectional flow fields, unlike the more gradual change in the headwind case.

One of the most prominent features of the SFS2 airwake and other backward-facing step geometries is the recirculation region. This region consists of complex crosswise flow interactions and areas where the flow moves upstream instead of downstream. This latter flow behavior was captured by the measurements in crosswise Plane 2, as shown in Fig. 2.10a, which was located at $l/4$ of the flight deck length.

By inspecting the results for the headwind case in Fig. 3.14a, a similar observation to the one made for crosswise Plane 1 was apparent—the flow was symmetric. The streamwise flow contour had an upstream flow region, indicated by the light blue color, which reached velocities of $-0.25U_\infty$. The headwind case had a sharp streamwise flow gradient near the edges of the flight deck, where the flow rapidly changed from the free-stream to the upstream flow of the recirculation region.

The cross-sectional flow did not show significant velocity gradients, unlike the gradients seen for the streamwise flow. However, at the edges of the ship geometry, the cross-sectional velocity had a higher magnitude than observed in crosswise Plane 1, reaching $0.15U_\infty$. The flow was directed downward from the hangar door upper edge and curled inward towards the flight deck from both port and starboard sides, indicated by the lines of the cross-sectional

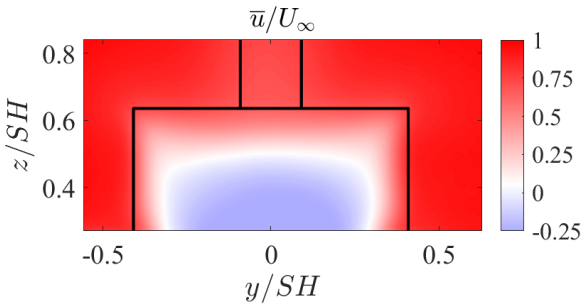

(a) $\psi = 0°$.

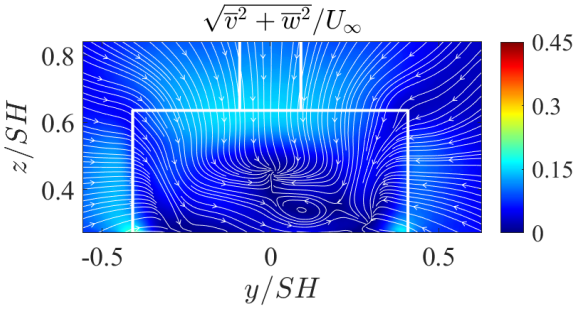

(b) $\psi = 0°$.

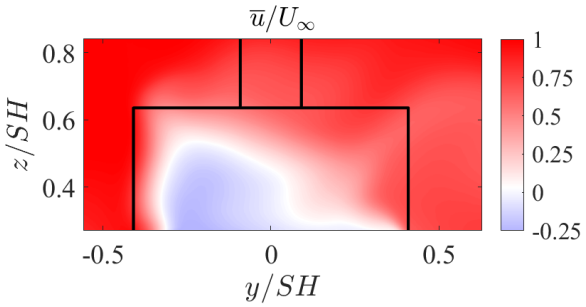

(c) $\psi = 10°$.

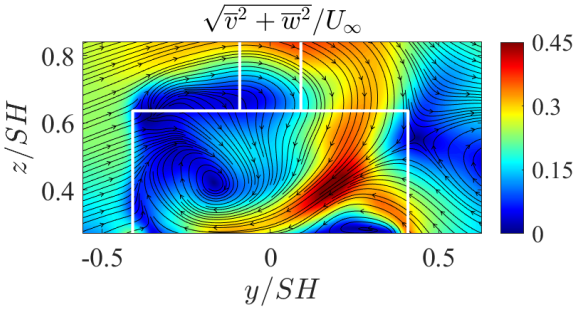

(d) $\psi = 10°$.

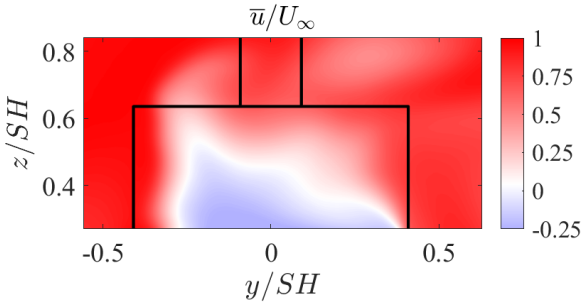

(e) $\psi = 20°$.

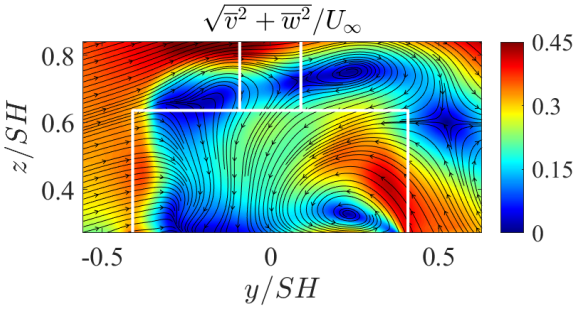

(f) $\psi = 20°$.

Figure 3.14 Time-averaged velocity contours for crosswise Plane 2 (Figure 2.10a) for $U_\infty = 30.48$ m s^{-1}.

velocity contour in Fig. 3.14b.

The recirculation region involved many complex flow interactions for the quartering wind cases. First, the recirculation region was asymmetric, as seen in Fig. 3.14c & 3.14e, with a bias towards the port side. The oil flow visualization indicated a focus on the port side, shown by Point M in Fig. 3.4. Therefore, it appears that the asymmetry of the recirculation region

tended to be more biased towards the windward side. The highest magnitude of the upstream flow within the recirculation region was also $-0.25U_\infty$. However, the overall cross-sectional size appeared to be smaller.

The oil flow visualization also indicated signs of the recirculation region becoming smaller. A difference between the $\psi = 10°$ and $\psi = 20°$ cases in the streamwise contours appeared above the superstructure region. The $\psi = 20°$ case (Fig. 3.13e) had patches of reduced streamwise flow in the rough vicinity of the previously observed trailed and secondary vortices in crosswise Plane 1. These reduced areas were also present in the cross-sectional velocity magnitude for $\psi = 20°$. The vortical structures from crosswise Plane 1 appeared to be present in crosswise Plane 2 for $\psi = 20°$, whereas the horseshoe vortices dissipated for the headwind case. The $\psi = 10°$ seemed to have a remnant of the crosswise Plane 1 vortex. However, it was not as distinct as the two vortices seen in the $\psi = 20°$ case.

There were many differences in the cross-sectional flow field between the two quartering wind cases in crosswise Plane 2. The $\psi = 10°$ case (Fig. 3.14d) had a greater area of low cross-sectional velocity on the port side. Considering the slightly wider upstream flow region for $\psi = 10°$, it was likely that the interaction between the trailed vortex and the recirculation region caused a sharp gradient at the port side edge. This sharp gradient and area of reduced velocity possibly caused the oil flow to remain on the hangar doors at Point L in Fig. 3.4a.

Another difference involved the interaction of the recirculation region and the leeward side upwash. A strong cross-sectional velocity magnitude of $0.5U_\infty$ was present for the $\psi = 10°$ case on the flight deck. The recirculation region directed the incoming flow from the funnel wake downwards, which then interacted with the upwash and formed a region where the flow reached higher magnitudes, as seen in Fig. 3.14d.

This same effect was also present in $\psi = 20°$, however, it was closer towards the starboard side edge (Fig. 3.14f). The $\psi = 20°$ case had a strong upwash, which was also seen in the oil flow visualization, indicated by Point P in Fig. 3.4b. Figure 3.14f shows the upwash that appeared in the form of high cross-sectional magnitude on the leeward side flight deck

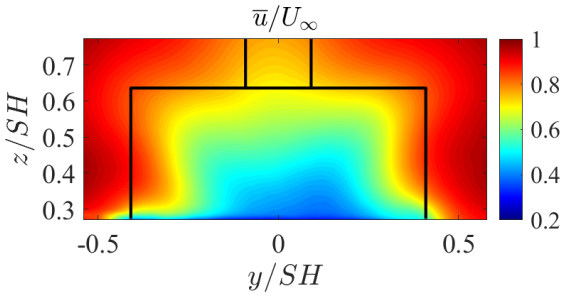

(a) $\psi = 0°$.

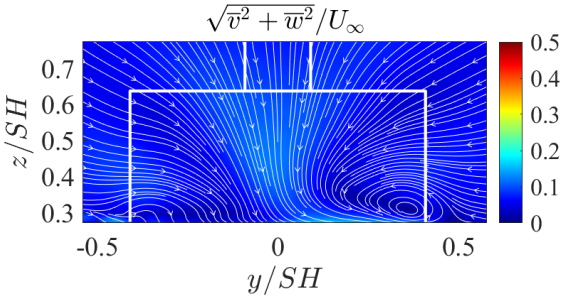

(b) $\psi = 0°$.

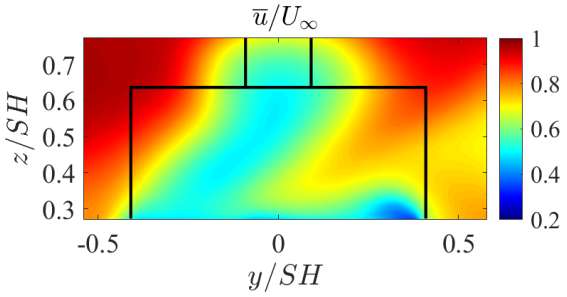

(c) $\psi = 10°$.

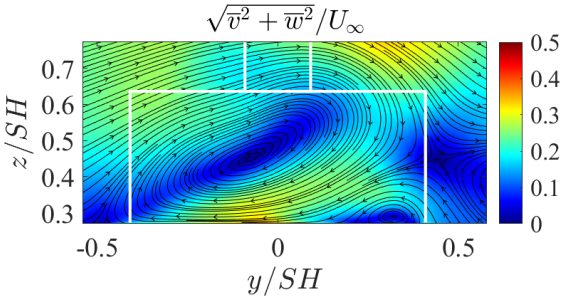

(d) $\psi = 10°$.

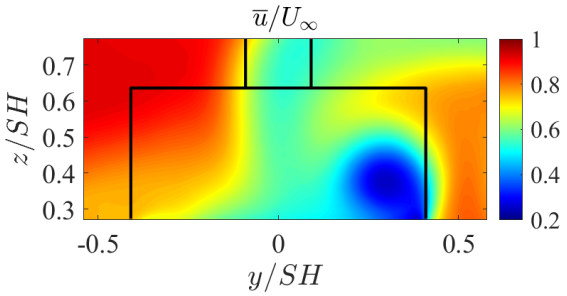

(e) $\psi = 20°$.

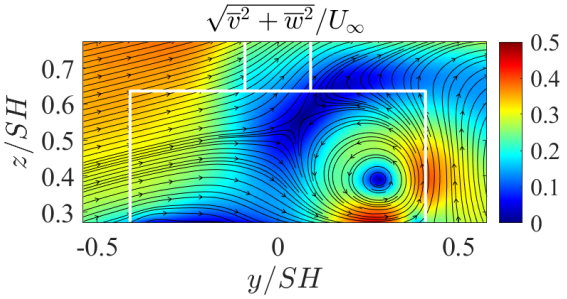

(f) $\psi = 20°$.

Figure 3.15 Time-averaged velocity contours for crosswise Plane 3 (Figure 2.10a) for $U_\infty = 30.48$ m s^{-1}.

edge at $y/SH = 0.4$. The interaction seemed to form a small flight deck vortex in the same region. These complex interactions were present across the entire field of view (FOV) for the quartering wind cases, highlighting the distinct difference between them and the headwind case.

Further downstream of the recirculation region, the final examined crosswise plane was

located. This final crosswise Plane 3 (Fig. 2.10a) intersected two flight deck vortices in the headwind case, seen by the lines of the cross-sectional velocity magnitude in Fig. 3.15b. The headwind case remained symmetric, as it was for the previous two crosswise planes. No sharp velocity gradients were present for the headwind case. However, there was a reduced streamwise flow region, similar to the one observed in crosswise Plane 1 for the funnel wake (Fig. 3.13a). The quartering wind cases shared the least resemblance in this region of interest. Conversely, for the $\psi = 10°$ case in Fig. 3.15d, a large vortical structure that spanned across the entire flight deck appeared to form. The region expanded above the superstructure as well. On the other hand, the $\psi = 20°$ case in Fig. 3.15f seemed to have a flight deck vortex at the edge of the starboard side flight deck that caused the windward flow to diverge. This diversion created a sharp gradient for both streamwise and cross-sectional velocities on the leeward side. Lastly, the overall shifting of the airwake was apparent at this crosswise plane. For both quartering wind cases, the reduced velocity regions expanded above the superstructure. For the $\psi = 20°$ case specifically, the shift of the funnel wake was also captured in Fig. 3.15e. Thus, these crosswise flow contours, combined with oil flow visualization, revealed essential qualitative information about the different flow structures within the SFS2 airwake.

The flow features observed from the crosswise planes can lack a clear connection between them. Hence, it is helpful to investigate the streamwise evolution of the flow field. A single streamwise plane shown in Fig. 2.10b was measured for both quartering wind cases. A comparative streamwise case without the effects of ABL was unavailable. Hence only the two quartering wind cases were compared. Figure 3.16 shows the velocity contours of both components, as well as their magnitude $\sqrt{\overline{u}^2 + \overline{w}^2}$, with lines indicating the direction of the dominant component. The streamwise plane revealed additional features that were not fully captured by the crosswise planes. First, the recirculation region of the funnel was visible for both quartering wind cases, which is indicated by the light blue color in the $\overline{u}/U_\infty$ contours. It appeared that the $\psi = 10°$ case had a larger funnel recirculation region, suggesting the wake of the funnel was also larger within the body-axis reference frame. Conversely, the

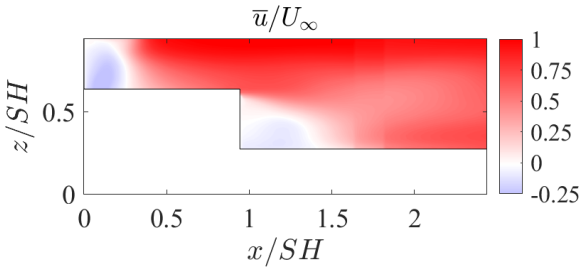

(a) $\psi = 10°$.

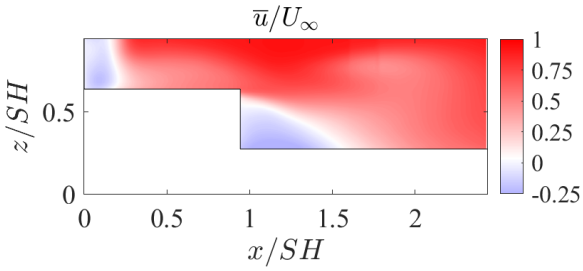

(b) $\psi = 20°$.

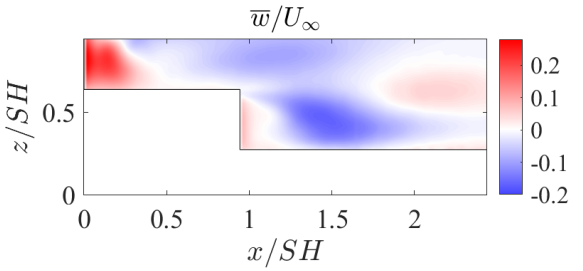

(c) $\psi = 10°$.

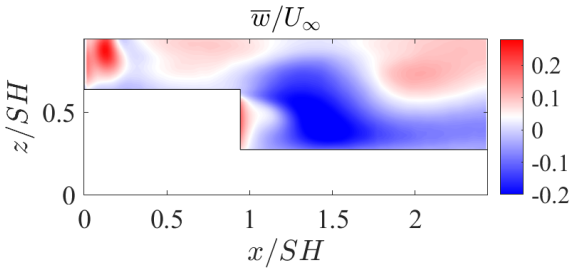

(d) $\psi = 20°$.

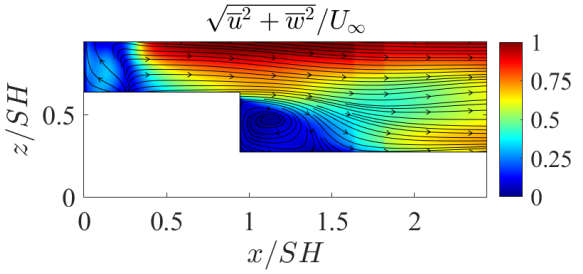

(e) $\psi = 10°$.

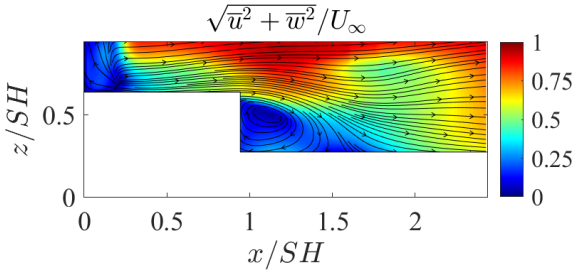

(f) $\psi = 20°$.

Figure 3.16 Time-averaged velocity contours for streamwise Plane 1 (Figure 2.10b) for $U_\infty = 30.48$ m s^{-1}.

$\psi = 20°$ case had a smaller funnel recirculation region, which was perhaps because of the funnel wake being shifted outside the body-axis reference frame. An interesting observation can also be made for the wall-normal velocity component in the funnel wake. The area of positive wall-normal velocity was substantially greater behind the funnel than in the flight deck recirculation region.

The streamwise contours revealed some of the features found in crosswise planes. The

flight deck area had a distinct region of lower streamwise velocity, as shown in Fig. 3.16. For the $\psi = 10°$ case, crosswise Plane 3 (Fig. 3.15d) revealed a large vortical structure across the entire cross-sectional area of the flight deck. This vortical structure spanned above the superstructure and had reduced streamwise velocities, which were also observed from the measurements shown in Fig. 3.16a. Likewise, the $\psi = 20°$ case also showed the deflection of the windward flow, which was affected by the flight deck vortex at crosswise Plane 3, as seen in Fig. 3.15f. Although the centerline streamwise plane covered only the symmetry line, it supplemented the observations for crosswise planes. Therefore, the combination of crosswise and streamwise plane measurements revealed some flow features that were not present in the surface oil flow visualization. These qualitative results helped distinguish certain features that might be common for the SFS2 airwake with different quartering wind conditions.

3.3.2 Airwake Fluctuation Contours

Time-averaged velocity contours for quartering wind cases revealed flow features that were different from the headwind case. One quantitative measure of the airwake can be done by examining the velocity fluctuations and TKE. Velocity fluctuations and TKE provided insight into the turbulent behavior of the airwake. Similarly to the previous subsection, each crosswise plane will be covered in order, with the streamwise Plane 1 being last. The velocity fluctuations for crosswise Plane 1 are shown in Fig. 3.17 & 3.18. Once again, the fluctuations were symmetric for the headwind case and more widespread across the FOV. Although the fluctuations were widespread, they remained minimal in magnitude. On the other hand, the quartering wind cases had strong fluctuations for all three velocity components in Fig. 3.17 & 3.18. These high fluctuations seemed to occur in areas of the observed flow features. For $\psi = 10°$, the highest fluctuations were within the vortical structure. Similarly, the $\psi = 20°$ case appeared more turbulent in the areas covered by the two observed vortical flow features. Outside these regions, the fluctuations for quartering wind cases were essentially zero.

The TKE for crosswise Plane 1 is shown in Fig. 3.18. A resemblance to the spanwise

velocity fluctuation, v_{rms}, was clear. The funnel airwake appeared to be energetic in the vortical structure region. A strong spanwise component for the quartering wind cases seemed to affect the turbulent behavior significantly, whereas the headwind case did not produce as much turbulent kinetic energy. The $\psi = 10°$ had a more concentrated energy distribution compared to the $\psi = 20°$ case.

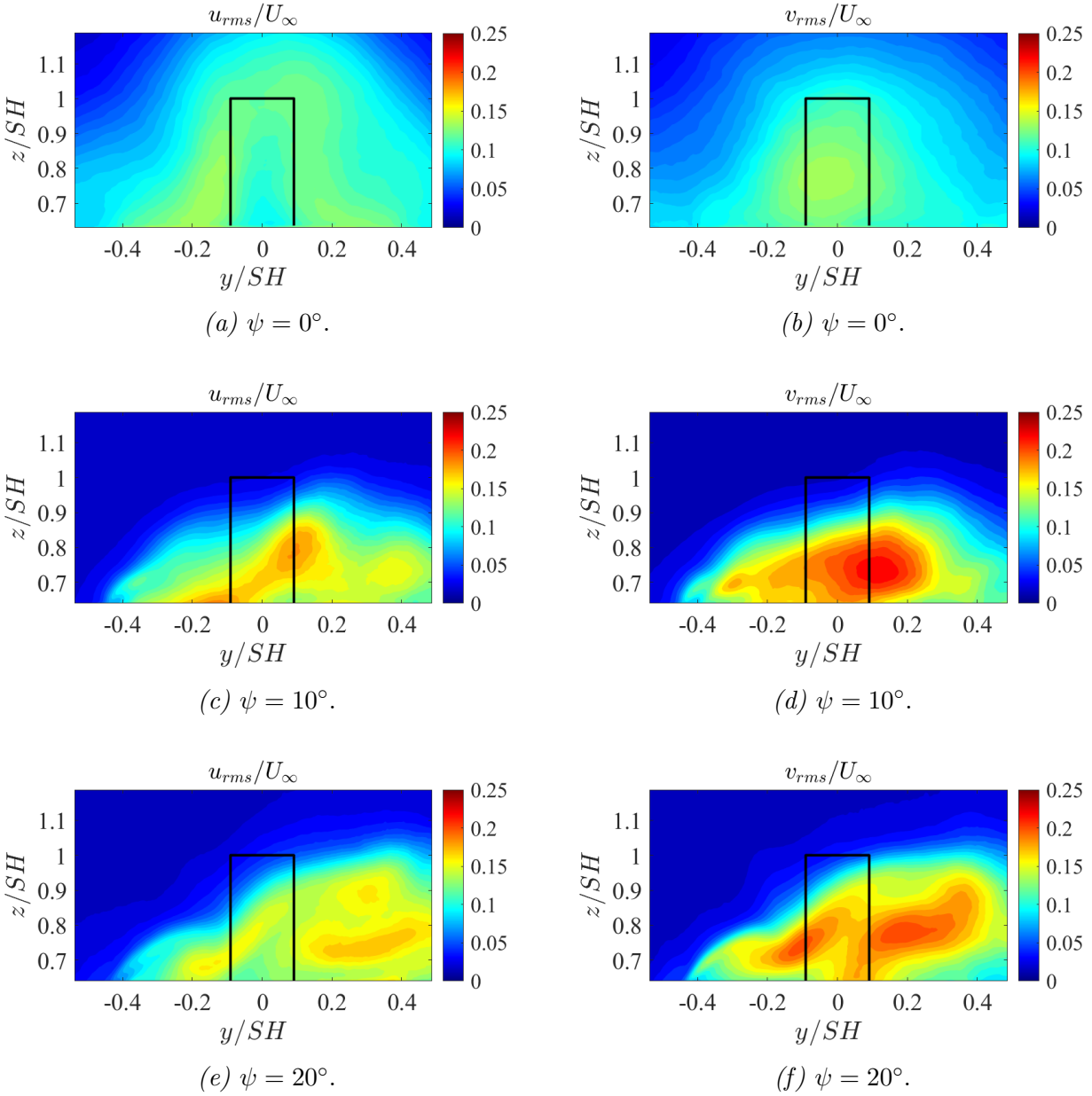

(a) $\psi = 0°$. *(b)* $\psi = 0°$.

(c) $\psi = 10°$. *(d)* $\psi = 10°$.

(e) $\psi = 20°$. *(f)* $\psi = 20°$.

Figure 3.17 Time-averaged streamwise & spanwise velocity fluctuation contours for crosswise Plane 1 (Figure 2.10a) for $U_\infty = 30.48$ m s^{-1}.

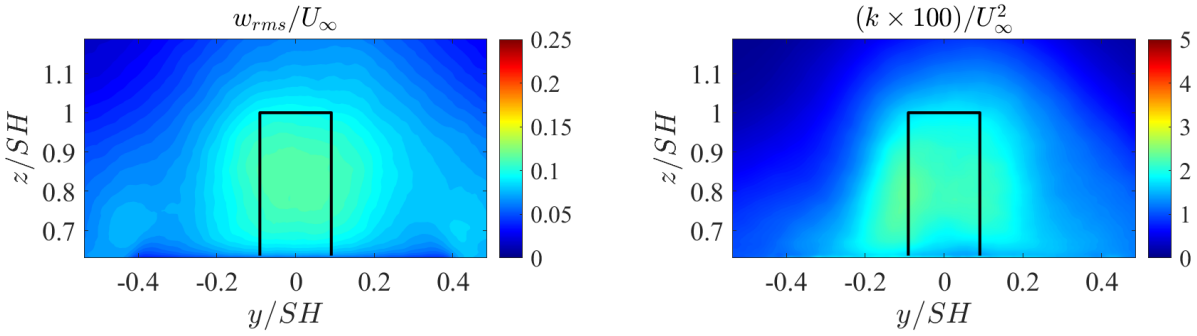

(a) $\psi = 0°$.

(b) $\psi = 0°$.

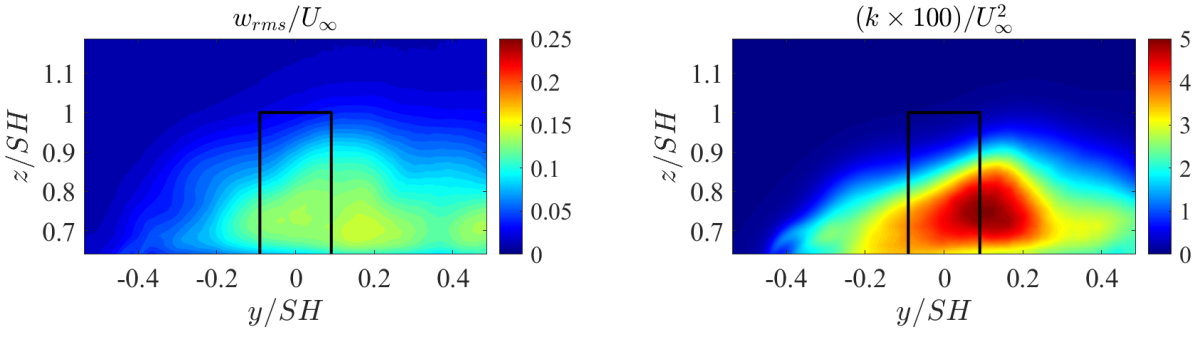

(c) $\psi = 10°$.

(d) $\psi = 10°$.

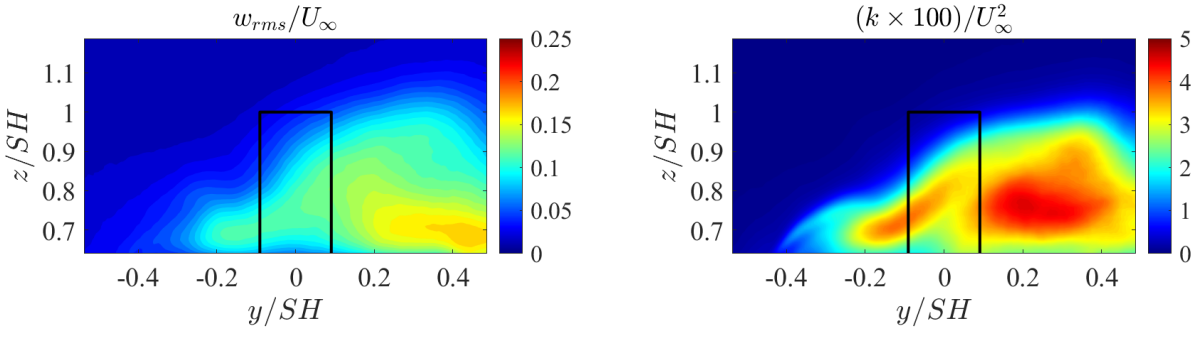

(e) $\psi = 20°$.

(f) $\psi = 20°$.

Figure 3.18 Time-averaged wall-normal velocity fluctuation & TKE contours for crosswise Plane 1 (Figure 2.10a) for $U_\infty = 30.48$ m s^{-1}.

Fluctuations of crosswise Plane 2 are shown in Fig. 3.19 & 3.20. The recirculation region had more turbulent behavior compared to crosswise Plane 1. Widespread fluctuations were once again present for the headwind case. However, the streamwise fluctuation, u_{rms}, indicated strong variations on both port and starboard sides for $\psi = 0°$ in Fig. 3.19. These high fluctuations were possibly related to the flow curling onto the flight deck from the

vertical superstructure edges. The fluctuations at the edges were also high for the quartering wind cases. However, for the $\psi = 10°$ case, the port side fluctuations were significantly higher and in the region containing a sharp velocity gradient. The sharp velocity gradient likely induced fluctuations, hence making the flow more turbulent. A similar result was observed for $\psi = 20°$ case, yet the fluctuations were also stronger on the starboard side, compared to

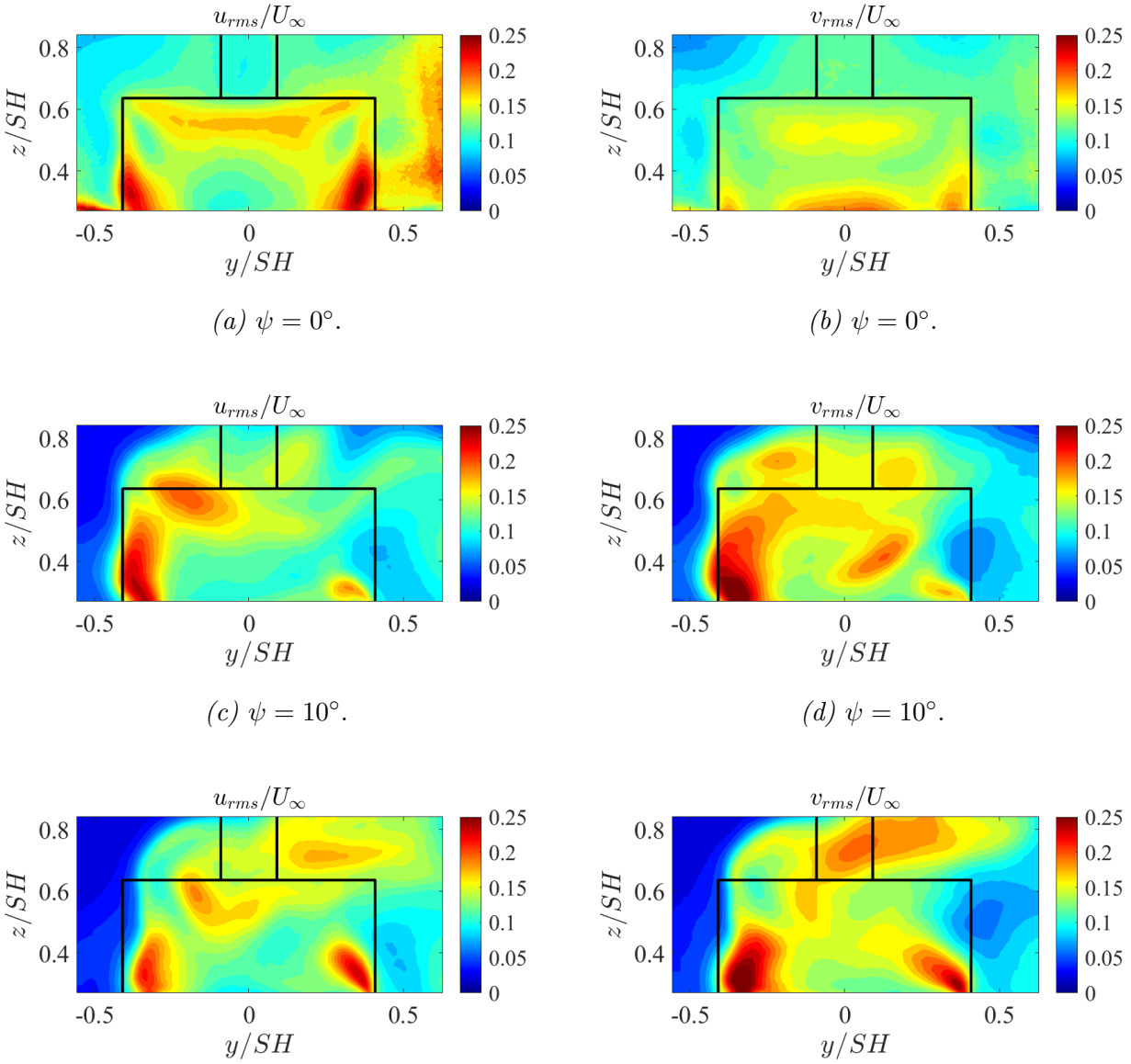

(a) $\psi = 0°$. *(b)* $\psi = 0°$.

(c) $\psi = 10°$. *(d)* $\psi = 10°$.

(e) $\psi = 20°$. *(f)* $\psi = 20°$.

Figure 3.19 Time-averaged streamwise & spanwise velocity fluctuation contours for crosswise Plane 2 (Figure 2.10a) for $U_\infty = 30.48$ m s^{-1}.

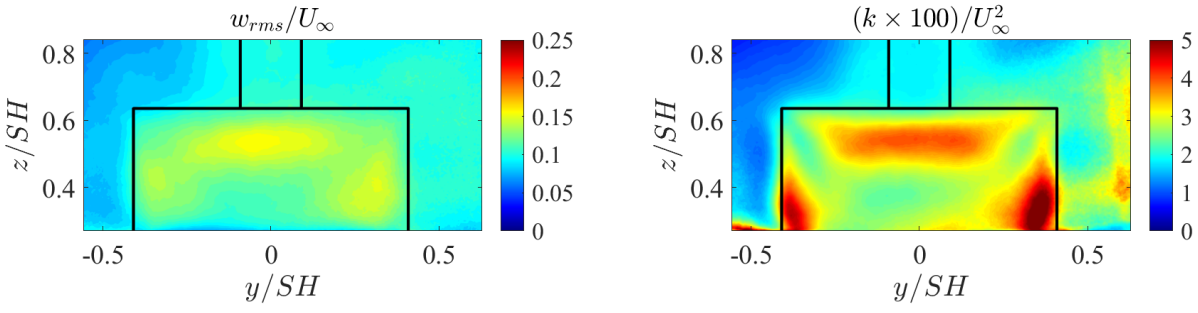

(a) $\psi = 0°$.

(b) $\psi = 0°$.

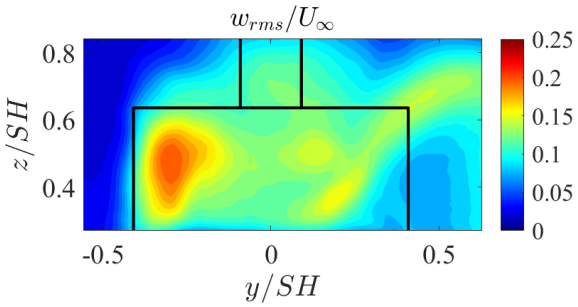

(c) $\psi = 10°$.

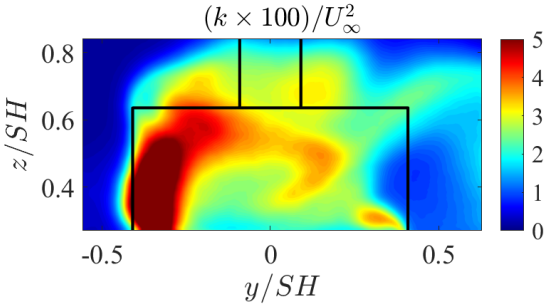

(d) $\psi = 10°$.

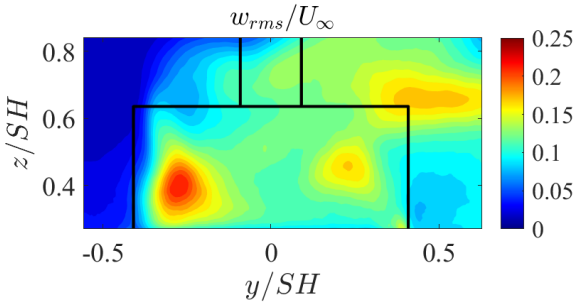

(e) $\psi = 20°$.

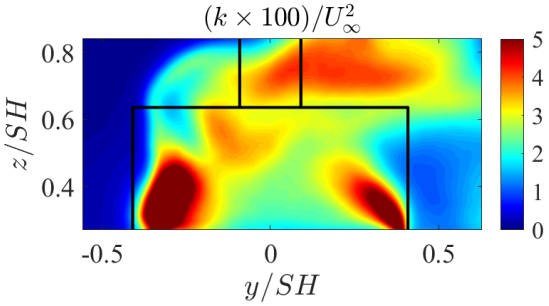

(f) $\psi = 20°$.

Figure 3.20 Time-averaged wall-normal velocity fluctuation & TKE contours for crosswise Plane 2 (Figure 2.10a) for $U_\infty = 30.48$ m s^{-1}.

the $\psi = 10°$ case. These starboard side fluctuations originated from the interaction with the leeward side flow field and the upwash. There were sharp velocity gradients located within this region, as seen in Fig. 3.14f.

The turbulent kinetic energy within the recirculation region was the highest out of all the crosswise planes. Figure 3.20 shows the highly energetic cross-sectional cut. Once again,

similarities between the spanwise and TKE contours were evident, which further suggested that a strong spanwise velocity component made the flow field more turbulent. The shift of the flow field was apparent from the TKE contours in Fig. 3.20. Minimal TKE region in the windward side increased in area as the angle became higher. Figure 3.19 also showed the energetic funnel wake having a presence downstream at crosswise Plane 2 and interacting

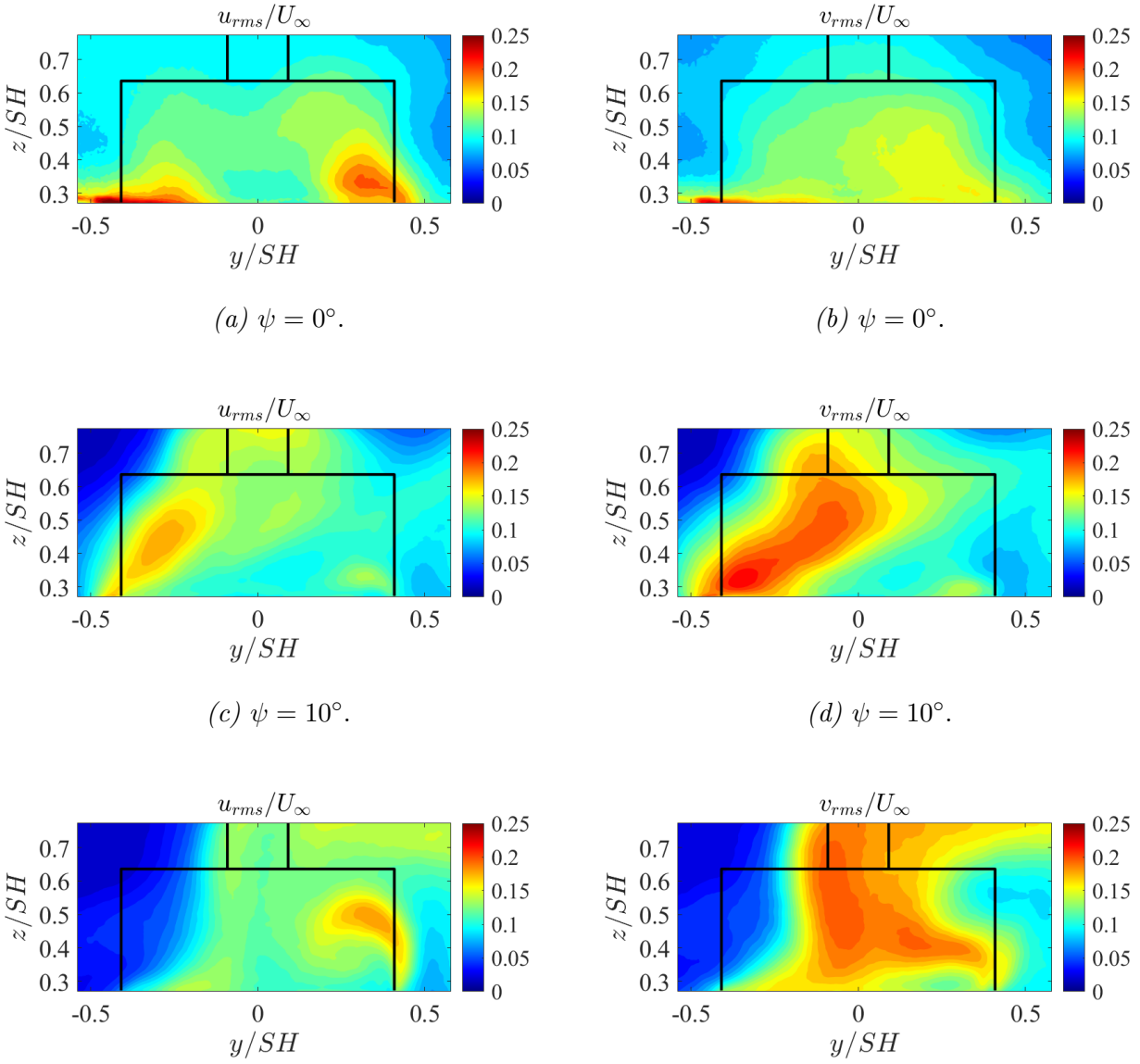

(a) $\psi = 0°$.

(b) $\psi = 0°$.

(c) $\psi = 10°$.

(d) $\psi = 10°$.

(e) $\psi = 20°$.

(f) $\psi = 20°$.

Figure 3.21 Time-averaged streamwise & spanwise velocity fluctuation contours for crosswise Plane 3 (Figure 2.10a) for $U_\infty = 30.48$ m s^{-1}.

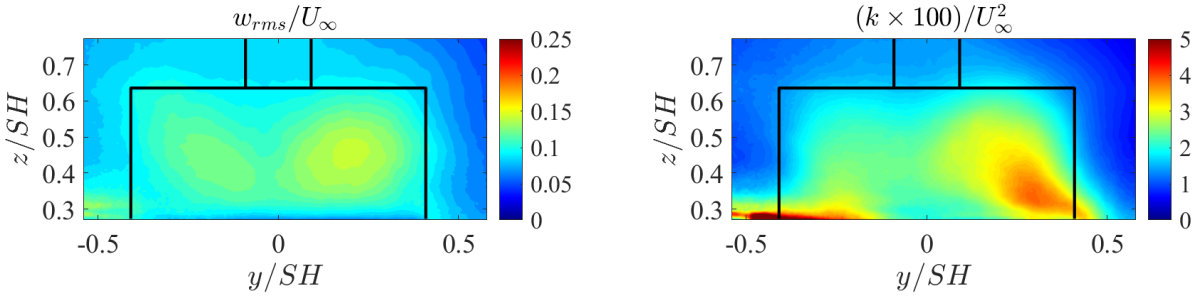

(a) $\psi = 0°$.

(b) $\psi = 0°$.

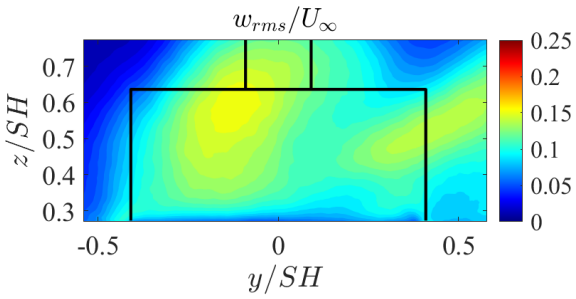

(c) $\psi = 10°$.

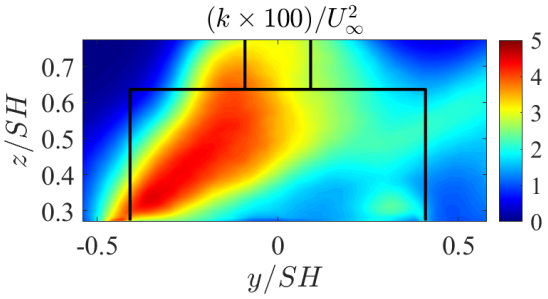

(d) $\psi = 10°$.

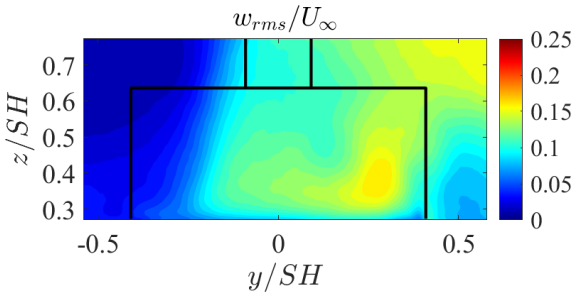

(e) $\psi = 20°$.

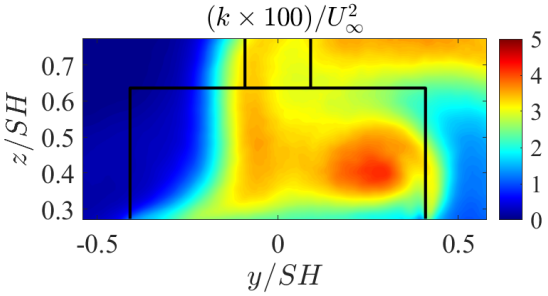

(f) $\psi = 20°$.

Figure 3.22 Time-averaged wall-normal velocity fluctuation & TKE contours for crosswise Plane 3 (Figure 2.10a) for $U_\infty = 30.48$ m s^{-1}.

with the leeward side flow field.

A similar trend found in crosswise Plane 1 & 2 was also observed in crosswise Plane 3. The high fluctuations were in the vicinity of sharp gradients and vortical structures, as seen in Fig. 3.15. The two near-wall fluctuations of the streamwise component for the headwind case were likely related to the flight deck vortices. Fluctuations for the $\psi = 10°$ were strong

(Fig. 3.21 & 3.22), considering the location of the crosswise plane was after the recirculation region. Nevertheless, it appeared that the fluctuations seen on the port side encapsulated the large flight deck vortical structure, but the entire FOV had more fluctuations for $\psi = 10°$. The sharp velocity gradients of Fig. 3.15f also contained high fluctuations. Interestingly, the port side region had a significantly larger area of minimal fluctuations. Turbulent kinetic energy at crosswise Plane 3 also closely matched the spanwise fluctuations. A difference in

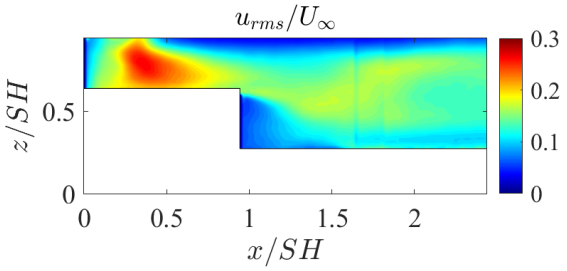

(a) $\psi = 10°$.

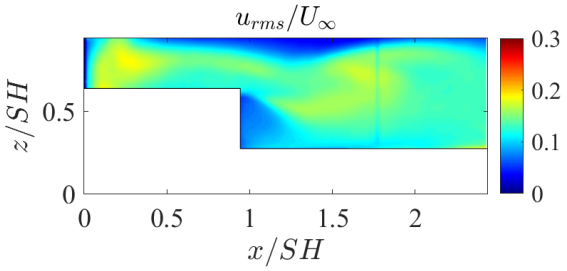

(b) $\psi = 20°$.

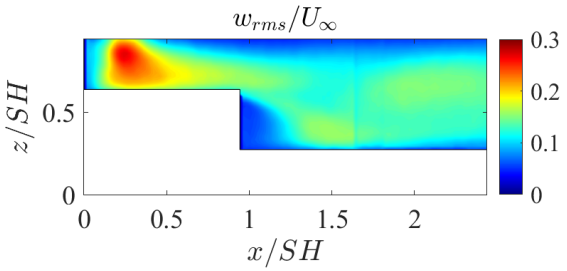

(c) $\psi = 10°$.

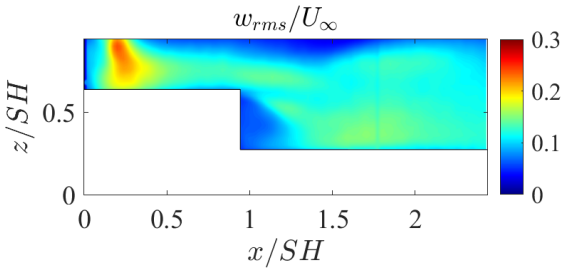

(d) $\psi = 20°$.

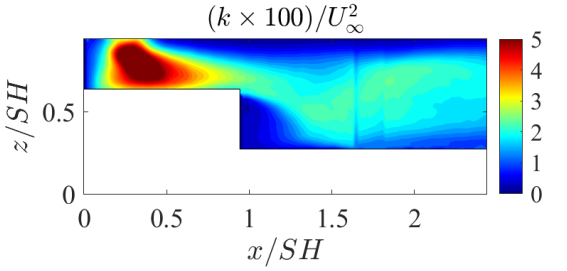

(e) $\psi = 10°$.

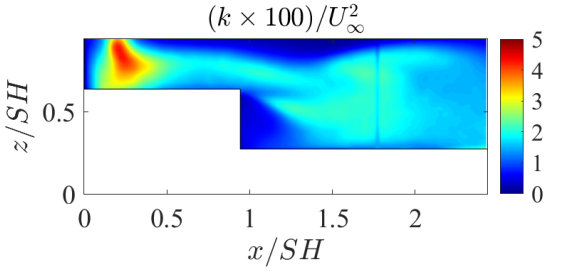

(f) $\psi = 20°$.

Figure 3.23 Time-averaged velocity fluctuation & TKE contours for streamwise Plane 1 (Figure 2.10b) for $U_\infty = 30.48$ m s^{-1}.

the TKE was noted for the $\psi = 20°$ case, where the TKE showed a very clear round flow structure (Fig. 3.22), indicating the strong flight deck vortex observed in Fig. 3.15f.

Lastly, the streamwise Plane 1 fluctuations and TKE are considered. Interestingly, the most turbulent region found in the streamwise plane for both quartering wind cases was the funnel wake, shown in Fig. 3.23. The $\psi = 10°$ case had significantly stronger fluctuations in the funnel wake than the $\psi = 20°$ case. This further suggested that the funnel wake had a strong presence in the $\psi = 10°$ case, whereas it was not as prominent at the centerline location for the $\psi = 20°$ case. High fluctuations, as well as TKE, were observed in the shear layer originating from the edge of the superstructure. Overall, the entire FOV contained more fluctuations as the quartering wind angle increases.

3.4 Effects of Simulated ABL

Reynolds number independence was shown for both cases with and without ABL in Section 3.2. The present section will consider only the most notable differences between the different configurations (Table 2.2). Time-averaged velocity and TKE contours for two measurement planes are covered similarly to Section 3.3.

A common difference between the configurations involving ABL and the ones without was the lower velocity magnitude across the entire FOV. This result was naturally caused by the simulated boundary layer, which had a velocity distribution shown in Fig. 2.4a. The maximum velocity seen across all crosswise planes and the streamwise plane was around $0.65U_\infty$. Flow field shape remained Reynolds number independent for the configurations with ABL. However, crosswise Plane 2 had some differences, excluding the lower magnitude. For the $\psi = 20°$ case in Fig. 3.24f, the secondary vortical structure previously observed in the case without ABL was no longer visible in the FOV. A closer inspection suggested that the vortical system was shifted towards the leeward side and outside the FOV. While it was the only difference observed throughout the crosswise planes, it was a peculiar finding which should not be present in a Re independent flow.

The configurations involving the ABL for the streamwise plane also had a comparable

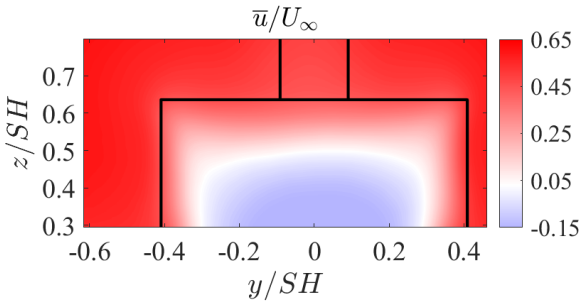

(a) $\psi = 0°$.

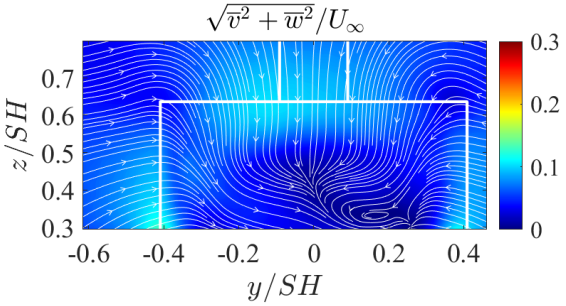

(b) $\psi = 0°$.

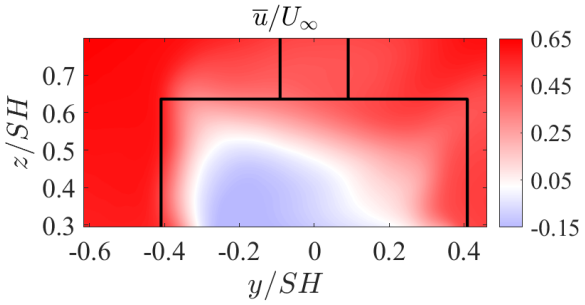

(c) $\psi = 10°$.

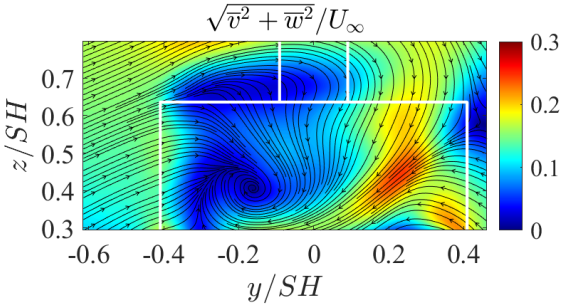

(d) $\psi = 10°$.

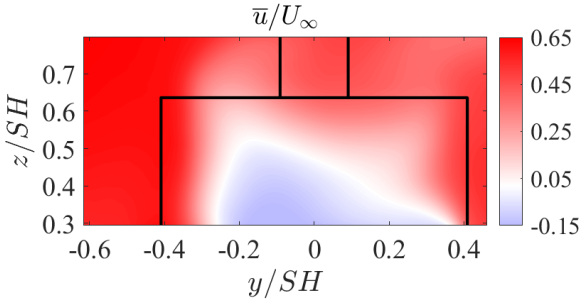

(e) $\psi = 20°$.

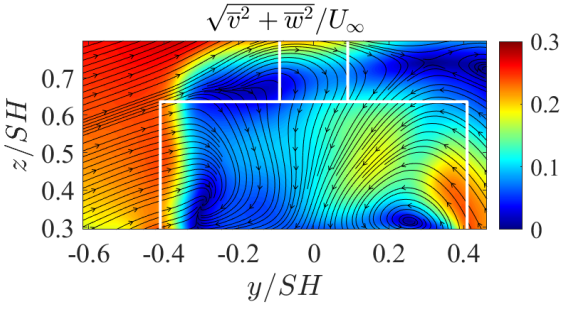

(f) $\psi = 20°$.

Figure 3.24 Time-averaged velocity contours for crosswise Plane 2 (Figure 2.10a) for $U_\infty = 30.48$ m s^{-1} with simulated atmospheric boundary layer.

$\psi = 0°$ case. A similar trend of lower free-stream velocity magnitude across the entire FOV was also seen in the streamwise measurements. The difference between the three quartering wind conditions is shown in Fig. 3.25 & 3.26. For the streamwise velocity, two clear recirculation regions were seen in the $\psi = 0°$ case. A major difference in the headwind case was the larger size of the recirculation region, which was qualitatively shown in the oil flow

visualization (Fig. 3.3). The second difference was seen in the wall-normal velocities for the headwind case. Figure 3.25b shows the wall-normal contour to be negative everywhere except for the two recirculation regions. For the quartering wind cases in Fig. 3.25d & 3.25f, there were areas outside the two recirculation regions containing positive wall-normal velocities. The $\psi = 10°$ case contained a larger region of negative wall-normal velocities when compared to the $\psi = 20°$ case. However, the spanwise results showed the existence of the same positive

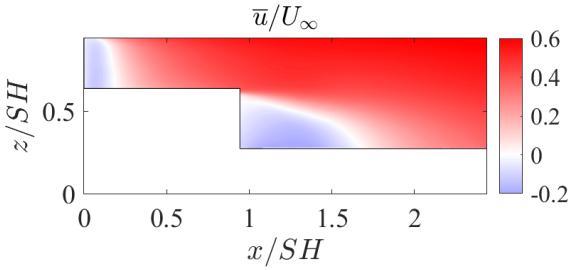

(a) $\psi = 0°$.

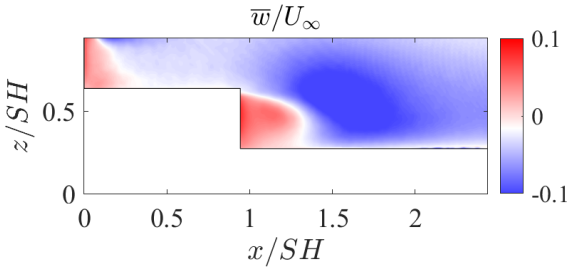

(b) $\psi = 0°$.

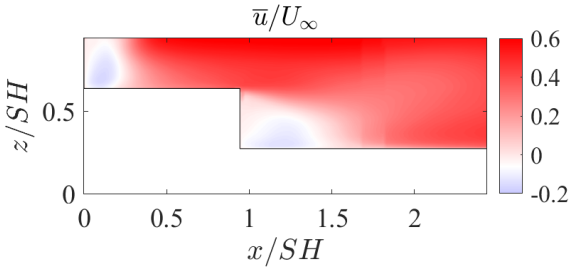

(c) $\psi = 10°$.

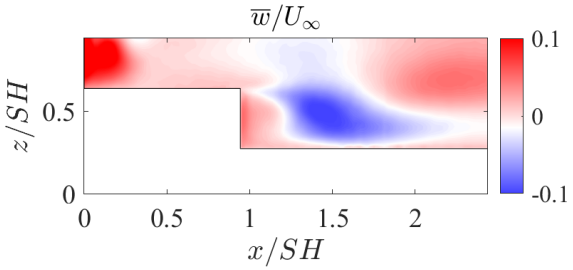

(d) $\psi = 10°$.

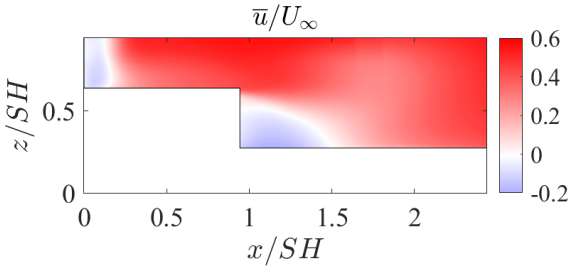

(e) $\psi = 20°$.

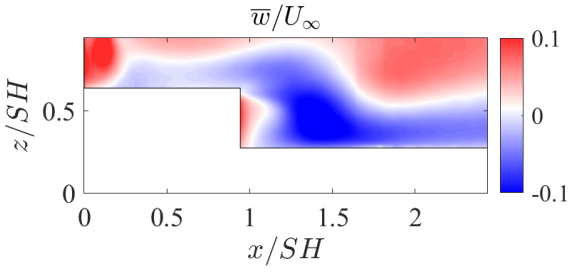

(f) $\psi = 20°$.

Figure 3.25 Time-averaged velocity contours for streamwise Plane 1 (Figure 2.10b) for $U_\infty = 30.48$ m s^{-1} with simulated atmospheric boundary layer.

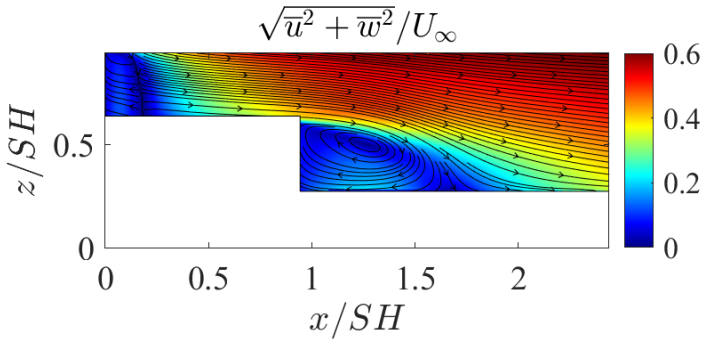

(a) $\psi = 0°$.

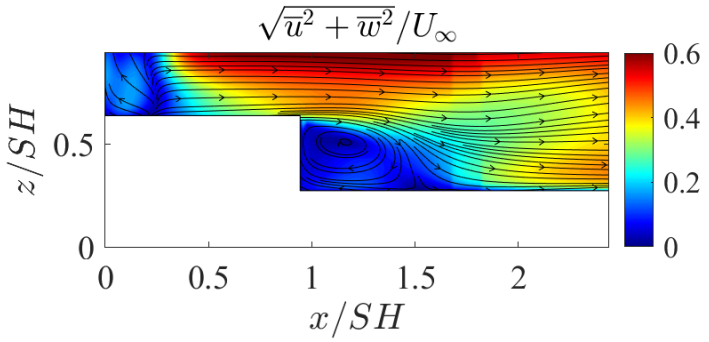

(b) $\psi = 10°$.

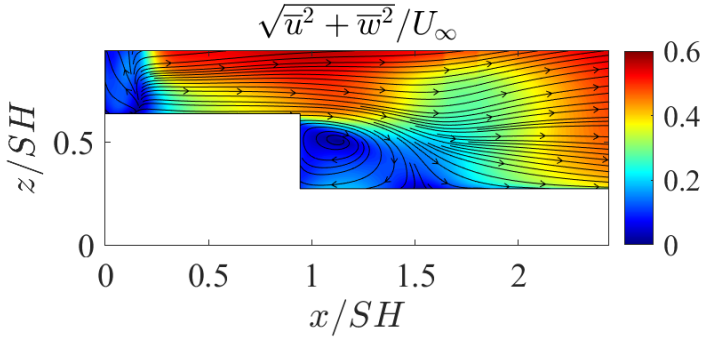

(c) $\psi = 20°$.

Figure 3.26 Time-averaged velocity magnitude and direction contours for streamwise Plane 1 (Figure 2.10b) for $U_\infty = 30.48$ m s^{-1} with simulated atmospheric boundary layer.

wall-normal velocity region in the location of crosswise Plane 3 (Fig. 3.25d). Additionally, for $\psi = 10°$, the immediate funnel wake region appeared to have wall-normal velocities close to zero. Likewise, the immediate funnel wake region for $\psi = 20°$ case in Fig. 3.25f also had low

wall-normal velocities. Considering that the wall-normal velocity variation was not large in the case without ABL, an artificial boundary layer further decreased the magnitude. However, with that being said, the overall flow field shape remained mostly consistent with the ABL.

Under the effects of a simulated ABL, decreased velocity magnitudes caused the fluctuations to decrease. The TKE contours for crosswise Plane 2 are shown in Fig. 3.27. Lower free-stream velocity magnitude had a significant effect on the TKE results. It is important to remember that atmospheric boundary layers include inherent turbulence, which was also generated by the simulated ABL, as seen in Fig. 2.4b. Thus, the TKE does not necessarily provide an accurate turbulent behavior of the flow field under the effect of the ABL. Nevertheless, the TKE in Fig. 3.27 showed the same trends observed in Section 3.3.2. For the quartering wind cases, the port side had energetic fluctuations, and the region above

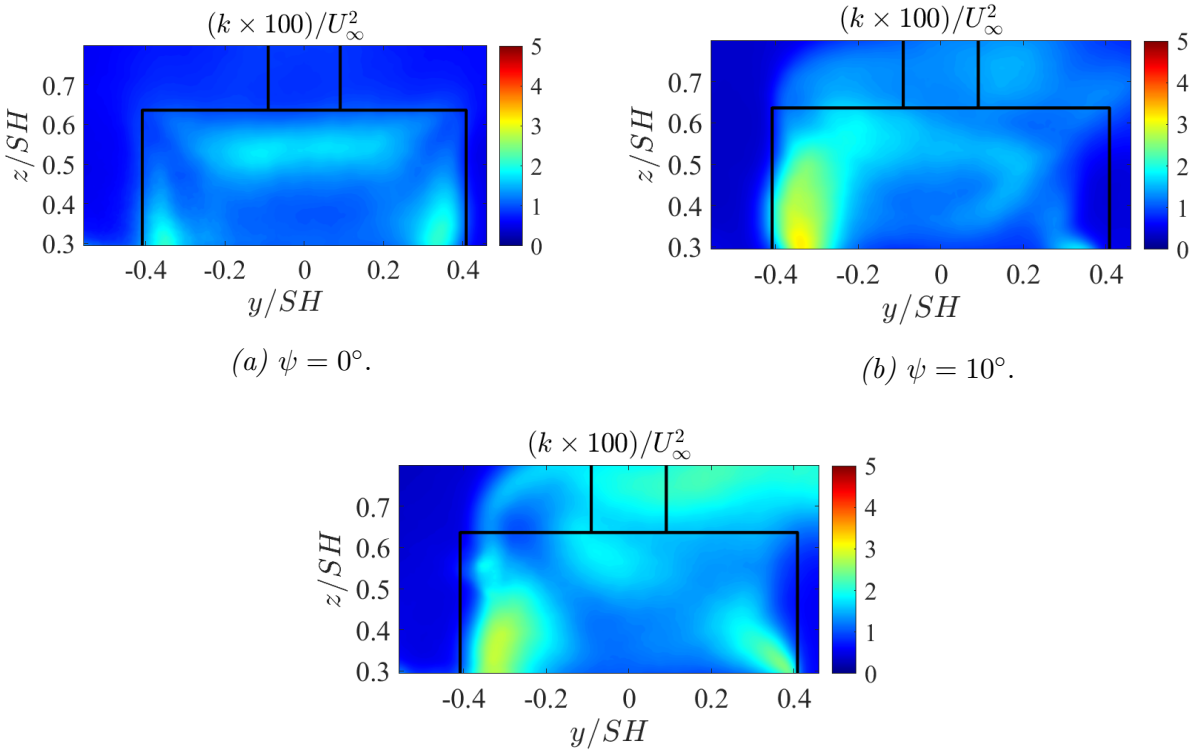

(a) $\psi = 0°$.

(b) $\psi = 10°$.

(c) $\psi = 20°$.

Figure 3.27 Turbulent kinetic energy (TKE) contours for crosswise Plane 2 (Figure 2.10a) for $U_\infty = 30.48$ m s^{-1} with the simulated atmospheric boundary layer.

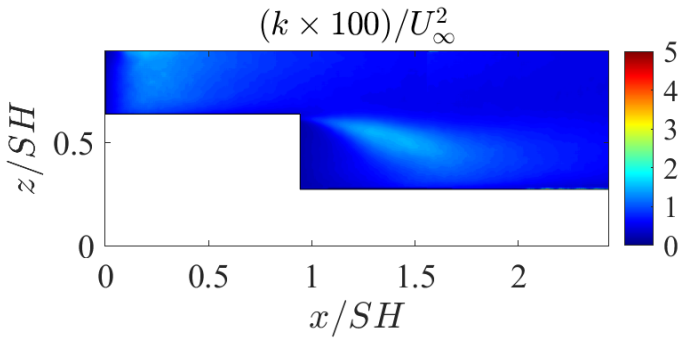

(a) $\psi = 0°$.

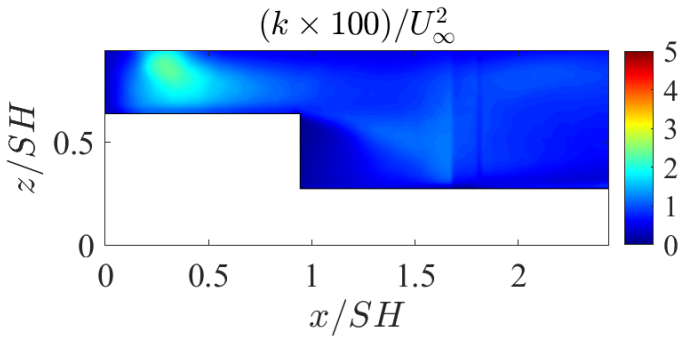

(b) $\psi = 10°$.

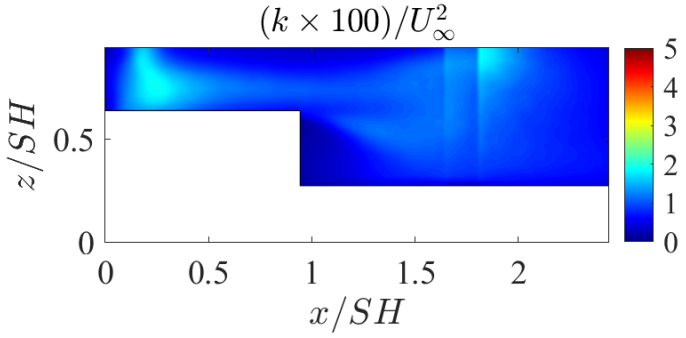

(c) $\psi = 20°$.

Figure 3.28 Turbulent kinetic energy (TKE) contours for streamwise Plane 1 (Figure 2.10b) for $U_\infty = 30.48$ m s^{-1} with the simulated atmospheric boundary layer.

the superstructure also contained more energy as the wake was further shifted towards the leeward side. Of course, the overall magnitude of the TKE was lower because it was a function of the velocity fluctuations. Similarly, for the streamwise Plane 1, Fig. 3.28 shows

the TKE contours. The headwind case in Fig. 3.28a showed the shear layer as one of the more energetic regions within the flow field. Conversely, the quartering wind cases had the most turbulent kinetic energy in the wake of the funnel, with the $\psi = 10^{\circ}$ case containing the most energy in that region.

The velocity fluctuation and TKE contours provided some insight into the turbulent behavior. However, they are insufficient to entirely quantify the turbulent airwake. Different tools are required to consider the more detailed changes in turbulence. The following Section 3.5 will address the airwake using other methods commonly utilized to analyze turbulent flows.

3.5 Turbulent Behavior of the Airwake

The turbulent content of the SFS2 airwake was explored using three different methods. Results covered in the present section were limited to the streamwise Plane 1 at 30.48 m s^{-1} (100 ft s^{-1}), and included the effects of the ABL.

From Section 3.3.2, energetic velocity fluctuations were observed in the funnel wake region and above the flight deck. Thus, spatial locations in these regions were considered as points of interest. For these locations, the differences caused by changes in yaw angle were studied. Specifically, the effects on the large-scale coherent motion. As mentioned in Section 1.2.3, the SFS2 airwake contained flows of such type, hence it is valuable to examine the changes caused by a yaw angle.

3.5.1 Spectral Analysis of the Airwake

Power spectral density can be used to analyze the energy content over a range of different frequencies. In Fig. 3.29, two different spatial locations are shown by the green markers. The green markers consisted of 9 neighboring points, from which the average was considered. These green markers were located in the regions that contained points of interest. The first location was within the funnel wake, seen in the plots on the left side of Fig. 3.29, and the second location, shown by the plots on the right side, was above the flight deck in the operating path of the helicopter. For both spatial locations, the PSD of the streamwise and

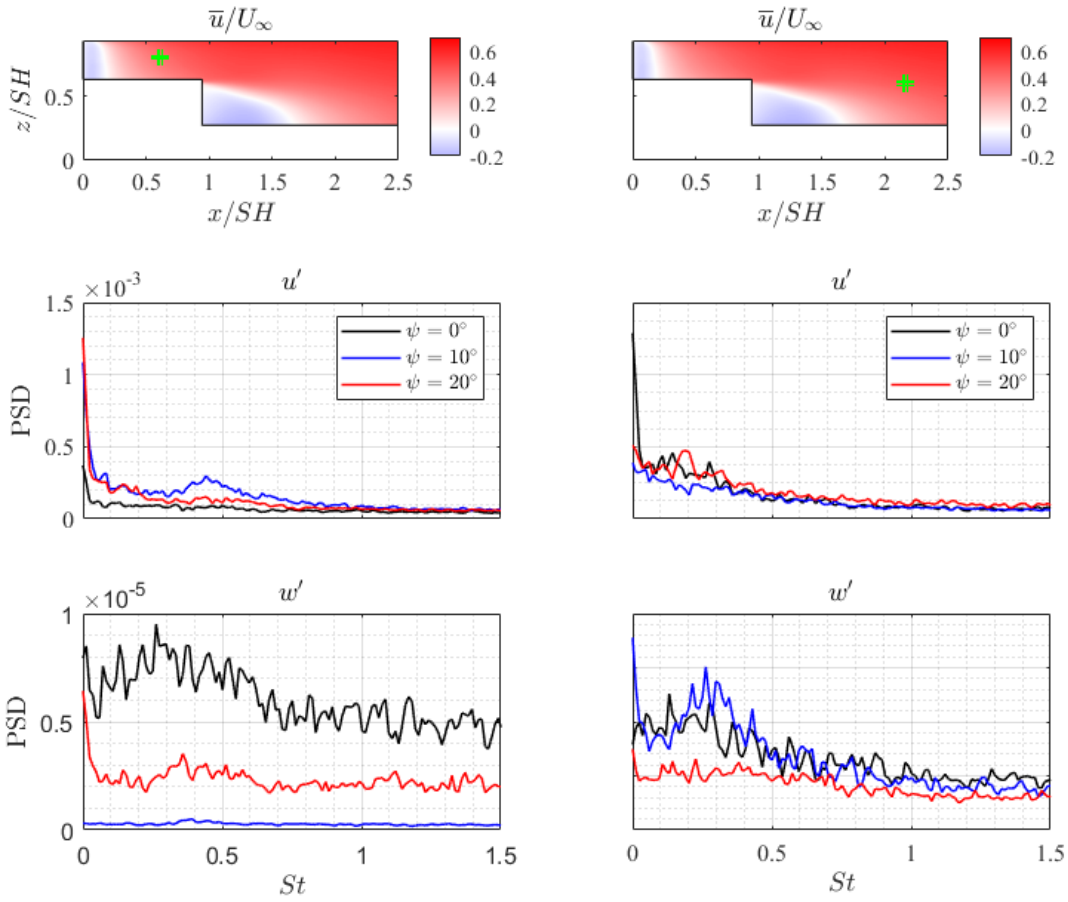

Figure 3.29 Power spectral density of streamwise and wall-normal velocity fluctuations normalized to U_∞^2. The two spatial locations are shown by the green dots on the time-averaged velocity contour. The line plots correspond to the spatial locations.

wall-normal velocity fluctuations was shown below the velocity contours. The headwind case was represented by the black color, the $\psi = 10°$ by the blue color, and the $\psi = 20°$ by the red color.

The results captured by the PSD displayed some conflicting findings in the funnel wake region (Fig. 3.29). Analysis of the velocity fluctuations in Section 3.3.2 suggested the $\psi = 10°$ case had the most energetic funnel wake for both velocity components. The PSD revealed that the $\psi = 10°$ case was just as energetic as the $\psi = 20°$ case for the streamwise velocity fluctuations, u'. However, a clear peak was present between $St \in [0.4, 0.5]$, which was likely

caused by a more energetic higher frequency flow structure. The dominant vortex shedding frequency for a full-scale ship lies in the range of $St \in [0.16, 0.25]$ [17], which is significantly lower than the observed St value of the peak. Conversely, the wall-normal PSD appeared to be the least energetic out of the three cases across the entire St range. Recalling the observation made in Section 3.4, for the $\psi = 10°$ case, the wall-normal velocities were close to zero at this point of interest (Fig. 3.25d). The low wall-normal velocity was a contributor to a less energetic PSD result. Therefore, it is likely that the streamwise flow was considerably more dominant in the funnel wake for the $\psi = 10°$ case, whereas the other two cases did not have such a distinct difference between the two velocity components.

Inspecting the other point of interest, located at the flight deck, no clear distinctions can be made (Fig. 3.29). Unlike the funnel wake location, the flight deck region appeared to remain consistent between the two quartering wind cases and the headwind case. Minor deviations were present, however, they can be considered negligible as the scale of these differences was very small. It is likely that a different outcome would be observed if a point closer to the recirculation region, or the flight deck surface was picked. Although the current choice was in the vicinity of the reduced streamwise flow and the strong spanwise gradients seen in Fig. 3.25 & 3.15, the spectral analysis showed no significant difference at this location.

3.5.2 Coherent Motion of the Flow Field

The selected locations had some coherent structures passing through them. For the flight deck point, Fig. 3.30 shows that for R_{uu} there was a large area in coherent motion for $\psi = 0°$, which is indicative of a large-scale structure or eddy passing by. The correlation coefficient R_{uu} describes the u' fluctuation propagation in the same general direction as the surrounding u' fluctuations, hence they are correlated. Referring to the $\psi = 0°$ case, the area with inverse correlation for R_{uu} was clearly the recirculation region, which was already found to have an upstream streamwise flow component (Fig. 3.25a). Thus, the two-point correlation agreed with the previous findings and revealed large coherent motion in the headwind case. Similarly, the wall-normal correlation coefficient, R_{ww}, suggested a strong coherent flow

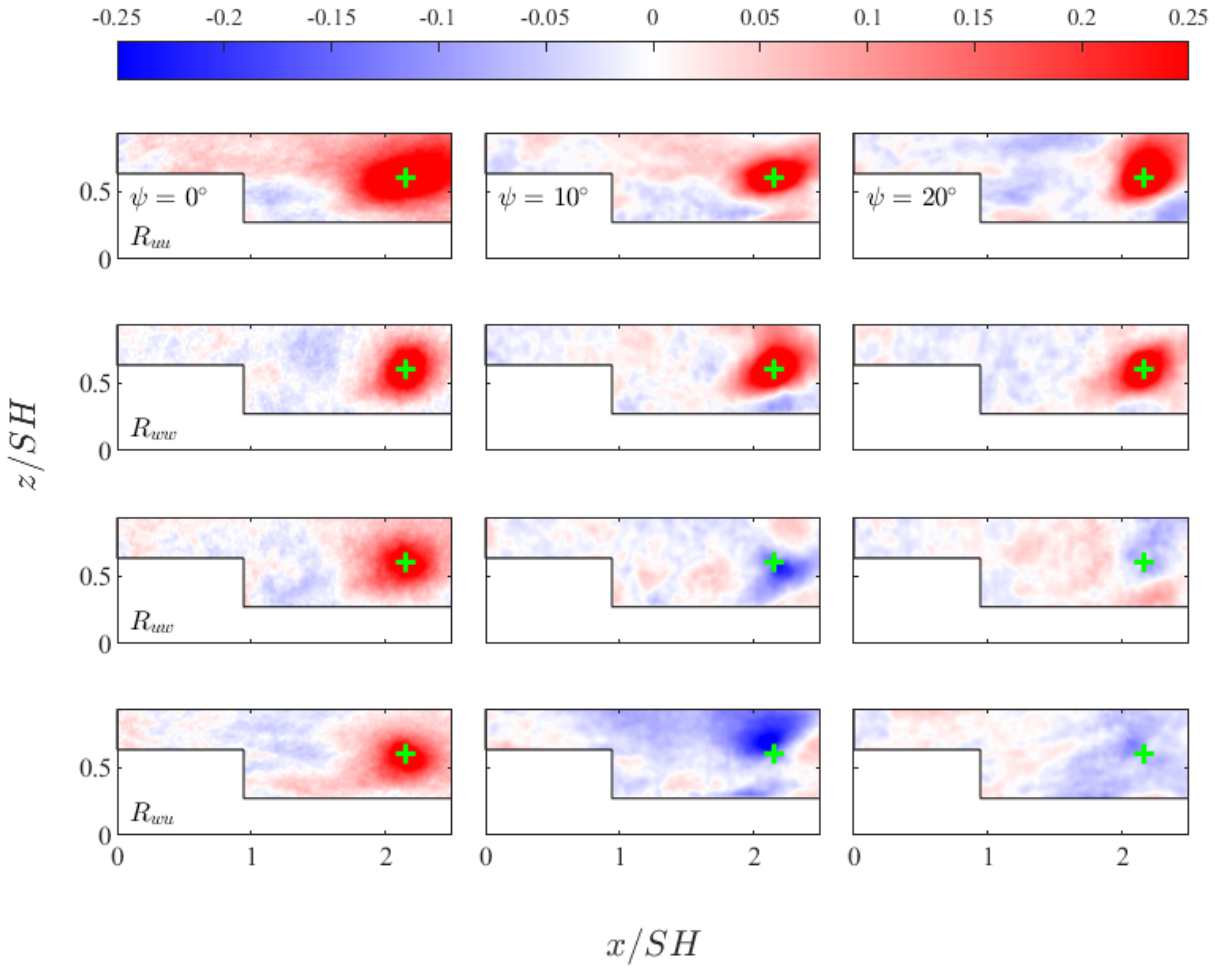

Figure 3.30 Two-point correlation contours for different R_{ij} cases, located in the flight deck region indicated by the green cross.

structure passing through the selected location. However, this structure did not appear to be as large or widespread as the one for R_{uu} case. Finally, the two remaining correlation coefficients, R_{uw} and R_{wu}, showed the correlation between fluctuations in u' and w'. As an example, for R_{uw}, positive fluctuations in w' will be correlated with positive fluctuations in u', which was seen as the red contour in Fig. 3.30. Conversely, a positive fluctuation in w' will be uncorrelated with negative fluctuations in u', which was seen as the blue contour in Fig. 3.30. The same principal applies to R_{wu}, except it is reversed.

Two-point correlation revealed a large coherent structure in the R_{uu} contour for the $\psi = 10°$ case (Fig. 3.30). The strength of the correlation appeared to be weaker when

compared to the headwind case. Additionally, the wall-normal correlation, R_{ww}, was more widespread. The contour of R_{uw} for $\psi = 10°$ closely resembled the observed large vortical structure in the flight deck region. The correlation coefficient R_{uw} showed that for the positive fluctuations in w', the fluctuations of u' in the immediate vicinity were negatively correlated, suggesting a movement in the upstream direction. Recalling Fig. 3.26b, the general area in which the point of interest was located had reduced streamwise velocity and a positive wall-normal velocity region. The two-point correlation findings were consistent with the qualitative time-averaged velocity contour results for the $\psi = 10°$. As for the $\psi = 20°$ case, a distinct large coherent motion was not present outside of the local area of the green cross location (Fig. 3.30). The fluctuation motion shown by R_{uw} and R_{wu} was not easily relatable to the time-averaged results. Negative u' fluctuations appeared to occur for R_{uw} in the same region where the reduced streamwise velocity was observed. However, the areas with positive fluctuations in w' had a negative time-averaged wall-normal velocity, resulting in a different behavior than expected. Unlike the $\psi = 10°$ case, the $\psi = 20°$ case had more regions with some correlation across the flight deck for both R_{uw} and R_{wu}.

The second point of interest, located in the funnel wake, provided a different perspective on the flow field. A region with high correlation R_{uu} was observed in Fig. 3.31 for both the headwind and $\psi = 10°$ cases. This location appeared to be under the same influence of the large-scale eddy passing through the airwake, as seen in Fig. 3.30. The region of R_{uu} correlation was reduced for the $\psi = 20°$ case, which was also observed by the two-point correlation for the flight deck point of interest. The strong correlation extended beyond $x/SH = 1$ and reached the half-way point of the flight deck ($\psi = 20°$ in Fig. 3.31). Recalling the observations from crosswise plane velocity contours in Section 3.3.1, crosswise Plane 2 for $\psi = 20°$ displayed the same two vortical structures captured in crosswise Plane 1. The two-point correlation for R_{uu} suggested a stronger coherent motion between the first two crosswise planes. Nevertheless, the $\psi = 20°$ case R_{uu} correlation region was not as large as for the other two cases. Interestingly, for the two quartering wind cases, the funnel recirculation

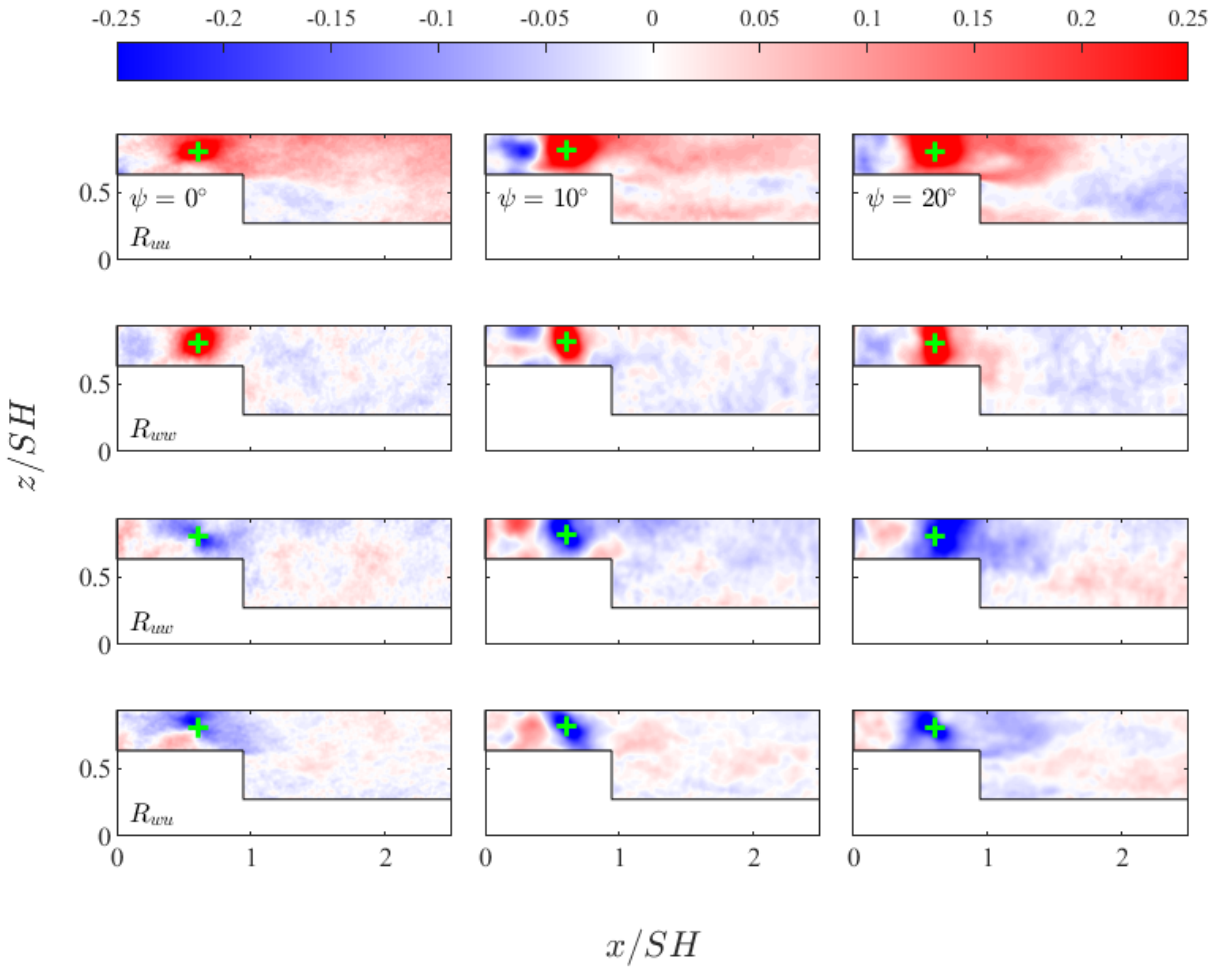

Figure 3.31 Two-point correlation contours for different R_{ij} cases, located in the funnel wake region indicated by the green cross.

region fluctuations were negatively correlated to the point of interest. The TKE contour in Fig. 3.28 showed energetic funnel wake behavior for $\psi = 10°$ and $\psi = 20°$. Two-point correlation distinguished the funnel wake separately from the surrounding flow field.

Wall-normal correlation R_{ww} in Fig. 3.31 showed minimal relation to the locations outside the immediate point of interest. For all three cases, the wall-normal fluctuations did not have a strong coherent motion. The PSD for the funnel wake point of interest (Fig. 3.29) showed that the wall-normal fluctuations were less energetic compared to the streamwise fluctuations. Additionally, the $\psi = 10°$ case displayed the least energetic results. Relating the results, the two-point correlation of R_{ww} for the $\psi = 10°$ case did not have a coherent motion region as

large as the headwind and $\psi = 20°$ cases. Thus, the $\psi = 10°$ case appeared to have motion more dominant in the streamwise direction. Of course, the same was true for the headwind and $\psi = 20°$ cases, however, the difference in the $\psi = 10°$ case was more profound.

The correlations for R_{uw} and R_{wu} showed overall similar trends with some differences in between. The point of interest in Fig. 3.31 was negatively correlated to the surrounding area for all cases. However, as seen in Fig. 3.30, the flow in the flight deck region had positive correlation for u' and w' fluctuations, with some exception in the $\psi = 10°$ case. For the $\psi = 20°$ case, the R_{uw} and R_{wu} correlations displayed similar behavior in Fig. 3.30 & Fig. 3.31. The immediate surrounding area around the selected green cross location in the funnel wake was negatively correlated (Fig. 3.31), whereas the area that contained the green cross location on the flight deck had positive correlation. Likewise, the reverse was seen in Fig. 3.30.

Overall, the two-point correlations suggested strong coherent motion for R_{uu}. In the cases with quartering wind conditions, the passing largest coherent structure appeared to decrease. However, it is possible that only a section of the overall structure was observed. The airwake was shifted towards the leeward side, which likely pushed the direction of the passing eddy away from the plane of symmetry of the SFS2 model, which resulted in a smaller cross-sectional cut of the eddy. Additional streamwise measurements are needed at different locations away from the symmetry plane to investigate this behavior. However, based on the crosswise plane measurements, the leeward side had significant interactions with the flight deck flow field (Fig. 3.14 & 3.15), which likely indicates a larger region of coherent motion for R_{uu}. The PSD result alluded to this behavior as well. The SFS2 airwake contained large-scale low-frequency structures. However, the PSD did not show the higher frequency content as more energetic in Fig. 3.29, which implies that the airwake remained primarily dominated by low-frequency content. Thus, the two-point correlation did not necessarily imply a smaller-scale eddy. Instead, it likely captured a portion of the passing coherent structure.

3.5.3 Contribution of the Decomposed Flow

A different way to study the coherence within the fluid flow is to decompose the flow field into energy containing modes. Proper orthogonal decomposition provides ordered modes, from highest to lowest, based on their total fluctuating kinetic energy [33]. The different modes can be used to reconstruct the original flow field. If a small number of modes capture a high percentage of the energy, POD can be used to isolate certain modes and study their impact on the flow field. A similar approach was performed for the SFS2 airwake with different quartering wind conditions.

The streamwise plane results were decomposed and the first 10 modes are shown in Fig. 3.32. The singular value decay was represented by the lines containing circular markers. This decay showed the variation of the ordered energetic modes, with the first mode being

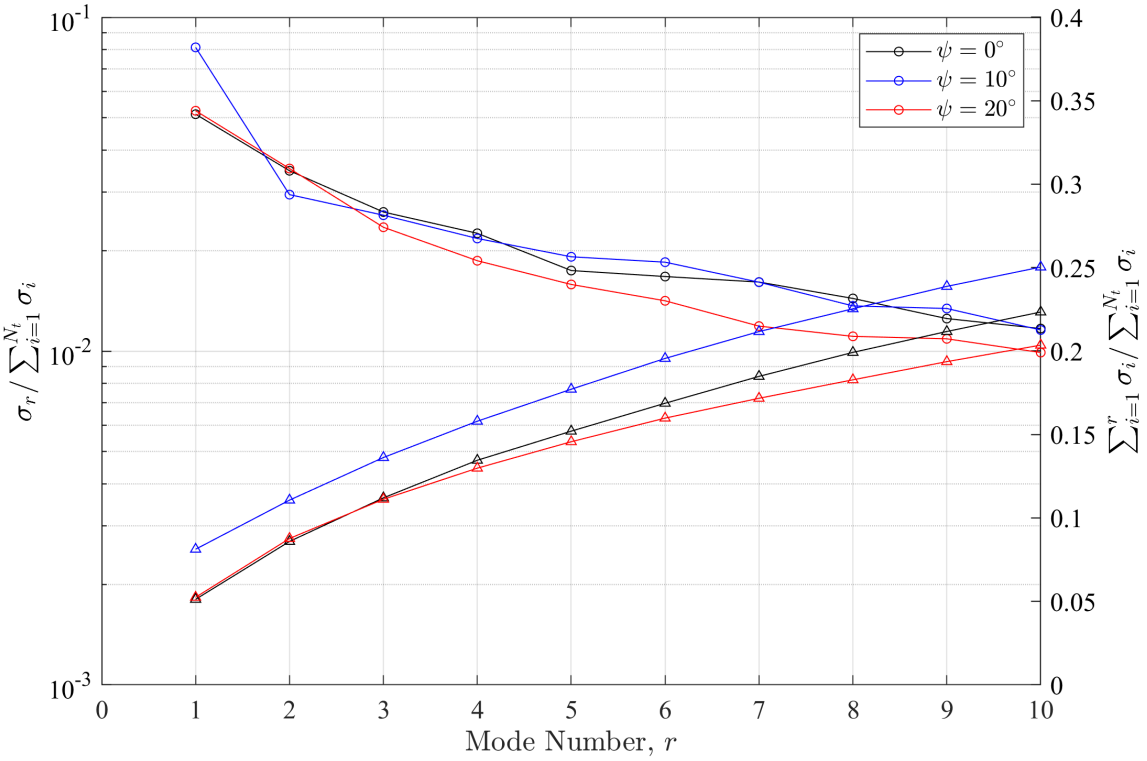

Figure 3.32 The singular value decay and cumulative sum for the first ten modes from POD calculation. Circles indicate the singular value decay, and triangles show to the cumulative sum.

the most energetic, hence, a decreasing trend is expected as each following mode contains less energy than the previous one. The singular value decay was normalized by the total energy contained within the singular values. The first mode was seen to contain around 8% of the total energy for the $\psi = 10°$ case, with the second mode dropping to around 3%. Likewise, the lines with the triangular markers in Fig. 3.32 represented the cumulative sum of the modes. This cumulative sum represented the total combined energy of a specific mode and the preceding ones before it. In Fig. 3.32, the cumulative sum for the $\psi = 10°$ case showed the first mode containing approximately 8% of the total energy, and the second mode having around 11% of the total energy, which was simply the combined energy of the first two modes. Thus, the cumulative sum is expected to increase with each mode and reach a final value of 1 at the maximum number of modes. The cumulative sum represents the total energy of the flow field captured by the modes. Generally, if fewer modes are needed to capture approximately 90% of the energy, then the flow field contains strong coherent motion, and each energetic mode can be better related to the observed flow patterns.

Singular values of the SFS2 streamwise plane suggested a complex turbulent flow field. A total of around $1,000$ modes were needed to capture 90% of the energy within the flow field. The total number of modes was equivalent to the number of images (Table 2.4). Thus, the high number of modes implied that the airwake was highly turbulent, and coherent motion is challenging to capture. Instead of considering the $1,000$ modes, the first 10 modes can be studied as they are the most energetic. The singular values in Fig. 3.32 for $\psi = 10°$ revealed consistent findings with the TKE, PSD, and two-point correlation results. It was previously observed that the $\psi = 10°$ contained strong coherent motion and had a high turbulent kinetic energy. This was seen by the first mode of $\psi = 10°$ case in Fig. 3.32 capturing around 8% of the total energy, whereas the first mode for the headwind and $\psi = 20°$ case captured around 5%. Cumulatively, the first 10 modes for the $\psi = 10°$ case contributed to around 25% of the energy, which was higher than the other two cases. Despite having a higher first mode, the $\psi = 10°$ case closely matched the headwind case, which was also observed in Fig. 3.30,

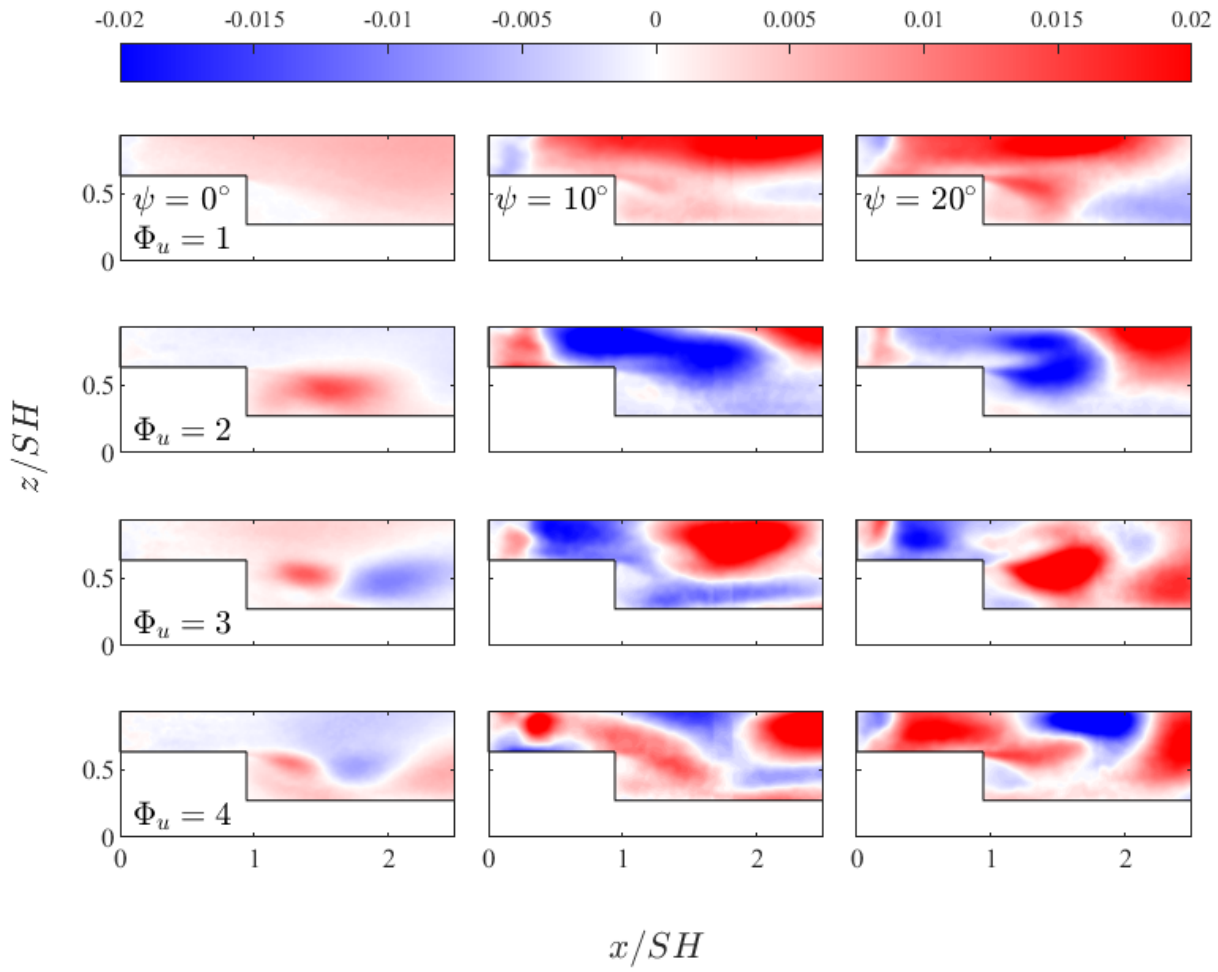

Figure 3.33 First four spatial basis modes of u-velocity component for three different yaw angles.

suggesting a strong coherent motion. Conversely, the $\psi = 20°$ case had less energetic modes after Mode 3, and started to differ from the headwind and $\psi = 10°$ cases.

A closer inspection of the first 4 spatial modes is shown in Fig. 3.33 & 3.34. The contours show the same modes that were referred to in the discussion of singular values. However, these spatial modes were separated into the streamwise spatial basis Φ_u (Fig. 3.33) and wall-normal spatial basis Φ_w (Fig. 3.34). It is worth noting that the scale of the contours was arbitrary, unlike the correlation contours in Fig. 3.30 & 3.31. The dimmer headwind case was caused by a finer spacing between the x and z coordinates, whereas the spacing for the quartering wind cases was the same. Nevertheless, the only difference caused by the finer

spacing was the contrast of the headwind results.

The first mode in Fig. 3.33 resembled the R_{uu} correlation from Fig. 3.30 for all three cases. It appeared that this first mode also contained the large-scale coherent motion from previous observations. Interestingly, the spatial basis modes for Φ_u and Φ_w had significant resemblance between them for each case seen in Fig. 3.33 & 3.34. This observation makes sense, since the velocity fluctuations were correlated. The behavior of these velocity fluctuations was also influenced by the passing eddies, which vary in scale and energy levels. It is also apparent that the first mode in Fig. 3.33 closely resembles the shape of the mean flow for the headwind case seen in Fig. 3.25a. While the two-point correlation revealed the more dominant streamwise

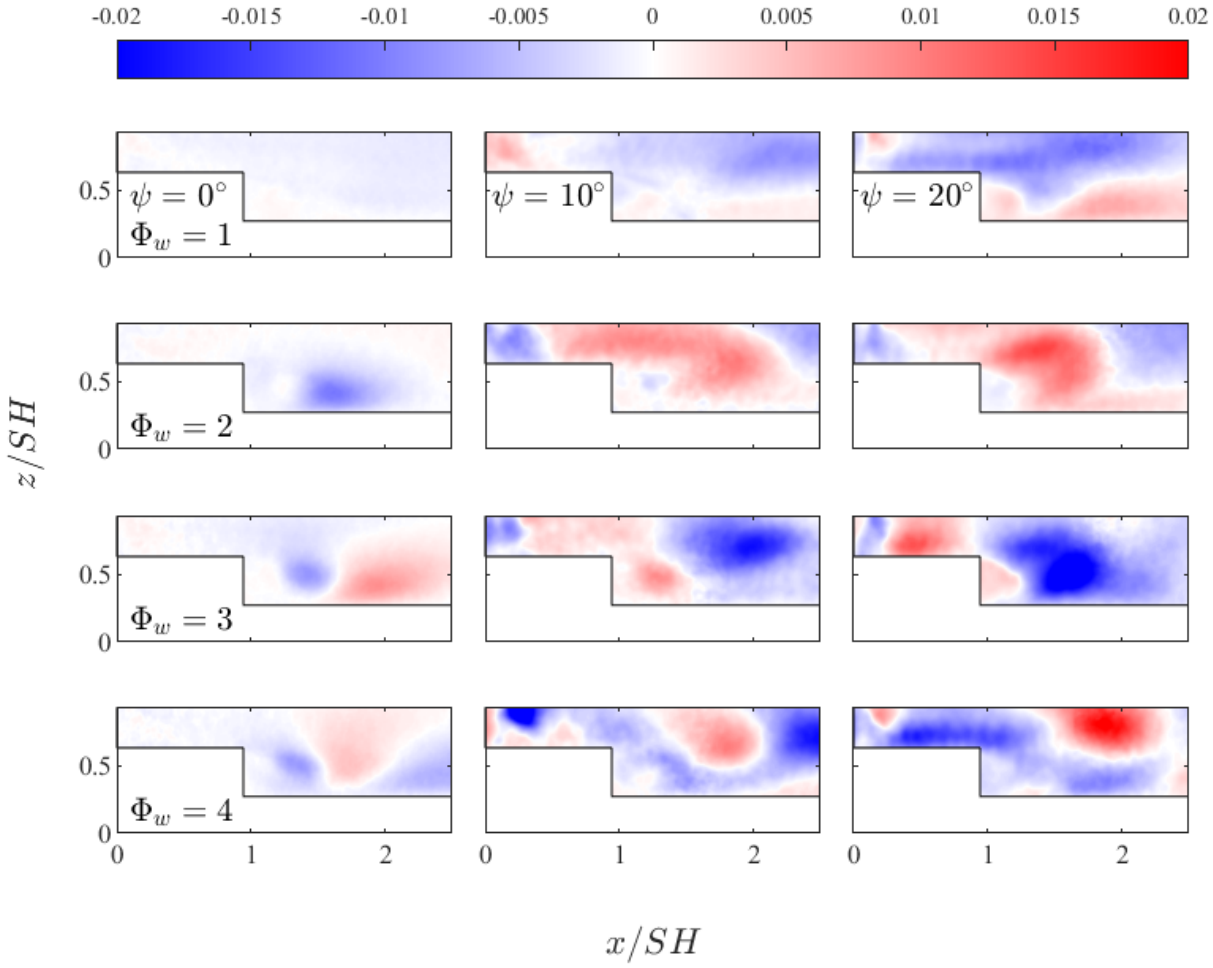

Figure 3.34 First four spatial basis modes of w-velocity component for three different yaw angles.

coherence, the POD modes provided insight into the other, less energetic, coherent motions.

A relation between the modes and the time-averaged flow contours was evident through a closer examination. Particularly, Mode 2 for the $\psi = 10°$ case had a large area covered in blue throughout the flight deck in Fig. 3.33. The time-averaged velocity contour for crosswise Plane 3 (Fig. 3.15c) revealed a large region of flow with lower streamwise velocity spanning throughout the flight deck FOV. Additionally, the cross-sectional contour indicated that the flow had a vortical behavior at that location. Considering the reduced streamwise velocity, Mode 2 appeared to capture such a region in Fig. 3.33 for $\psi = 10°$. Likewise, Modes 3 and 4 further alluded to the same observed structure, only capturing different aspects related to it. For instance, Mode 3 appeared to distinguish the region above the flight deck where reduced streamwise velocity was observed in Fig. 3.25c, which is shown as a region in red for $\Phi_u = 3$ in Fig. 3.33. As for Mode 4, it separated the flow into three coherent regions on the flight deck: one related to the recirculation region, another to the intermediate slower velocity directly after the recirculation region, and the third region appeared to be related to the vortical movement nearing the end of the flight deck.

The $\psi = 20°$ case had similar distinctions between its modes in Fig. 3.33. Recalling the time-averaged crosswise plane velocity contours, the $\psi = 20°$ case had a reduced streamwise velocity region spanning across the flight deck FOV as well (Fig. 3.24e). This region was captured by Mode 2 in Fig. 3.33. It appears that for the $\psi = 20°$ case, this region was not as widespread as it was for the $\psi = 10°$ case. However, it appeared to be influenced more by the recirculation region across all four modes. Mode 3 captured the region of the funnel wake, and suggested that it was separate from the coherent flow on the flight deck, unlike Mode 3 in the $\psi = 10°$ case. Finally, Mode 4 seemed to have three major distinct regions in the FOV as well. The first one was the flow coming from the funnel wake shown in red, the second region had the reduced streamwise flow spanning above the flight deck (Fig. 3.25e) shown in blue, and the final region was related to the flow leaving the flight deck.

In the case of the SFS2 airwake, the simple POD did not necessarily relate the different

spatial modes to the actual flow structures observed. An attempt was made to interpret these measurements using POD. However, the complexity of the airwake had more nuances within. Thus, a way of filtering the airwake, for instance into frequency bands, might provide more valuable insight of the intricacies within. Methods such as SPOD can filter the flow field into different frequency bands, or multi-scale POD that splits the correlation matrix into the contribution of different scales [34]. Such POD methods could be useful if a specific flow structure is studied.

4 Conclusions

Time-resolved particle image velocimetry (TR-PIV) measurements and surface oil flow visualization were performed on the Simple Frigate Shape No. 2 (SFS2) model for two different quartering wind conditions of $\psi = 10°$ and $\psi = 20°$. The study was carried out at the Embry-Riddle Aeronautical University Low-Speed Wind Tunnel Facility. Three crosswise planes of interest were measured, as well as a single streamwise plane. Measurements were made in the Reynolds number range of 3.2 through 6.4 million based on ship length, for a total of eight different configurations. The configurations varied based on TR-PIV type, inclusion of Cowdrey rods to simulate the atmospheric boundary layer (ABL), and the yaw angle.

The results were compared with the headwind case and revealed significant differences within the flow field. Qualitative results showed strong asymmetry throughout the airwake for both quartering wind cases. The flow field showed insignificant variation with Reynolds number even in a yawed setting. Effects of the simulated ABL were also explored. The airwake was further investigated through a spectral analysis, two-point correlation, and proper orthogonal decomposition (POD). Results were related to the observed qualitative phenomena within the airwake, and differences were established. In short, the outcome from the work contributes to the dynamic interface (DI) problem by providing a more extensive basis of the SFS2 airwake with quartering wind conditions. Many of the intricacies within the airwake remain unexplored, specifically for different variations of quartering winds. Therefore, the present research fills in some gaps related to airwakes with $\psi = 10°$ and $\psi = 20°$.

4.1 Summary of Conclusions

The objectives of the present research have been outlined in Section 1.3 and the outcomes and conclusions made are now addressed in the same order.

1. Significant differences within the flow field were identified for the two quartering wind cases compared to the headwind case. Prior work in the literature has described the

complexity and asymmetry of the recirculation region observed within the airwake. This research found significant differences in the flow field at the funnel wake, recirculation region, and flight deck. The flow characterization was performed using surface oil flow visualization and time-resolved particle image velocimetery (TR-PIV) measurements.

(a) Surface oil flow visualization showed a clear difference in the development of funnel wake with quartering wind conditions. At this location, no horseshoe vortices were present. Instead, a windward side trailing vortex, originating from the front corner of the superstructure, was identified. The funnel wake for the $\psi = 10°$ case had an area of flow separation on the leeward side, which suggested the wake was moved. Nevertheless, the $\psi = 10°$ funnel wake had a more substantial presence and interaction with the port side trailing vortex.

Similar results were observed for the $\psi = 20°$ case, but the interaction with the trailing vortex was not as profound, and the airwake appeared to be moved further towards the leeward side. The flow separation region there showed an interaction with the upwash from the leeward side. The flight deck surface flow contours shared more similarities for both quartering wind cases. The recirculation region appeared to decrease and become asymmetric. Flow separation on the port and starboard side edges was evident, and an upwash from the leeward side, which interacted with the flight deck flow field. This interaction was found to be more profound for the $\psi = 20°$ case.

(b) The TR-PIV measurements revealed the time-averaged velocity flow field of the three crosswise planes and a single streamwise plane. Crosswise Plane 1, located on top of the superstructure, showed an asymmetry of the funnel wake. In addition, the trailing vortex was observed to be closer to the symmetry plane of the ship, which suggested an interaction between the funnel wake and the trailing vortex.

Strong spanwise velocities reaching $0.4U_\infty$ were found within the funnel wake, and

the flow had sharp velocity gradients surrounding the found vortical structure. The $\psi = 20°$ case showed similar features, but a second, larger, vortical structure formed around $y/SH = 0.2$. The trailing vortex appeared to have a weaker interaction with the funnel wake in the $\psi = 20°$ case. Steeper velocity gradients were also observed and reached magnitudes upwards of $0.6U_\infty$. No horseshoe vortices were present in the funnel wake for the quartering wind cases.

(c) The TR-PIV velocity contour results for crosswise Plane 2 showed the asymmetric recirculation region and patches of reduced streamwise flow extending above the superstructure. Both quartering wind cases had lingering features from crosswise Plane 1. For the $\psi = 10°$ case, a weak part of the trailing vortex was observed interacting with the recirculation region, and in the $\psi = 20°$ case, both vortical structures were present at this location, suggesting that the funnel wake had more energy to prolong these features. Once again, large spanwise velocity magnitudes reaching $0.4U_\infty$ were measured. The $\psi = 20°$ case had visible interaction between the leeward side and flight deck flow fields. Additionally, a small vortical structure formed on the starboard side of the flight deck for the $\psi = 20°$ case.

(d) Stereoscopic TR-PIV results for crosswise Plane 3 showed asymmetry in the time-averaged flow field. A large region of reduced streamwise flow was observed for both quartering wind cases. This region extended beyond the superstructure, and for the $\psi = 20°$ case, it moved towards the leeward side. In the $\psi = 10°$ case, the spanwise flow field revealed a sizable rotating structure covering almost the entire flight deck width. Conversely, the $\psi = 20°$ case had a small starboard side flight deck vortex that had sharp spanwise velocity gradients surrounding it. This vortex appeared to be a consequence of the strong windward spanwise component and the leeward side upwash flow interactions. The $\psi = 20°$ case also had a region of spanwise velocity reaching values close to zero near the plane of symmetry above the flight deck.

(e) The PIV measurements for streamwise Plane 1 revealed a smaller recirculation region for the two quartering wind cases. Previously observed patches of reduced streamwise flow from the crosswise measurements were also evident in the streamwise measurements. This region extended beyond the height of the superstructure and covered about half of the flight deck length, starting after the recirculation region. Wall-normal velocities were positive in the funnel wake and covered a wider area. In the $\psi = 10^\circ$ case, a region with positive wall-normal velocity was found above the flight deck, which was likely related to the vortical structure found in crosswise Plane 3. Around the flight deck vortex location in the $\psi = 20^\circ$ case, the wall-normal velocity appeared to have a directional split, which agreed with the results from crosswise Plane 3.

2. The turbulent behavior of the airwake primarily revealed high fluctuations and turbulent kinetic energy (TKE) in the areas of observed flow characteristic from the qualitative velocity contour results. The turbulence intensities and TKE closely resembled the shapes of the overall flow field from the time-averaged velocity contours. However, high fluctuations and TKE values were found at the edges of the flight deck, suggesting flow separation from both the windward and leewards side flows. Additionally, the coherent motion was briefly examined, under the effects of the simulated atmospheric boundary layer (ABL), through a spectral analysis, two-point correlation, and proper orthogonal decomposition (POD).

   (a) Power spectral density (PSD) was calculated for two spatial locations within the funnel wake and above the flight deck. The PSD results revealed that the quartering wind cases had similar spectra for the u' fluctuations. However, at the funnel wake, the $\psi = 10^\circ$ case had a slight increase in magnitude in the Strouhal number range of 0.4 and 0.5. When compared to the headwind and $\psi = 20^\circ$ cases, the PSD also revealed the w' fluctuations to be significantly weaker for the

$\psi = 10^\circ$ case at the funnel wake location. This outcome result suggested that the $\psi = 10^\circ$ case was dominated by the streamwise flow within the funnel wake. The location above the flight deck showed a negligible difference for the headwind and quartering wind cases, suggesting the energy remained consistent at that spatial point. In addition, the PSD did not show an overall increase in energy at higher frequencies. Therefore, the airwake appeared to be primarily dominated by large-scale low-frequency content.

(b) Two-point correlation was performed for the same points used in the PSD analysis. The results showed strong coherent motion for the two-point correlation coefficient R_{uu}, but the correlated area decreased with an increase in yaw angle. The two-point correlations were used to better interpret the found flow field from the time-averaged velocity contours. Results showed a strong correlation in the region covering the first two crosswise planes, further supporting the finding of the funnel wake remaining influential in the quartering wind cases, especially for the $\psi = 20^\circ$ case.

(c) POD analysis showed the decomposition of the streamwise Plane 1 results. The results displayed the nontrivial nature of the flow field. A 90% flow field reconstruction required the first $1,000$ modes, highlighting the different energetic levels inherent within the airwake. Nevertheless, the first 10 modes contributed to around 20% of the total energy for the $\psi = 20^\circ$ case, around 23% for the headwind case, and 25% for the $\psi = 10^\circ$ case. The high energy of the first 10 modes for the $\psi = 10^\circ$ case agreed with the results from TKE and two-point correlation. The first four spatial basis modes were used to interpret flow features, and some success was obtained.

3. A qualitative comparison of the effects of ABL on the time-averaged flow field was performed. The results revealed that the airwake under the effects of the simulated

ABL was not dependent on Reynolds number. However, the ABL did reduce the overall velocity magnitude seen across the field of view (FOV), which was an expected outcome. Furthermore, some variations within the shape of the flow field were observed for crosswise Plane 2 in the $\psi = 20°$ case. However, these variations did not appear significant. Instead, the variation was related to the secondary vortical structure shift that was initially observed in crosswise Plane 1 and remained influential in crosswise Plane 2. Thus, the qualitative results suggested a negligible effect on the flow field shape. However, the simulated ABL did reduce the overall fluctuations and TKE levels. This reduction was related to the choice of normalization. Quantitative differences were not examined. However, the turbulent behavior analysis was performed for the results with the effects of the ABL.

4.2 Recommendations for Future Work

The research was primarily focused on establishing a qualitative basis for the Simple Frigate Shape No. 2 (SFS2) airwake with two different quartering wind conditions. A variety of unexplored topics related to quartering winds exist. While the current work covered parts of it, more detailed studies are possible to further contribute to the dynamic interface (DI) problem. Some potential areas that can be studied for a ship airwake with different quartering wind conditions include:

1. Different yaw angles will likely alter the flow field. A significant difference was observed between the $\psi = 10°$ and $\psi = 20°$ cases. It is clear that a change in yaw angle will have an effect on the overall shape of the flow field. While it is not feasible, at least in an experimental setting, to study incredibly small increments, changes in every 5° or 10° are possible in a larger test section, or with a smaller model. Prior work in literature tends to have larger increments of 15° or 30°, but the change in flow field shape appears to be drastic. Therefore, with smaller increments, a connection between the changes that occur can be made.

2. Particle image velocimetry (PIV) measurements only capture the flow field as a cross-sectional cut. Thus, additional planes of interest can be studied to form an even better understanding of the SFS2 airwake for different quartering wind conditions. Asymmetry is present in the spanwise variation of the airwake, which cannot be captured by a single streamwise plane. Regarding planes of interest, the appropriate reference frame must be decided, as that will influence the measurement objectives. The free-stream reference frame will capture the leeward side and the actual model airwake. In contrast, the body-axis reference frame will provide spatiotemporal information of the flow field.

3. A ship is subject to motion in six degrees of freedom. The present work considered a simple case of yaw only. In a practical setting, all six degrees of freedom would affect the airwake in some aspect. Thus, a combination of yaw and roll, or yaw and pitch, can be studied. Some research has been done for the effects of pitch, and roll, but there is a lack of combined configuration studies. Experimentally, such configurations are challenging to setup but are highly valuable for computational validations.

4. Proper orthogonal decomposition (POD) has shown to provide value in studies of highly turbulent flows. Different POD methods exist that can further expand on the coherent behavior seen within the ship airwake. The frequency content is relevant to the ship airwake problem, and spectral POD (SPOD) is capable of decomposing the flow into different frequency bands. Filtering specific frequencies could provide more information related to the flow behavior of the airwake. As seen in the current work, a clear deviation in magnitude was observed in the Strouhal number range of 0.4 and 0.5, and SPOD could decompose the flow field to closer inspect that specific frequency band. The time dynamics of the flow can also be filtered with the use of multi-scale POD. This would reveal if any periodic motions exist, and better enhance the large-scale low-frequency effects. These methods have been successfully implemented for the headwind case, and should be explored for different quartering wind cases as well.

5. The experimental framework feasibly covers only certain configurations. Thus, a computational approach can be used to study substantially more information about the entire three-dimensional flow field. In fact, there are more computational studies than experimental ones containing quartering wind cases. However, the computational simulations lack a consistent reason within their approach to the ship airwake study with quartering winds. Some studies include quartering wind cases for large angles but do not study the changes between the different cases. Other studies focus on the free-stream reference frame, which is not very useful if the objective is to understand the spatiotemporal changes on the flight deck for the DI problem. To this end, it would be beneficial to perform computational simulations that focus on the body axis reference frame and the intricacies within different quartering wind cases.

REFERENCES

[1] Forrest, J. S., Owen, I., Padfield, G. D., and Hodge, S. J., "Ship-Helicopter Operating Limits Prediction Using Piloted Flight Simulation and Time-Accurate Airwakes," *Journal of Aircraft*, Vol. 47, No. 3, 2012, pp. 1020–1031. https://doi.org/10.2514/1.C031525.

[2] Greenwell, D., and Barrett, R., "Inclined Screens for Control of Ship Air Wakes," *3rd AIAA Flow Control Conference*, San Francisco, CA, 2006, pp. 1314–1325. https://doi.org/10.2514/6.2006-3502.

[3] Quon, E. W., Cross, P. A., Smith, M. J., Rosenfeld, N. C., and Whitehouse, G. R., "Investigation of Ship Airwakes Using a Hybrid Computational Methodology," *Annual Forum Proceedings–AHS International*, Vol. 4, 2014, pp. 3001–3014.

[4] Zhang, J., Minelli, G., Basara, B., Bensow, R., and Krajnović, S., "Yaw Effect on Bi-Stable Air-Wakes of a Generic Ship Using Large Eddy Simulation," *Ocean Engineering*, Vol. 219, 2021. https://doi.org/10.1016/j.oceaneng.2020.108164.

[5] Tinney, C. E., and Ukeiley, L. S., "A Study of a 3-D Double Backward-Facing Step," *Experiments in Fluids*, Vol. 47, No. 3, 2009, pp. 427–438. https://doi.org/10.1007/s00348-009-0675-9.

[6] Mora, R. B., "Experimental Investigation of the Flow on a Simple Frigate Shape (SFS)," *The Scientific World*, Vol. 2014, 2014. https://doi.org/10.1155/2014/818132.

[7] Mora, R. B., Garcia, J. C. M., and García-Magariño, A., "Aerodynamic Optimization Over Frigate Helicopter Flight Deck by Hangar Shape Modifications," *AIAA Journal*, Vol. 59, No. 4, 2021, pp. 1387–1397. https://doi.org/10.2514/1.J059946.

[8] Zan, S. J., "On Aerodynamic Modelling and Simulation of the Dynamic Interface," *Proceedings of the Institution of Mechanical Engineers. Part G, Journal of Aerospace Engineering*, Vol. 219, No. 5, 2005, pp. 393–410. https://doi.org/10.1243/095441005X30315.

[9] Zhu, N., Zhang, Z., Gnanamanickam, E., and Leishman, J. G., "Dynamics of Large-Scale Flow Structures within Ship Airwakes," *AIAA Scitech 2022 Forum*, San Diego, CA, 2022, pp. 2532:1–2532:23. https://doi.org/10.2514/6.2022-2532.

[10] Seth, D., Leishman, J. G., Gnanamanickam, E., and Zhang, Z., "Time-Resolved Ship Airwake Measurements in a Simulated Atmospheric Boundary Layer," *Journal of Aircraft*, Vol. 58, No. 3, 2021, pp. 624–649. https://doi.org/10.2514/1.C035886.

[11] Seth, D., "Contributions to the Understanding of Ship Airwakes Using Advanced Flow Diagnostic Techniques," Ph.D. Dissertation, Embry-Riddle Aeronautical University, Daytona Beach, FL, 2020.

[12] Zhu, N., "Analysis of Ship Airwakes Using Modal Decomposition," Master's Thesis, Embry-Riddle Aeronautical University, Daytona Beach, FL, 2021.

[13] Polsky, S. A., "A Computational Study of Unsteady Ship Airwake," *40th AIAA Aerospace Sciences Meeting & Exhibit*, Reno, NV, 2002, pp. 1022:1–1022:10. https://doi.org/10.2514/6.2002-1022.

[14] Memon, W. A., Owen, I., and White, M. D., "Motion Fidelity Requirements for Helicopter-Ship Operations in Maritime Rotorcraft Flight Simulators," *Journal of Aircraft*, Vol. 56, No. 6, 2019, pp. 2189–2209. https://doi.org/10.2514/1.C035521.

[15] Advani, S. K., and Wilkinson, C. H., "Dynamic Interface Modelling and Simulation-A Unique Challenge," *Royal Aeronautical Society Conference on Helicopter Flight Simulation*, London, 2001.

[16] Kääriä, C. H., Wang, Y., Padfield, G. D., Forrest, J. S., and Owen, I., "Aerodynamic Loading Characteristics of a Model-Scale Helicopter in a Ship's Airwake," *Journal of Aircraft*, Vol. 49, No. 5, 2012, pp. 1271–1278. https://doi.org/10.2514/1.C031535.

[17] Shukla, S., Sinha, S. S., and Singh, S. N., "Ship-Helo Coupled Airwake Aerodynamics: A Comprehensive Review." *Progress in Aerospace Sciences*, Vol. 106, 2019, pp. 71–107. https://doi.org/10.1016/j.paerosci.2019.02.002.

[18] Corrsin, S., "Extended Applications of the Hot-Wire Anemometer," National Advisory Committee for Aeronautics, TN No. 1864, 1949.

[19] Raffel, M., Willert, C. E., Wereley, S. T., and Kompenhans, J., *Particle Image Velocimetry: A Practical Guide*, Second Edition, Springer, 2007.

[20] Shi, Y., Li, G., Su, D., and Xu, G., "Numerical Investigation on the Ship/Multi-Helicopter Dynamic Interface," *Aerospace Science and Technology*, Vol. 106, 2020, pp. 106175:1–106175:19. https://doi.org/10.1016/j.ast.2020.106175.

[21] Yuan, W., Wall, A., and Lee, R., "Combined Numerical and Experimental Simulations of Unsteady Ship Airwakes," *Computers & Fluids*, Vol. 172, 2018, pp. 29–53. https://doi.org/10.1016/j.compfluid.2018.06.006.

[22] Sydney, A. J., Ramsey, J., and Milluzzo, J., "Time-Resolved PIV Measurements of Ship Motion and Orientation Effects on Airwake Development," *35th AIAA Applied Aerodynamics Conference*, Denver, CO, 2017, pp. 4230:1–4230:11. https://doi.org/10.2514/6.2017-4230.

[23] Garnett, T. S., "Investigation to Study the Aerodynamic Ship Wake Turbulence Generated by a DD963 Destroyer," Report D210-11545-1, 1979.

[24] Healey, J. V., "A Data Base for Flight in the Wake of a Ship," *30th Aerospace Sciences Meeting and Exhibit*, Reno, NV, 1992, pp. 295:1–295:11. https://doi.org/10.2514/6.1992-295.

[25] Zan, S. J., and Garry, E. A., "Wind Tunnel Measurements of the Airwake Behind a Model of a Generic Frigate," NRC-IAR-LTR-AA-13, 1994.

[26] Maltby, R. L., and Keating, R. F. A., "Flow Visualization in Wind Tunnels Using Indicators," *NATO Advisory Group for Aeronautical Research and Development*, Vol. 70, 1962, pp. 29–38.

[27] LaVision, "Product Manual for DaVis 10.2," Göttingen, Germany, 2021.

[28] Wieneke, B., "PIV Uncertainty Quantification from Correlation Statistics," *Measurement Science & Technology*, Vol. 26, No. 7, 2015, pp. 074002:1–074002:10. https://doi.org/10.1088/0957-0233/26/7/074002.

[29] Chen, J., "Two-point Statistics of Coherent Structure in Turbulent Flow," *Journal of Flow Control, Measurement & Visualization*, Vol. 7(4), 2019, pp. 153–173. https://doi.org/10.4236/jfcmv.2019.74012.

[30] Solomon Jr, O. M., "PSD Computations Using Welch's Method," Technical Report SAND-91-1533, Sandia National Labs, 1991.

[31] Bendat, J. S., and Piersol, A. G., *Random Data: Analysis and Measurement Procedures*, 4$^{\text{th}}$ ed., John Wiley & Sons, Hoboken, NJ, 2011.

[32] Lumley, J. L., "The Structure of Inhomogeneous Turbulent Flows," *Atmospheric Turbulence and Radio Wave Propagation*, 1967, pp. 221–227.

[33] Weiss, J., "A Tutorial on the Proper Orthogonal Decomposition," *AIAA Aviation 2019 Forum*, 2019, pp. 3333:1–3333:21. https://doi.org/10.2514/6.2019-3333.

[34] Mendez, M. A., Balabane, M., and Buchlin, J., "Multi-scale Proper Orthogonal Decomposition of Complex Fluid Flows," *Journal of Fluid Mechanics*, Vol. 870, 2019, pp. 988–1036. https://doi.org/10.1017/jfm.2019.212.

I Appendix - Measurement Uncertainties

Stereoscopic time-resolved particle image velocimetry (TR-PIV) resolves three velocity components. The uncertainties related to the streamwise velocity component were addressed in Section 2.5.4. The remaining two components will be briefly covered as it is necessary to examine the validity of the measurements for PIV setups with substantial oblique camera viewing angles. Once again, the uncertainties were calculated by DaVis 10.2 [27, 28].

The spanwise and wall-normal velocity component uncertainties of crosswise Plane 1 for the $\psi = 10°$ case are shown in Fig. I.1 & I.2. As discussed in Section 2.5.4, the red dots represent the PIV measurements, and the black dots represent the uncertainty. It is evident that the uncertainties of the spanwise and wall-normal velocity components were very low. The uncertainties were less than 1%, as they were for the streamwise velocity component. It is important to reiterate that the velocity profiles shown in these figures were located at $y/SH \approx 0$, and that the uncertainties were slightly higher at areas including different flow behaviors, like the trailing vortex seen in crosswise Plane 1 (Fig. 3.13d). However, such an

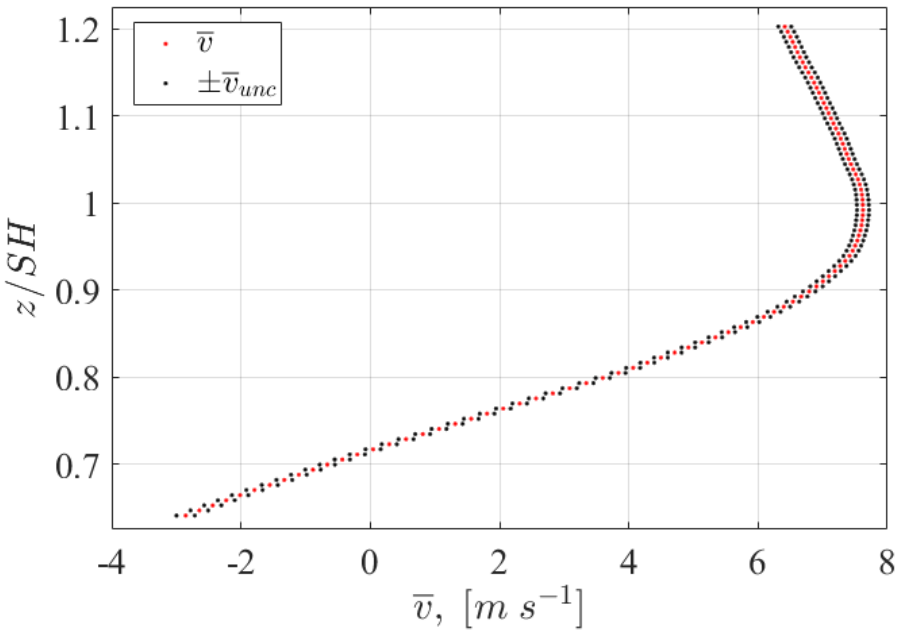

Figure I.1 The uncertainty of $\overline{v}$ for crosswise Plane 1 located at the magenta line in Fig. 2.11a.

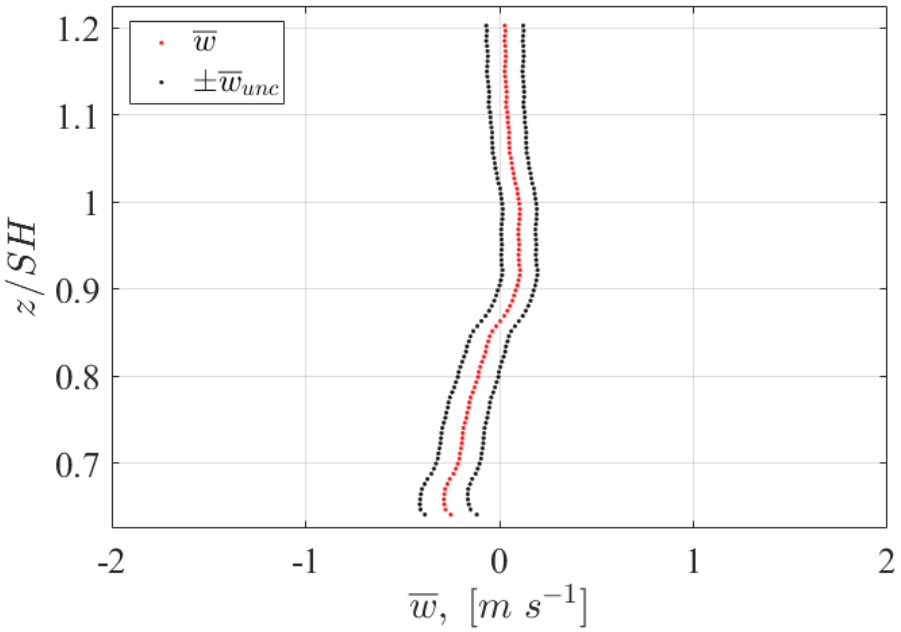

Figure I.2 The uncertainty of $\overline{w}$ for crosswise Plane 1 located at the magenta line shown in Fig. 2.11a.

outcome is expected in areas containing high turbulence or vortical flows. Although only the $\psi = 10°$ case was addressed, the uncertainties remained within the same margins for the $\psi = 20°$ case as well. Therefore, it is sufficient to consider the obtained PIV results as representative of the flow within the studied Simple Frigate Shape No. 2 airwake.

Similarly, the uncertainties for the planar PIV measurements of streamwise Plane 1 are shown in Fig. I.3–I.5. The uncertainty contour of Fig. I.3 highlights the different regions containing higher uncertainties. The most relevant region with a distinctly higher uncertainty was the recirculation region. As mentioned previously, it is expected for the uncertainties to be higher in regions containing high turbulence and unsteadiness. Thus, considering the overall region of streamwise Plane 1, the uncertainties appear to be close to zero, barring the recirculation region and the area near the funnel surface.

A closer inspection of the velocity component uncertainties alongside the magenta line of Fig. I.3 revealed a similar outcome previously found for crosswise Plane 1 uncertainties. The velocity profiles are shown in Fig. I.4 & I.5. Once again, the red dots represent the

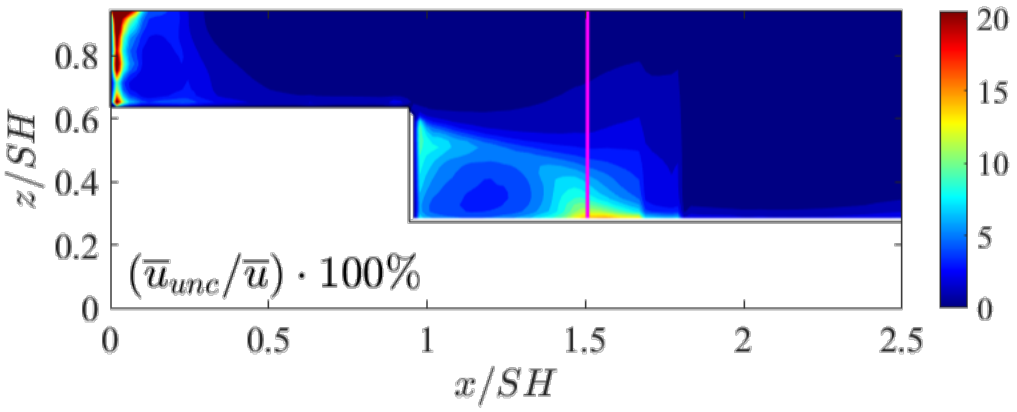

Figure I.3 Streamwise Plane 1 uncertainty contour of $\overline{u}_{unc}$ normalized to the $\overline{u}$ for $\psi = 10°$. The magenta line is the location of uncertainties for Fig. I.4–I.5.

measurements, and the black dots represent the respective uncertainty of each measurement. Higher uncertainties were observed closer to the flight deck surface, and as the velocity profile approached the free-stream, the uncertainties further decreased. A similar result was obtained

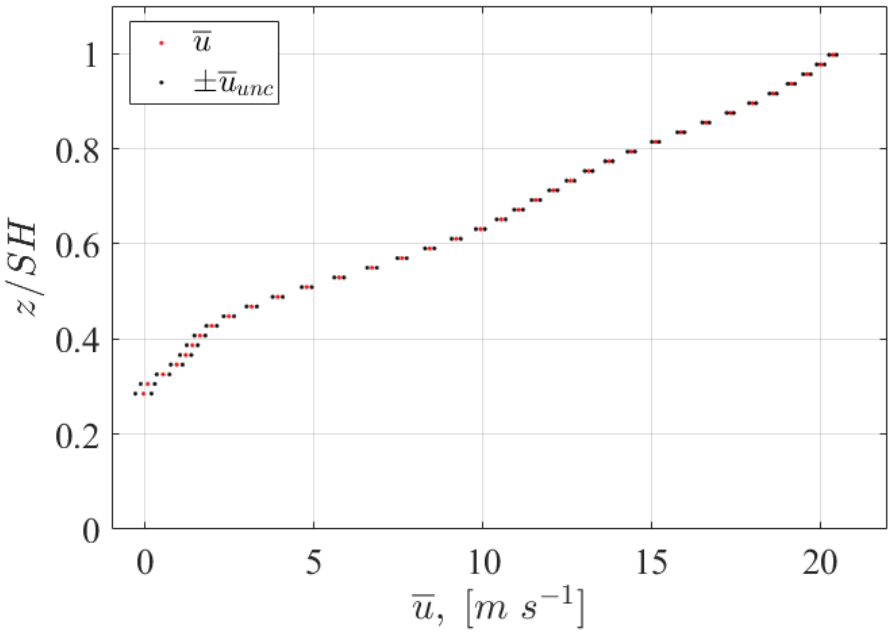

Figure I.4 The uncertainty of $\overline{u}$ for streamwise Plane 1 located at the magenta line shown in Fig. I.3.

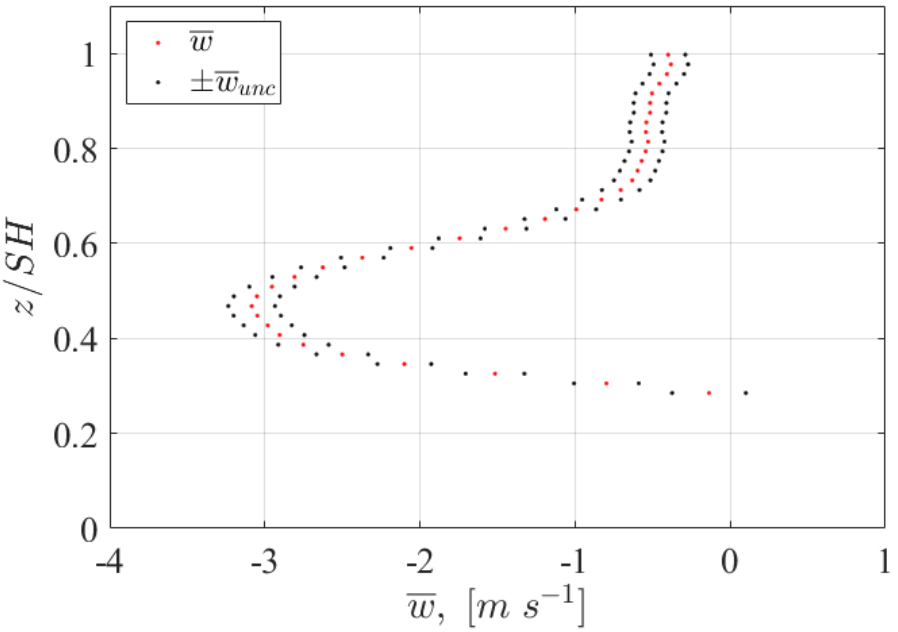

Figure I.5 The uncertainty of $\overline{w}$ for streamwise Plane 1 located at the magenta line shown in Fig. I.3.

for the $\psi = 20°$ case. For both cases, the uncertainties remained below 1% throughout the entire region of interest, except within the areas of higher unsteadiness of the flow. Therefore, the planar PIV results are representative of the airwake as well.